

PE&RS

October 2020

Volume 86, Number 10

PHOTOGRAMMETRY, ENGINEERING & REMOTE SENSING The official journal of the International Association of Photogrammetry and Remote Sensing





WHITTLES PUBLISHING

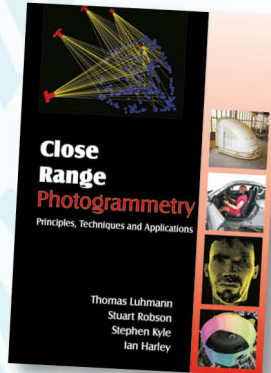
SIMPLY BRILLIANT BOOKS

ASPRS
MEMBER EXCLUSIVE

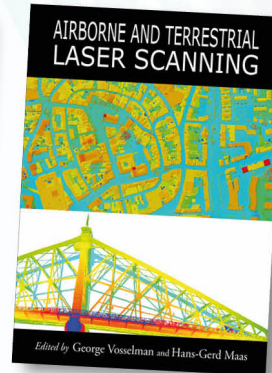
20%
DISCOUNT

ON ALL WHITTLES PUBLISHING BOOKS
USING CODE WPASPRS2

WHITTLES PUBLISHING'S STABLE OF CLASSIC GEOMATICS BOOKS INCLUDES THE THREE WINNERS OF THE PRESTIGIOUS KARL KRAUS MEDAL AWARDED BY ISPRS



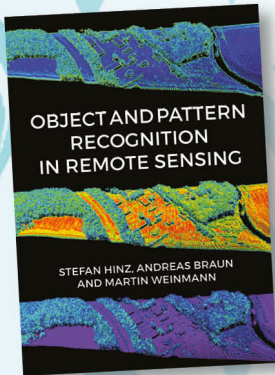
978-1870325-73-8
(Available as a CD)



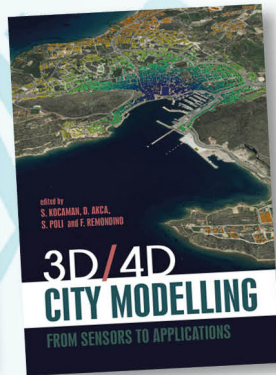
978-1904445-87-6



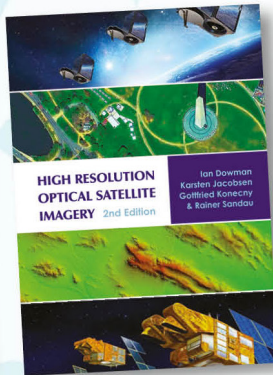
ISBN? Website only has 2nd edition



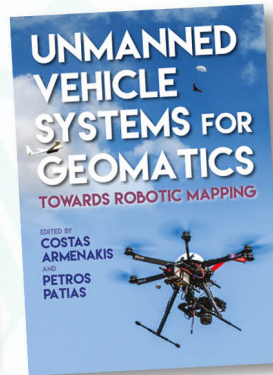
978-184995-128-9



978-184995-475-4



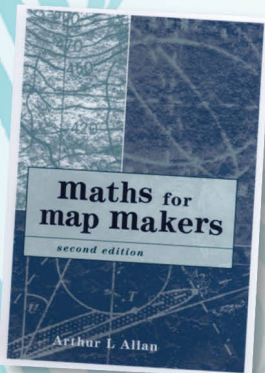
978-184995-390-0



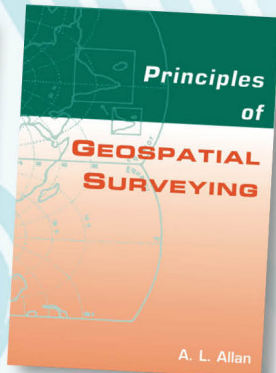
978-184995-127-2

OUR LIST CONTINUES TO EXPAND WITH THESE NEW TITLES

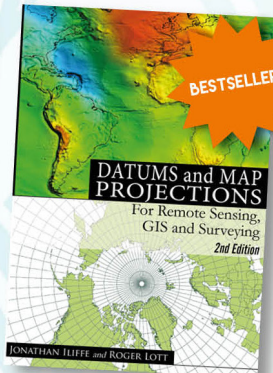
BROWSE OUR WEBSITE TO SEE OUR FULL RANGE OF ACCLAIMED GEOMATICS BOOKS



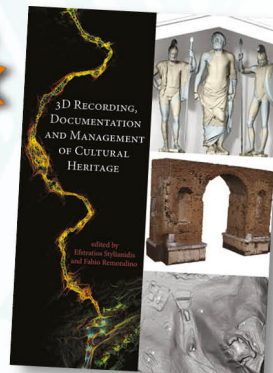
978-1870325-99-8



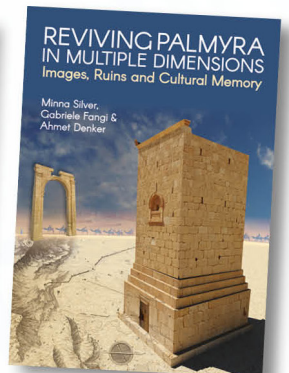
978-1904445-21-0



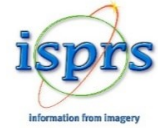
978-1904445-47-0



978-184995-168-5



978-184995-296-5



XXIV ISPRS Congress

International Society for Photogrammetry and Remote Sensing

4 – 10 July 2021, Nice, France



COMMISSION I
Sensor Systems



GERMANY / BRAZIL

COMMISSION II
Photogrammetry



ITALY / JAPAN

COMMISSION III
Remote Sensing



CHINA / CANADA

COMMISSION IV
Spatial Information Science



THE NETHERLANDS / CANADA

COMMISSION V
Education and Outreach



INDIA

www.isprs2020-nice.com

Keynote speakers



CHEN JUN
Chief Scientist NGCC



YVES UBELMANN
CEO - ICONEM



WILLEMIJN SIMON VAN LEEUWEN
Founder and CEO GeoFort



RAQUEL URTASUN
Head of Uber ATG



MICHAEL TONON
AIRBUS DEFENCE & SPACE



DAVIDE SCARAMUZZA
Professor University of Zurich & ETH Zurich



PIERRE ALLIEZ
Head of Science at Inria Sophia Antipolis

Executive committee



Nicolas Paparoditis
ENSG-IGN-Univ. Gustave Eiffel
Congress Director



Laurent Polidori
CESBIO
Congress Deputy Director



Tania Landes
INSA
Congress Media Chair



Clément Mallet
IGN
Congress Program Chair



Florent Lafarge
INRIA
Congress Program co-Chair



Pierre Grussenmeyer
INSA
Congress Industry Chair



Eric Labergerie
CNAM
Congress Financial Chair

Platinum sponsor



Gold sponsors



Silver sponsors



Bronze sponsors



Institutional partners, supporting graduate schools and associations



ANNOUNCEMENTS

URISA is pleased to announce the results of its 2020 URISA Board of Directors' election. Brent Jones will serve in the position of President-Elect and Kathryn Brewer, **Xan Fredericks**, and Steve Steinberg will serve as Directors. They will all begin their three-year terms at the conclusion of GIS-Pro 2020 which will be presented virtually this year.

Brent will serve as President-Elect for one year and his term as President will begin at the conclusion of GIS-Pro 2021.

Newly-elected URISA Board of Directors:

- Kathryn Brewer, GISP, Principal/GIS Project Manager, Spatial Relationships LLC, Boston Massachusetts
- Xan Fredericks, GISP, Lidar Coordinator/Associate National Map Liaison, US Geological Survey, St Petersburg, Florida
- Steven J. Steinberg, Ph.D., MPA, GISP, Geographic Information Officer (GIO), County of Los Angeles, Los Angeles, California

ACCOMPLISHMENTS

Atlantic is pleased to announce Nickolas Fusco, PLS, PSM as our most recent addition to the Executive Leadership team. Nick brings decades of proven surveying and engineering experience and will focus on bringing that expertise to all Atlantic clients.

"I am so excited for Nick to join the Atlantic Team," said Dennis Hall, Atlantic's Vice President of Business Development. "Nick's 45+ years of experience in the geospatial industry will be invaluable to our team. I believe his experience and licensure in the surveying field will open doors to us and will expand our service offering to our clients. We are looking forward to leveraging his extensive experience with the US Army Corps of Engineers and State Departments of Transportation to further build our clientele."

For more information, please visit www.atlantic.tech.

EQUIPMENT & TECHNOLOGY

SPECTRAL EVOLUTION provides portable spectroradiometers that can be used to take albedo measurements in the field. Spectroradiometers include the SR-6500, RS-8800, RS-5400, PSR+, RS-3500 and PSR-1100f. These spectroradiometers and FOV lenses are calibrated to NIST standards for absolute radiance measurements. Using a calibrated straight or right angle diffuser, a spectra of the downwelling irradiance can be accurately measured.

Albedo is a measurement of the electromagnetic solar radiation reflected by the earth's surface divided by the radiation incident on its surface. It is a fraction of the incident sunlight that a surface reflects. Albedo has a value from zero to one, with zero being a black totally absorbing surface and one being a mirror-like completely reflecting surface. Bright earth albedos like snow, clouds and ice have albedos ranging from 50% to 90%

while dark surfaces such as asphalt roads, dark soils and forests have albedos ranging from 5% to 20%.

For more information on measuring albedo, visit: <https://spectralevolution.com/applications/remote-sensing/measuring-albedo-with-a-field-spectroradiometer/>.

The SPECTRAL EVOLUTION RS-8800 field spectroradiometer now works with a wide range of our accessories for *in situ* measurements for remote sensing applications.

The RS-8800 is uniquely equipped with SPECTRAL EVOLUTION'S *Sensaprobe*TM grip which features a tilt angle sensor, auto-rangefinder and camera to automatically photograph and record field of view of scanned image displayed on your personal cell phone. This unique capability provides researchers with a convenient way to see exactly what they are measuring.

The RS-8800 field spectroradiometer is a full range (350-2500nm) high resolution/high sensitivity system including an Internet of Things (IoT) operating system that allows you to operate the system by iPhone, Android device, or tablet.

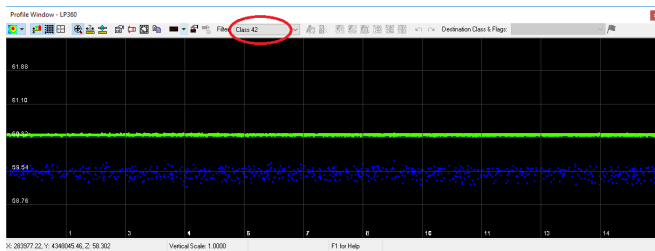
The RS-8800 uses its IoT operating system to control our accessories so that any user can get consistent scans. The IoT uses a WiFi network accessed by an Android device, iPhone or tablet for controlling the system and downloading data stored on the instrument.

For more information visit: <https://spectralevolution.com/products/hardware/field-portable-spectroradiometers-for-remote-sensing/rs-8800-remote-sensing-bundle/>

CALENDAR

- 30 November - 4 December 2020, **Climate Change and Disaster Management — Technology and Resilience in a Troubled World**, Sydney, Australia. For more information, visit <https://conference.unsw.edu.au/en/ccdm2020>.
- 28 January - 4 February 2021, **43rd COSPAR Scientific Assembly**, Sydney, Australia. For more information, visit <https://www.cospar2020.org/>.
- 7-11 June 2021, **URISA GIS Leadership Academy**, Minneapolis, Minnesota. For more information, visit www.urisa.org/education-events/urisa-gis-leadership-academy/.
- 16-20 August 2021, **URISA GIS Leadership Academy**, Portland, Oregon. For more information, visit <https://www.urisa.org/education-events/urisa-gis-leadership-academy/>.
- 8-12 November 2021, **URISA GIS Leadership Academy**, St. Petersburg, Florida. For more information, visit www.urisa.org/education-events/urisa-gis-leadership-academy/.
- 23-25 April 2021, **GISTAM 2021**, Prague, Czech Republic. For more information, visit www.gistam.org/.

FEATURE



595 GIS Tips & Tricks—Order Does Not Matter for LAStools

By Matthew Bauld and Al Karlin, Ph.D.
 CMS-L, GISP

 **2021 ASPRS Scholarship Application Season Now Open—**
 See page 606 for details



600 Deflections of the Vertical in Latvia

609 Uncertainty of Forested Wetland Maps Derived from Aerial Photography

Stephen P. Prisle, Jeffery A. Turner, Mark J. Brown, Erik Schilling, and Samuel G. Lambert

Forested wetlands (FWs) are economically and environmentally important, so monitoring of change is done using remote sensing by several U.S. federal programs. To better understand classification and delineation uncertainties in FW maps, we assessed agreement between National Wetlands Inventory maps based on aerial photography and field determinations at over 16 000 Forest Inventory and Analysis plots.

619 Weighted Spherical Sampling of Point Clouds for Forested Scenes

Alex Fafard, Ali Rouzbeh Kargar, and Jan van Aardt

Terrestrial laser scanning systems are characterized by a sampling pattern which varies in point density across the hemisphere. Additionally, close objects are over-sampled relative to objects that are farther away. These two effects compound to potentially bias the three-dimensional statistics of measured scenes. Previous methods of sampling have resulted in a loss of structural coherence. In this article, a method of sampling is proposed to optimally sample points while preserving the structure of a scene.

627 Redefining the Directional-Hemispherical Reflectance and Transmittance of Needle-Shaped Leaves to Address Issues in Their Existing Measurement Methods

Jun Wang, Jing M. Chen, Lian Feng, Jianhui Xu, and Feifei Zhang

The directional-hemispherical reflectance and transmittance of needle-shaped leaves are redefined in this study. We suggest that the reflected and transmitted radiation of a leaf should be distinguished by the illuminated and shaded leaf surfaces rather than the usual separation of the two hemispheres by a plane perpendicular to the incoming radiation.

643 Pavement Macrottexture Determination Using Multi-View Smartphone Images

Xiangxi Tian, Yong Xu, Fulu Wei, Oguz Gungor, Zhixin Li, Ce Wang, Shuo Li, and Jie Shan

Pavement macrottexture contributes greatly to road surface friction, which in turn plays a vital role in reducing road accidents. Conventional methods for macrottexture measurement are either expensive, time-consuming, or of poor repeatability. Based on multi-view smartphone images collected *in situ*, this paper develops and evaluates an affordable and convenient alternative approach for pavement macrottexture measurement. We demonstrate multi-view smartphone images can yield results comparable to the ones from the conventional laser texture scanner. It is expected that the developed approach can be adopted for large scale operational uses.

COLUMNS

593 Mapping Matters

597 Book Review—*Image Processing and Data Analysis with ERDAS IMAGINE*

599 Grids and Datums

This month we look at the Republic of Latvia

603 Signatures

The Column of the Student Advisory Council

ANNOUNCEMENTS

598 ASPRS Certifications

605 Headquarters News

605 New ASPRS Members

Join us in welcoming our newest members to ASPRS.

618 *PE&RS* Call for Submissions—Urban Remote Sensing

DEPARTMENTS

590 Industry News

590 Calendar

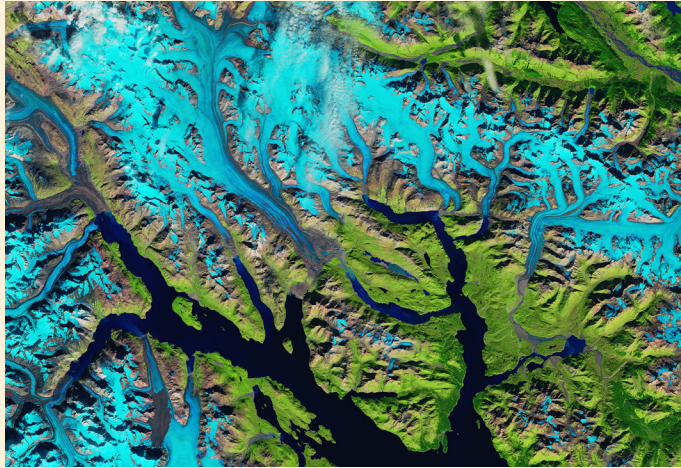
626 Who's Who in ASPRS

642 ASPRS Sustaining Members

652 ASPRS Media Kit

See the Cover Description on Page 592

COVER DESCRIPTION



In 1750, around the time the Little Ice Age reached its maximum, Glacier Bay in southeast Alaska was entirely filled with ice. When Captain George Vancouver sailed there in 1795, the glacial ice had pulled back to expose five miles of the bay—all part of a tidewater glacier's natural life cycle of advance and retreat. By the time naturalist John Muir explored and documented the region in 1879, the ice front had retreated 45 miles.

Today, the ice has retreated more than 60 miles (100 kilometers), and most vestiges of the original glacier now terminate on land. Just a handful of glaciers still flow into Glacier Bay and dispense icebergs—a type of glacier known as “tidewater glaciers.” Only one—McBride Glacier—still flows into the bay's East Arm.

The past few decades of glacial retreat are visible in the cover image, acquired on September 6, 1986, with Landsat 5, and the image above, acquired on September 17, 2019, with Landsat 8. Snow and ice are blue in these false-color images, which use different wavelengths to better differentiate areas of ice, rock, and vegetation.

Muir Inlet, Glacier Bay, and the surrounding land are part of Glacier Bay National Park. Around the time the park was established in 1980, most visitors viewed its glaciers from the vantage point of the water, where tidewater glaciers dropped huge slabs of ice into the bay. But the retreating glaciers, many of which now terminate on land, have changed how visitors experience the park.

“Recent retreat has been influenced by rapidly warming air and water temperatures,” said Andrew Bliss, a glaciologist with the National Park Service. “In the East Arm, all of the glaciers are retreating; in the West Arm, a few glaciers are stable or advancing slightly.”

One of the most notable retreats has occurred at Muir Glacier, which lost its tidewater terminus. That is, the glacier now ends on land instead of the water, where it once calved some of the park's most impressive icebergs.

“This retreat caused a major change in visitation patterns,” said Tania Lewis, a wildlife biologist and research coordinator at the park. Prior to the late 1980s, Muir Glacier was the main destination for visitors who wanted to view calving glaciers, icebergs, and the bay's wildlife.

Southeast of Muir Glacier, McBride is the last tidewater glacier in the bay's East Arm and the only remaining source of icebergs in this part of the bay. But that glacier is continuing to retreat. In 1998, Lewis spent six weeks near the terminus of McBride Glacier, where she studied harbor seals. “At that time, the inlet was only about a mile long and usually full of ice on which harbor seals hauled out, gave birth, and nursed their pups,” Lewis said.

The inlet leading to McBride Glacier now measures more than three miles long. “I went into McBride Inlet again last summer for the first time in over 10 years and was blown away by how far back it was, and how long the newly exposed inlet is,” Lewis said. During that visit she saw one large iceberg with some harbor seals on it. “Once McBride Glacier is grounded and is no longer tidewater, there will be no ice habitat left for seals in Muir Inlet.”

The changes to the park's tidewater glaciers are dramatic, providing visitors and scientists with a stark view of how ecosystems respond to ice retreat and a changing climate.

For more information or to see both images in their entirety, visit <https://landsat.visibleearth.nasa.gov/view.php?id=147171>.



THE IMAGING
& GEOSPATIAL
INFORMATION
SOCIETY

PHOTOGRAMMETRIC ENGINEERING & REMOTE SENSING

JOURNAL STAFF

Publisher ASPRS
Editor-In-Chief Alper Yilmaz
Assistant Editor Jie Shan
Assistant Director — Publications Rae Kelley
Electronic Publications Manager/Graphic Artist
Matthew Austin

Photogrammetric Engineering & Remote Sensing is the official journal of the American Society for Photogrammetry and Remote Sensing. It is devoted to the exchange of ideas and information about the applications of photogrammetry, remote sensing, and geographic information systems. The technical activities of the Society are conducted through the following Technical Divisions: Geographic Information Systems, Photogrammetric Applications, Lidar, Primary Data Acquisition, Professional Practice, and Remote Sensing Applications. Additional information on the functioning of the Technical Divisions and the Society can be found in the Yearbook issue of *PE&RS*.

Correspondence relating to all business and editorial matters pertaining to this and other Society publications should be directed to the American Society for Photogrammetry and Remote Sensing, 425 Barlow Place, Suite 210, Bethesda, Maryland 20814-2144, including inquiries, memberships, subscriptions, changes in address, manuscripts for publication, advertising, back issues, and publications. The telephone number of the Society Headquarters is 301-493-0290; the fax number is 225-408-4422; web address is www.asprs.org.

PE&RS. *PE&RS* (ISSN0099-1112) is published monthly by the American Society for Photogrammetry and Remote Sensing, 425 Barlow Place, Suite 210, Bethesda, Maryland 20814-2144. Periodicals postage paid at Bethesda, Maryland and at additional mailing offices.

SUBSCRIPTION. For the 2020 subscription year, ASPRS is offering two options to our *PE&RS* subscribers — an e-Subscription and the print edition. E-subscribers can plus-up their subscriptions with printed copies for a small additional charge. Print and Electronic subscriptions are on a calendar-year basis that runs from January through December. We recommend that customers who choose both e-Subscription and print (e-Subscription + Print) renew on a calendar-year basis.

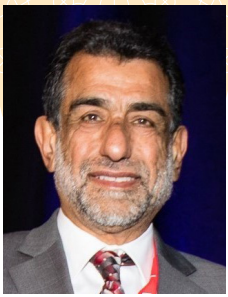
The rate of the e-Subscription (digital) Site License Only for USA and Non-USA is \$1000.00 USD. e-Subscription (digital) Site License Only for Canada* is \$1049.00 USD. e-Subscription (digital) Plus Print for USA is \$1365.00 USD. e-Subscription (digital) Plus Print for Canada* is \$1424.00 USD. e-Subscription (digital) Plus Print for Non-USA is \$1395.00 USD. Printed-Subscription Only for USA is \$1065.00 USD. Printed-Subscription Only for Canada* is \$1124.00 USD. Printed-Subscription Only for Non-USA is \$1195.00 USD. *Note: e-Subscription/Printed-Subscription Only/e-Subscription Plus Print for Canada include 5% of the total amount for Canada's Goods and Services Tax (GST #135123065). **PLEASE NOTE: All Subscription Agencies receive a 20.00 USD discount.**

POSTMASTER. Send address changes to *PE&RS*, ASPRS Headquarters, 425 Barlow Place, Suite 210, Bethesda, Maryland 20814-2144. CDN CPM #40020812

MEMBERSHIP. Membership is open to any person actively engaged in the practice of photogrammetry, photointerpretation, remote sensing and geographic information systems; or who by means of education or profession is interested in the application or development of these arts and sciences. Membership is for one year, with renewal based on the anniversary date of the month joined. Membership Dues include a 12-month electronic subscription to *PE&RS*. Or you can receive the print copy of *PE&RS* Journal which is available to all member types for an additional fee of \$60.00 USD for shipping USA, \$65.00 USD for Canada, or \$75.00 USD for international shipping. Dues for ASPRS Members outside of the U.S. will now be the same as for members residing in the U.S. Annual dues for Regular members (Active Member) is \$150.00 USD; for Student members \$50.00 USD for USA and Canada \$58.00 USD; \$60.00 USD for Other Foreign members. A tax of 5% for Canada's Goods and Service Tax (GST #135123065) is applied to all members residing in Canada.

COPYRIGHT 2020. Copyright by the American Society for Photogrammetry and Remote Sensing. Reproduction of this issue or any part thereof (except short quotations for use in preparing technical and scientific papers) may be made only after obtaining the specific approval of the Managing Editor. The Society is not responsible for any statements made or opinions expressed in technical papers, advertisements, or other portions of this publication. Printed in the United States of America.

PERMISSION TO PHOTOCOPY. The appearance of the code at the bottom of the first page of an article in this journal indicates the copyright owner's consent that copies of the article may be made for personal or internal use or for the personal or internal use of specific clients. This consent is given on the condition, however, that the copier pay the stated per copy fee of 3.00 USD through the Copyright Clearance Center, Inc., 222 Rosewood Drive, Danvers, Massachusetts 01923, for copying beyond that permitted by Sections 107 or 108 of the U.S. Copyright Law. This consent does not extend to other kinds of copying, such as copying for general distribution, for advertising or promotional purposes, for creating new collective works, or for resale.



MAPPING MATTERS

YOUR QUESTIONS ANSWERED

The layman's perspective on technical theory and practical applications of mapping and GIS

BY Qassim A. Abdullah, Ph.D., PLS, CP**

QUESTION:

Question: I came across one of your articles while searching for some answers about breaklines, so I figured I'd contact you for more information. The article I found is from September 2017 and it is about using breaklines for lidar datasets. I'm working with a surveyor and a drone pilot. The pilot flies, the surveyor does the ground control setup, I process the data and the surveyor confirms whether the product is accurate. Recently, the surveyor asked me if I can provide him directly with a TIN (triangulated irregular network). The problem that I am having is with breaklines. I can't find an industry standard or guidelines on when or where breaklines are needed. I'm starting to wonder, aside from using them for obvious things like gutters and roads and the sides of a cliff, if this is as much of an art as a science. Would you be able to point me in the right direction so I can learn more about what features need breaklines and when we should and should not use them?

Nathan Mangsen, Mangsen Mapping

Dr. Abdullah: First of all, it is always good to hear from a former student. As for your question, whether there is a need for breaklines is a controversial issue among users within the geospatial community. Breaklines were originally developed to ensure the accurate modeling of a terrain surface where sparsely compiled mass points (3D points collected by a stereo compiler using photogrammetric mapping principles) may result in the inaccurate representation of abrupt changes in terrain. Before lidar and digital photogrammetry, all topographic maps were created through a manual process using stereo photogrammetry. This process was time-consuming, expensive and did not always result in an

"The introduction of the breaklines concept was a genius approach at the time because we could not afford to model the terrain with a dense enough network of mass points."

accurate terrain model, since it depended on the thoroughness of the compilers and the quality of their stereo vision. The introduction of the breaklines concept was a genius approach at the time because we could not afford to model the terrain with a dense enough network of mass points, i.e.

collecting a mass point every one meter along the terrain, to accurately depict all details on the ground. Over the last two decades, lidar has alleviated the geospatial mapping community's main concern about the density of mass points and its ability to accurately model the terrain. These days, aerial lidar is collected at densities ranging from 2 points per square meter (USGS QL2) to hundreds of points per square meter, while a terrestrial or mobile lidar system can acquire data with a density of thousands of points per square meter. However, 30 years after the introduction of lidar, some factions of the industry are still hooked on the idea of collecting breaklines to augment dense lidar data. This outdated practice continued even when the data acquired using mobile lidar resulted in a point cloud with a density of thousands of points per square meter. Breaklines are used today in several other geospatial applications, including hydro enforcement, transportation engineering and to avoid some anomalies during the ortho-rectification

"The need for breaklines in those applications can be eliminated if software companies would devise solutions based on artificial intelligence (AI), machine learning and deep learning algorithms that utilize the computational power of the processing machine, AI-based algorithms and the richness of lidar data"

process. The need for breaklines in those applications can be eliminated if software companies would devise solutions based on artificial intelligence (AI), machine learning and deep learning algorithms that utilize the computational power of the processing machine, AI-based algorithms and the richness of lidar data (that lidar includes points cloud,

Photogrammetric Engineering & Remote Sensing
Vol. 86, No. 10, October 2020, pp. 593–594.
0099-1112/20/593–594

© 2020 American Society for Photogrammetry
and Remote Sensing
doi: 10.14358/PERS.86.10.593

“As an industry, we need to exert some pressure on the leading software manufacturers who are providing the industry with 3D modeling and road design packages”

lidar intensity images, and the natural color imagery from the RGB cameras). As an industry, we need to exert some pressure on the leading software manufacturers who are providing the industry with 3D modeling and road design packages. Their software is used by all state departments of transportation (DOTs) for road planning and design. Their software requires the user to provide breaklines to represent road centerlines, road edges, roadbeds, curbs and gutters, sidewalks, shoulders, tops of endwalls, tops of slopes, ditch bottoms, etc. For transportation projects, mobile lidar is usually used to create point clouds with a density estimated to be from 2,000 to 6,000 points per square meter. With this kind of dense points cloud, the software should be smart enough to find road crown, slopes, edges, etc. without relying on any manually compiled information. The question for the software developers is what could define the terrain details better than the information provided by 6,000 points (each with accurate X,Y,Z) per square meter and sub-centimeter resolution colored imagery? Currently, many users of these road design software packages acquire mobile lidar data with thousands of points per square meter, create breaklines from it, then decimate the point clouds to a 5-foot grid to be able to ingest it into the software. This practice is wasteful for two reasons: First, mobile lidar data acquired with a density of thousands of points per square meter is being decimated to 5-foot grid; and second, manually extracting breaklines, as mentioned above, is time-consuming and costly.

There is no justifiable reason for using breaklines, especially with dense lidar data. The lack of innovation by some

leading software companies is crippling the industry and limiting the utilization and benefits of lidar data. I hope algorithms and AI-based software will soon advance in a way to help us to unleash the power of lidar data and eliminate or minimize unnecessary laborious tasks such as these. The breakline concept was created decades ago to suit that era of mapping technologies. Breaklines should have no place in our mapping practices today since lidar can provide us with the most accurate and most thorough way to model the terrain.

“Breaklines should have no place in our mapping practices today since lidar can provide us with the most accurate and most thorough way to model the terrain.”

I hope this answers your question. For further reference, the Florida DOT manual for surveying and mapping provides excellent information about the requirements and guidelines for breaklines.

***Dr. Abdullah is Vice President and Chief Scientist at Woolpert, Inc. He is also adjunct professor at Penn State and the University of Maryland Baltimore County. Dr. Abdullah is ASPRS fellow and the recipient of the ASPRS Life Time Achievement Award and the Fairchild Photogrammetric Award.*

The contents of this column reflect the views of the author, who is responsible for the facts and accuracy of the data presented herein. The contents do not necessarily reflect the official views or policies of the American Society for Photogrammetry and Remote Sensing, Woolpert, Inc., NOAA Hydrographic Services Review Panel (HSRP), Penn State, and/or the University of Maryland Baltimore County.

Available on the ASPRS Website



The 4th Edition of the Manual of Remote Sensing!

The *Manual of Remote Sensing, 4th Ed.* (MRS-4) is an “enhanced” electronic publication available online from ASPRS. This edition expands its scope from previous editions, focusing on new and updated material since the turn of the 21st Century. Stanley Morain (Editor-in-Chief), and co-editors Michael Renslow and Amelia Budge have compiled material provided by numerous contributors who are experts in various aspects of remote sensing technologies, data preservation practices, data access mechanisms, data processing and modeling techniques, societal benefits, and legal aspects such as space policies and space law. These topics are organized into nine chapters. MRS4 is unique from previous editions in that it is a “living”

document that can be updated easily in years to come as new technologies and practices evolve. It also is designed to include animated illustrations and videos to further enhance the reader’s experience.

MRS-4 is available to ASPRS Members as a member benefit or can be purchased by non-members. To access MRS-4, visit <https://my.asprs.org/mrs4>.



Order Does Not Matter for LAStools

For most of us with any programming experience, especially us old FORTRAN programmers, we know that programming languages are carefully structured and the order of instructions in a program really matters. Getting things out of order may produce unexpected results. Rules, like using parenthesis around operators, as in converting angular coordinates into their decimal equivalents:

$$\text{Latitude} = ((\text{Degrees}) + (\text{Minutes}/60) + (\text{Seconds}/3600))$$

to ensure that operations are performed and grouped in the expected order are typically observed. Arguments for instructions are expected to follow a certain order otherwise the instruction may error (or go into that infinite loop). The same is generally true for Python scripting.

Here at Dewberry, we make use of a several commercial, off the shelf software tools when processing lidar data, but we usually customize them to our specific needs. The customization usually entails calling them from custom scripts, most of which are written in the Python programming language. Because LAStools (rapidlasso GmbH: <https://rapidlasso.com/lasools/>) contains numerous independent executable files, LAStools presents Dewberry the ideal opportunity to construct custom lidar processing Python scripts.

We have noticed that LAStools uses a syntax structure for Python scripting that is less demanding than most that we have previously encountered. Unlike Python interpreters, such as Arcpy (packaged with the Esri ArcGIS/ArcGISPro suite) which expects arguments to be given in a set order and separated by commas, LAStools accepts arguments in essentially any order and separated by spaces. While this feature of LAStools is well documented on the University of North

Carolina LAStools page (<https://www.cs.unc.edu/~isenburg/lasools/>) it is a bit difficult to find. So, below is an example of a LAStools command from a recent project that reclasses points with return number 0 from any ASPRS point class to ASPRS Class 42.

```
lastoolspath\las2las -i *.las -keep_return 0 -filtered_transform -set_extended_classification 42 -odix_reclass -olas -cores 8
```

Without previous knowledge, the code above doesn't make a ton of sense. This statement specifies the following:

Las2las -i *.las: call the las2las executable for each input files with the .las extension and do the following:

- keep_return 0: Filters point records with a return number of 0
- filtered_transform: Sets the filtered point records as the points to be manipulated
- set_extended_classification 42: Reclassifies the filtered points to ASPRS Class 42
- odix_reclass: Sets the output file name as the input name plus "_reclass"
- olas: Output file as LAS
- cores 8: use 8 computer cores for processing

The above code could also be input and successfully run as follows:

```
lastoolspath\las2las -i *.las -filtered_transform -olas -set_extended_classification 42 -cores 8 -keep_return 0 -odix_reclass
```

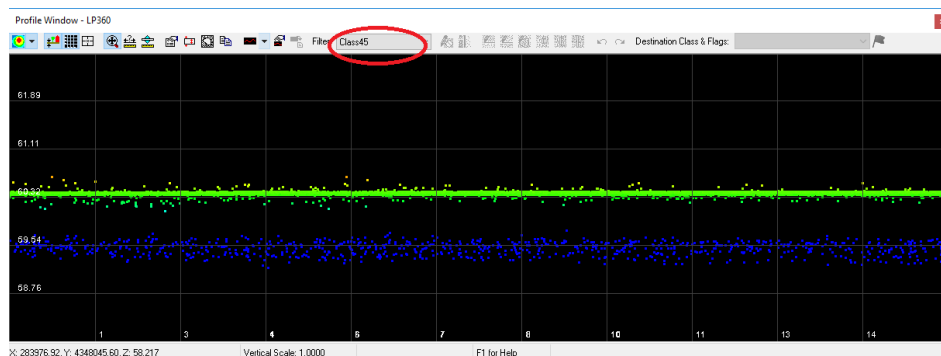


Figure 1. Synthetic (Return number zero) points have been erroneously assigned to ASPRS Class 45- (Green points) in this profile showing ONLY Class 45 points)

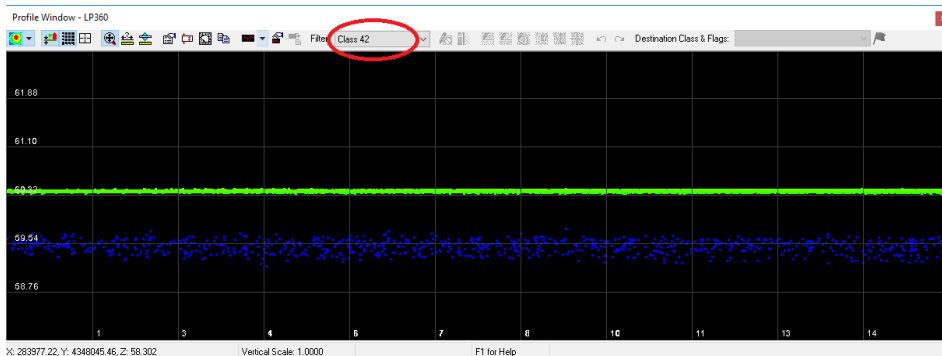


Figure 2. After running the aforementioned LASTools command, Return number zero points have been properly reclassified to ASPRS Class 42- Synthetic Water Surface (Green points) in this profile showing ONLY Class 42. The Terrascan suite does not currently support reclassification by return number, but this operation is supported in LASTools.

And there you have it, two LASTools Python scripts that produce the same results, but with the arguments in a different order.

Matt Bauld and Al Karlin, Ph.D., CMS-L, GISP are with Dewberry's Geospatial and Technology Services group in Tampa, FL. Matt is a Geospatial Analyst who works primarily with processing topobathymetric lidar and constructing lidar-derived DEMs and breaklines. As a Senior Geospatial Scientist, Al works with all aspects of Lidar, remote sensing, photogrammetry, and GIS-related projects.



The Rising Star program is focused on mentorship of tomorrow's leaders within ASPRS and the geospatial and remote sensing community. Geospatial companies, agencies, and ASPRS regions can all benefit by participation in the program through the advancement and professional development of their employees or associates through the process of sponsorship.

For more information go to www.asprs.org/rising-star-program.

[HTTP://DPAC.ASPRS.ORG](http://dpac.asprs.org)



"The ASPRS Aerial Data Catalog is a tool allowing owners of aerial photography to list details and contact information about individual collections. By providing this free and open metadata catalog with no commercial interests, the Data Preservation and Archiving Committee (DPAC) aims to provide a definitive metadata resource for all users in the geospatial community to locate previously unknown imagery."

ASPRS AERIAL DATA CATALOG

"THE SOURCE FOR FINDING AERIAL COLLECTIONS"

1

USE

Use the catalog to browse over 5,000 entries from all 50 states and many countries. Millions of frames from as early as 1924!

3

TELL

Spread the word about the catalog! New users and data collections are key to making this a useful tool for the community!

2

SUPPLY

Caretakers of collections with, or without metadata, should contact DPAC to add their datasets to the catalog for free!

For More Details Contact:

David Ruiz
druiz@quantumspatial.com
510-834-2001

David Day
dday@kasurveys.com
215-677-3119

Image Processing and Data Analysis with ERDAS IMAGINE is intended as a step-by-step guide on processing remotely sensed data using ERDAS IMAGINE in an educational setting. Split into fourteen chapters, the guide is organized in a workflow that a student might use during a geospatial research project. While the content is similar to existing software field guides and unpublished sources created by individual university professors or students, this book contains multiple exercises using GIS for easy reference.

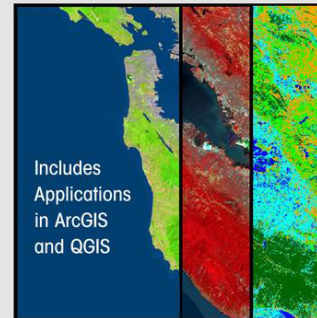
The content is grouped into five general areas, interweaved with instructions on using ERDAS IMAGINE, ESRI ArcMap for Desktop, and Quantum GIS (QGIS). The five areas are organized in various chapters; chapters 1 and 2 are on data collection focused on the acquisition of spatial data accompanied by instructions to ingest this data within the three software platforms; chapters 3 and 4 are on image processing that include georectification, orthorectification, and associated transformation and resampling techniques; chapters 6 and 7 are on image display limited to radiometric and spatial image enhancement; chapters 5 and 13 are focused on positional and thematic accuracy assessment separated by their usage within the instructional process; and chapters 8 to 12 and 14 are on image analysis. Review questions are included for each chapter with answers at the back of the book.

The book title places emphasis on ERDAS IMAGINE, but the book has almost equal content on ESRI ArcMap for Desktop and QGIS. These additions are a bonus for the user and should have been reflected in the title.

In Chapter 1, readers are to expect that a section on acquiring data from the LandsatLook Viewer will be included, but it is absent. In addition to acquiring data, this chapter includes instructions on displaying this data using the three geospatial software. The data acquisition information is already outdated, but readers should still be able to figure out where the information has moved or how to obtain similar data from the same websites.

Chapter 2 is the official introduction to the software applications, but software steps introduced in the previous chapter break up this workflow. In addition, the data acquisition steps are repeated, which makes some chapters stand on their own where others require other chapters to continue. The ERDAS steps used may not be the most efficient, but do not alter the outcome. For example, the book continually includes a step to 'Fit to Frame' for each image displayed. This step can be eliminated by presetting an option available in "Preferences." In addition, the remote sensing information relayed is limited or specific to the data the authors used in their exercises. Band Combinations is an example, where the reader would benefit from a table showing common band combinations and some uses of each combination for display and analysis.

Image Processing and Data Analysis with ERDAS IMAGINE®



Includes Applications in ArcGIS and QGIS

Stacy A.C. Nelson
Siamak Khorram



Image Processing and Data Analysis with ERDAS IMAGINE

Stacy A.C. Nelson and Siamak Khorram.

Taylor & Francis Group, LLC: Boca Rotan, FL. 2019. XV and 329 pp., diagrams, maps, photos, images, index. Hardcover. \$144.00. ISBN-13 978-1-1380-3498-3.

Reviewed by Shiloh Dorgan, Physical Scientist, U.S. Army Corps of Engineers, Alexandria, Virginia.

Chapters 3 and 4 on georectification and orthorectification could be merged into a single chapter, as the only difference between the ERDAS processes is the incorporation of elevation data. The absence of the information explaining different transformations and resampling techniques, as well as clear best practices in selecting ground control points, is a weak spot in the book. Aside from that, the simple steps in using ERDAS to perform rectifications are clear and useful.

Chapter 5 on Positional Accuracy Assessment is succinct and informative in including an easy to read explanation of Root Mean Square Error (RMSE). Chapters 6 and 7 introduce Radiometric and Spectral Image Enhancements that are concise and beneficial to users. It would further benefit students to know the different types of enhancements outside of the two

Photogrammetric Engineering & Remote Sensing
Vol. 86, No. 10, October 2020, pp. 597–598.
0099-1112/20/597–598

© 2020 American Society for Photogrammetry and Remote Sensing
doi: 10.14358/PERS.86.10.597

chapters, showing the distinction between Spectral, Radiometric, and Spatial Enhancements. Chapters 8-14 provide a great compilation of instructions for students to follow in order to digitize using manual photointerpretation in both two and three dimensions, supervised and unsupervised classification, and detailed thematic accuracy assessment, mostly using ERDAS.

The book does not thoroughly explain the underlying basics of evaluating and processing remotely sensed data, creating a potential weak spot that may impact a student's overall understanding of remote sensing and image processing if used as a stand-alone resource.

In summation, this book serves as an easy how-to guide for

new users of ERDAS, as well as for students new to geospatial technology. I appreciate the book's presentation of detailed step-by-step instructions for commonly used project applications. The book can serve as a reference for getting started, as well as a quick reminder for existing users. Readers will find the exercises useful in understanding how to use ERDAS IMAGINE, ESRI ArcMap for Desktop, QGIS, as well as to compare the similarities and differences between the three software. I am looking forward to future editions stemming from this effort.

STAND OUT FROM THE REST

EARN ASPRS CERTIFICATION

ASPRS congratulates these recently Certified and Re-certified individuals:

CERTIFIED UAS TECHNOLOGIST

Andrew Ortega, Certification #UAST035

Effective August 20, 2020, expires August 20, 2023

RECERTIFIED LIDAR TECHNOLOGIST

Cathy McPherson, Certification #R015PT

Effective July 20, 2020, expires July 20, 2023

RECERTIFIED PHOTOGRAMMETRIST

Jason Heywood, Certification #R1233CP

Effective March 18, 2020, expires March 18, 2025

ASPRS Certification validates your professional practice and experience. It differentiates you from others in the profession. For more information on the ASPRS Certification program: contact certification@asprs.org, visit <https://www.asprs.org/general/asprs-certification-program.html>.



ASPRS WORKSHOP SERIES

It's not too late to earn
Professional Development Hours



Miss one of our Geo Week 2020 Live Online Workshops? Not to worry! You can purchase the workshops now and watch when you are ready! Check out the workshops offered by visiting:

[https://conferences.asprs.org/
geowee-2020/workshops/](https://conferences.asprs.org/geowee-2020/workshops/)

Image Priscilla Du Preez on Unsplash.



& GRIDS & DATUMS

THE REPUBLIC OF LATVIA

BY Clifford J. Mugnier, CP, CMS, FASPRS

The Grids & Datums column has completed an exploration of every country on the Earth. For those who did not get to enjoy this world tour the first time, *PE&RS* is reprinting prior articles from the column. This month's article on the Republic of Latvia was originally printed in 2002 but contains updates to their coordinate system since then.

Between 2500 and 1500 BC, the Finno-Ugric and proto-Baltic tribes settled on Baltic shores. The closest ethnic relatives of the Latvians are the ancient Prussians, the Galinds, the Jatvings, and the Lithuanians. The first settlers in the territory of Latvia were the Livonians or "Libiesi." The Livonians were once concentrated in the northern part of Latvia, but today only about 100 individuals speak their ancient language which nevertheless has contributed to a prominent Latvian dialect. By the 12th century, the natives were split into a number of tribal groups, all practicing nature religions. The Knights of the Sword (Livonian Order) were crusaders that forcibly converted Latvia to Christianity in the 13th century. For centuries, Latvia has been under Swedish, Polish, German, and Russian rule. In 1918, Latvia proclaimed independence from Czarist Russia. By 1940, Latvia was occupied by the Soviet Union and was soon overrun by Nazi Germany. Soviet forces reoccupied the country in 1944-45, and Latvia remained under Soviet rule until 1991 when it was admitted into the United Nations. In May 1994, the Latvian National Independence Movement finished first in Latvia's first post-Soviet local elections; the excommunists fared the worst.

Latvia shares borders with Estonia to the north (343 km), Russia to the east (246 km), Belarus to the southeast (161 km), Lithuania to the south (588 km), and the Baltic Sea and Gulf of Riga to the west comprises a coastline of 498 km. Slightly larger than West Virginia, the country is mostly low coastal plain with the highest point being Gaizinkalns at 312 meters.

Survey activities in Latvia began with Tenner's first-order



network of 1820-32 in Semgallen and Courland, and were published by Czarist Russia in 1843 and 1847. Tenner later supplemented his primary net with lower-order stations. The Tenner chains were originally computed on the Walbeck 1819 ellipsoid where the semi-major axis (a) = 6,376,895 m and $1/f = 302.7821565$; they were later recomputed on the Bessel 1841 ellipsoid. Between 1878 and 1884, Schulgin further increased the density of lower-order stations in the area originally surveyed by Tenner. However, the majority of these latter station monuments did not survive into the 20th century, and they were ignored by the Russians. The Tenner net in the east did not extend further north than the Sestukalns-Gaizinkalns side, and the Struve primary net extended north from this side through Yuryev and over the Gulf of Finland. The Russian Western Frontier surveys were executed mainly by Yemel'yanov and Nikifrov between 1904 and 1912. These chains formed a major part of the modern (early) 20th century network of Eastern Latvia with some of the first-order stations being old Tenner or Struve stations. This Russian sur-

Photogrammetric Engineering & Remote Sensing
Vol. 86, No. 10, October 2020, pp. 599–602.
0099-1112/20/599–602

© 2020 American Society for Photogrammetry
and Remote Sensing
doi: 10.14358/PERS.86.10.599

Deflections of the Vertical in Latvia



Because of the groundbreaking work the University of Latvia's Institute of Geodesy and Geoinformatics published on their research to develop a one-centimeter geoid model and the invention of a relatively inexpensive Digital Zenith Camera (DZC) by Dr. Ansis Zarins, I traveled to Riga a couple summers ago. LSU's Center for GeoInformatics had acquired an absolute gravity meter along with a couple relative gravity meters and various related instruments and vehicles

with the same objective for the State of Louisiana. Since their DZC only works at night with clear skies for star shots, days were open for the staff to take me around Riga and environs. A major point of interest for me was the origin of the Yuryev II Datum and the General Latvian Triangulation Net Datum Origin is Riga St. Peter's Church (top of the Riga Church spire).

The Latvian Geodesists then took me inside of the church, and a plaque in the floor of the vestibule, directly under the plumb line of the spire displayed the actual Datum Origin:



By the way, their DZC worked flawlessly, and LSU purchased one for €100K, including training. Our DZC is currently kept busy here in Louisiana observing the deflection of the vertical at all of our GPS CORS sites.

vey covered much of western and central Livonia in 1904-05, and eastern Livonia and Lettgallen were covered with the 1906 and 1912 nets. Lower-order nets to fourth order supplemented the primary chains. These Czarist Russian surveys were computed on the Pulkovo 1904 Datum or the Yuryev II Datum, both of which are referenced to the Bessel 1841 ellipsoid where $a = 6,377,397.155$ m and $1/f = 299.1528128$.

After Latvia achieved Republic status, the new Latvian Survey Office began to unify these various nets in stages, before commencing with their own survey activities in 1924. The results of this program of unification are published in *Latvijas Valsts Trigonometriskais*. The Pulkovo 1904 Datum points were recomputed into Yuryev II Datum based on 14 available first-order Scharmhorst points, and this was then put into the Senks Soldner Grid. The 1905 Russian net had already been computed on the Yuryev II Datum, and was accepted into the Old Gaizinkalns Soldner Grid where $\varphi_0 = 56^\circ 52' 15.184''$ N and $\lambda_0 = 25^\circ 57' 34.720''$ East of Greenwich. No false origin was used. Similarly, the 1906 and 1912 nets were already on the Yuryev II Datum, and those form the Old Vitoleieki Soldner Grid where $\varphi_0 = 56^\circ 40' 08.64''$ N , $\lambda_0 = 27^\circ 15' 11.79''$ East of Greenwich, and no false origin was used. Tenner's survey had been calculated on the Walbeck 1819 ellipsoid and was now recomputed on the Bessel 1841 ellipsoid and controlled by the Yemel'yanov-Nikifirov survey of the Puci-Sarmes side. This had the effect of introducing a slight swing to the orientation of the Tenner triangulation. The Latvian Kulkigan and Puci systems cover this net. For most of eastern Latvia, the earlier Russian surveys could be used to form the basis of the Latvian triangulation as the station centers could be found. In Courland and Sengallen the original triangulation dated back to 1820 and few of the old stations could be recovered. This necessitated a complete new survey, which was started in 1924 from the Liepaja-Paplaka base and extended in stages to the Puci-Sarmes side and thence to Riga and Jelgava. The origin of this system is the Yuryev II Datum value of Riga St Peter's Church "tower ball" which is the same station as the Tenner first-order point. The Yuryev II Datum azi-

imuth to Jelgava Church was adopted for the orientation of the net. Although the Riga Church and Courland values are the same as Scharnhorst value and the azimuth is identical, the coordinates of Jelgava Church vary slightly by 0.002" in each axis. This was due to the scales of the Liepaja and Jelgava bases, which were adopted for the Courland System in preference to the less reliable Scharnhorst scale. This became known as the "Provisional Courland System (datum)." The Provisional Courland System was divided into two Cassini-Soldner Grids: The "Riga System" with its origin at Riga St. Peter's Church where $\varphi_0 = 56^\circ 56' 53.919''$ N and $\lambda_0 = 24^\circ 06' 31.898''$ East of Greenwich, and the "Vardupe System" with its origin at the Provisional Courland station Vardupe where $\varphi_0 = 56^\circ 51' 32.961''$ N and $\lambda_0 = 21^\circ 52' 03.462''$ East of Greenwich. No false origin was used for either grid. The Provisional Courland System was immediately adjusted and computed before the triangulation of central and east Latvia was completed. This Provisional Courland System was first adjusted within itself and then adjusted to the Latvian part of the Baltic Ring. The lower-order control as far east as $24^\circ 20'$ East of Greenwich was adjusted and computed in terms of this system.

The General Latvian Triangulation Net of first-order stations covers practically all of Latvia, including Courland. The lower-order control east of $24^\circ 20'$ East of Greenwich was computed in terms of the General Latvian Triangulation Net. Actually, there is a small overlap around $24^\circ 20'$ East of Greenwich for which the coordinates of all stations, of all orders, were computed in both the Provisional Courland System and the General Latvian Triangulation Net. The 1924 net was adjusted in stages to fit the following eight bases: Puci-Sarmen Jelgava, Jekabpils-Daborkalns, Garmaniski-Viski, Kangari-Jamilova, Kirbbisi-Akija, Duorno Sielo-Dziedzinka (Polish Base), Arula-Urkaste (Estonian Base), and Liepaja-Paplaka. The chain Puci-Sarmen to Jekabpils-Daborkalns forms the backbone of the modern net from which the adjustment started. The origin of the General Latvian Triangulation Net is Riga St. Peter's Church (top of the Riga Church spire) where $\Phi_0 = 56^\circ 56' 53.919''$ N, $\Lambda_0 = 24^\circ 06' 31.898''$ East of Greenwich, and the reference azimuth to Mitau German Church $\alpha_0 = 215^\circ 24' 04.38''$. The value for Riga St. Peter's Church approximates the Dorpat II System (datum). The Latvian control was computed in terms of four Cassini-Soldner Grids. The grid names and the coordinates of the respective origins are as follows: Vardupe Cassini-Soldner Grid where $\varphi_0 = 56^\circ 51' 32.961''$ N and $\lambda_0 = 21^\circ 52' 03.462''$ E; the Riga Cassini-Soldner Grid where $\varphi_0 = 56^\circ 56' 53.919''$ N and $\lambda_0 = 24^\circ 06' 31.898''$ E; the Gaizinkalns Cassini-Soldner Grid where $\varphi_0 = 56^\circ 52' 15.031''$ N and $\lambda_0 = 25^\circ 57' 34.920''$ E; and the Vitolnieki Cassini-Soldner Grid where $\varphi_0 = 56^\circ 40' 08.447''$ N and $\lambda_0 = 27^\circ 15' 12.252''$ E. These grid systems cover zones of about $1\frac{1}{2}^\circ$ to 2° wide, and overlap slightly. The Vardupe Grid is computed from the geographics of the Provisional Courland System, while the Gaizinkalns and Vitolnieki Grid values correspond to the General Latvian Triangulation Net. The Riga Cassini-Soldner Grid coordinates are computed from both the

Provisional Courland System geographics and the General Latvian Triangulation Net. However, care is taken in the Latvian "Trig" Lists to show from which geodetic system the Riga Cassini-Soldner coordinates are computed.

During these inter-war years, the Russians were also actively recomputing their survey information in the Baltic states. Prior to 1932 the Russian horizontal control of the Baltic States was always referenced to Dorpat Observatory at Tartu in Estonia. In 1932 the Russians set up Pulkovo Observatory 1932 as their horizontal datum and origin reference to the Bessel 1841 ellipsoid, and later revised this to Pulkovo 1942, now properly termed "System 42" (datum) referenced to the Krassovsky 1940 ellipsoid.

Thanks to E.A. Early of the U.S. Army Map Service, "In 1942 the German Army undertook the conversion of the Latvian Soldner coordinates to DHG Pulkovo." (Deutsches Heeres Gitter – German Army Grid) "The first phase of the conversion embodied the change of projection from Soldner to Gauss-Krüger. The Latvian Geodetic Engineer Mensin set up formulas and tables to convert the four Latvian Soldner systems to the German Gauss-Krüger system. However, upon checking these formulas at the boundaries of the Soldner systems, inadmissible gaps were discovered. Mensin's formulas were then abandoned and new ones were derived following the method given in Jordan-Eggert's *Handbuch der Vermessungskunde*. Since there were no reliable geodetic connections to the Pulkovo system available at that time, the conversion of the Latvian system to the Pulkovo 1932 system could only be approximated. The value of the datum point of the general Latvian triangulation net approximates the Dorpat II system value. The necessary formulas converting Dorpat II system values to the Pulkovo 1932 system were available in the official Russian work of Brigade Engineer O. A. Sergjiew, *Making and Editing of Military Maps*, Moscow 1939. In the absence of better data, these formulas were taken as a basis for the conversion to Pulkovo 1932 datum. The German Preliminary DHG Pulkovo 1932 coordinates resulting from this conversion were published in the form of *Ausgabe Koordinatenkartei* by the Kriegs-Karten und Vermessungsamt Riga, in 1943.

In 1943 extensive surveys were executed along the Latvian-Russian border for the final connection of the Latvian triangulation with the Pulkovo system. At the conclusion of these surveys, the Latvian system (already in terms of the preliminary DHG Pulkovo 1932 system) was converted to the Pulkovo 1932 system by a rigidfield adjustment. The Russian Pulkovo 1932 system coordinates used in this adjustment were taken from Russian Catalogs. As a consequence of this adjustment, new conversion constants were computed to convert from the four Latvian Soldner systems to the Final DHG Pulkovo 1932 system. As mentioned previously, the triangulation of Latvia is not completely uniform, since the triangulation in Courland is based on the Provisional Courland System adjustment. Only the first-order stations in Courland are available in terms of the General Latvian Triangulation Net. The lower-order trig in Courland was con-

verted from the Provisional Courland System to the General Latvian Triangulation Net by a graphical adjustment (triangle by triangle) based on the comparison of first-order values. After the lower-order trig in Courland was converted to terms of the General Latvian Triangulation Net, the Final DHG Pulkovo 1932 coordinate for all Latvia were computed. These coordinates were published in 1943 as a second edition *Ausgabe Endwerte Koordinatenkartei* by the Kriegs-Karten und Vermessungsamt, Riga. In the Fall of 1944 the publication of the *Koordinaten-Verzeichnis* (trig books) was begun. The coverage of these books is scanty. Also, it is noted that there are differences of up to a meter, at some stations, between the *Koordinaten-Verzeichnis* values and those from the second edition *Koordinatenkartei*. It appears that this difference is accounted for by the fact that some of the Latvian traverse points (as included in the second edition *Koordinatenkartei*) were resurveyed by the German Army and consequently were listed in the *Koordinaten-Verzeichnis* books by the German Survey values." To convert from DHG Pulkovo 1932 Datum Grid coordinates to European Datum 1950 coordinates on the UTM Grid, zone 34, use the following: (UTM Northing) = $0.9996056758 * (\text{DHG Northing}) + 0.0000176163 * (\text{DHG Easting}) + 828.01$, and (UTM Easting) = $0.9996056758 * (\text{DHG Easting}) + 0.0000176163 * (\text{DHG Northing}) + 365.98$. The NIMA published values for that general region of Europe from European Datum 1950 to WGS 84 are $\Delta X = -87\text{m} \pm 3\text{m}$, $\Delta Y = -95\text{m} \pm 3\text{m}$, and $\Delta Z = -120\text{m} \pm 3\text{m}$. The NIMA published values for System 42 Datum (in Latvia) to the WGS 84 Datum are $\Delta X = +24\text{m} \pm 2\text{m}$, $\Delta Y = -124\text{m} \pm 2\text{m}$, and $\Delta Z = -82\text{m} \pm 2\text{m}$.

UPDATE

"(The) origin of Latvian Coordinate System LKS-92 definition was based on two GNSS campaigns in 1992 and 2003. There are two continuously operating reference networks in Latvia: LatPos and EUPOS® -Riga. GNSS stations of these networks have fixed coordinate values in LKS-92. At the Institute of Geodesy and Geoinformatics of the University of Latvia both LatPos and EUPOS® -Riga station daily coordinate values are calculated. The coordinate differences between epochs 1989.0

and 2018.5 were obtained for LatPos and EUPOS® -Riga stations, expressed in ITRF14. ITRF reflects the motion of Eurasian plate in global frame of the Earth and ETRF89 system reflects the intraplate motion. Mean yearly coordinate components in ETRF89 were analysed. Comparison of LatPos and EUPOS® -Riga station coordinate components in ETRF89, LKS-92 and ETRF2000 coordinate systems was performed. Future of Latvian coordinate system LKS-92 is discussed." *Baltic J. Modern Computing, Vol. 7 (2019), No. 4, 513-524* <https://doi.org/10.22364/bjmc.2019.7.4.05>

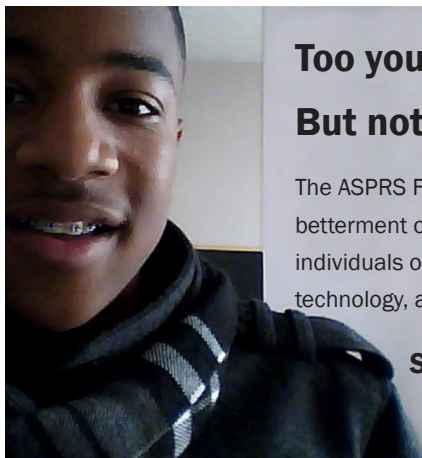
"According to the decision of IAG Reference Frame Subcommittee for Europe (EUREF) the EVRF2007 solution as the vertical reference has to be deployed in EU countries. The new height system *LAS-2000,5* had been enacted as the European Vertical Reference System's *EVRF2007* realization in Latvia and the new geoid model LV14 had been introduced by Latvian authority Latvian Geospatial Information Agency. However, the appreciation of the quality of quasi-geoid model LV14 is rather contradictory among the users in Latvia. The independent estimate and comparison of the two Latvian geoid models developed till now has been performed by the Institute of Geodesy and Geoinformatics. Previous geoid model LV98 which was developed for *Baltic-1977* height system almost 20 years ago is outdated now. Preparatory actions described in order to fulfil the task of comparison the geoids in two different height systems. The equations and transformation parameters are presented in this article for the normal height conversion from *Baltic-1977* height system to the Latvian realization named *LAS-2000,5*."

Balodis, J., Morozova, K., Silabriedis, G., Kalinka, M., 2016.

Changing the national height system and geoid model in Latvia. *Geodesy and Cartography* 42(1):20-24. DOI: 10.3846/20296991.2016.1168009.

The contents of this column reflect the views of the author, who is responsible for the facts and accuracy of the data presented herein. The contents do not necessarily reflect the official views or policies of the American Society for Photogrammetry and Remote Sensing and/or the Louisiana State University Center for GeoInformatics (C⁴G).

This column was previously published in *PE&RS*.



Too young to drive the car? Perhaps!

But not too young to be curious about geospatial sciences.

The ASPRS Foundation was established to advance the understanding and use of spatial data for the betterment of humankind. The Foundation provides grants, scholarships, loans and other forms of aid to individuals or organizations pursuing knowledge of imaging and geospatial information science and technology, and their applications across the scientific, governmental, and commercial sectors.

Support the Foundation, because when he is ready so will we.

asprsfoundation.org/donate



GREETINGS FROM THE ASPRS STUDENT ADVISORY COUNCIL (SAC)!

At SAC we are engaging the broader ASPRS Chapter community to become part of the SAC community network by inviting chapter presidents to our weekly SAC meeting. Our energized team members are building bridges, creating mutually beneficial relationships, and connecting chapters to increase inter-chapter engagement. This is SAC’s vision!

As part of this effort we are featuring the Oregon State University Chapter highlighting their remarkable contributions and introducing their elected officers.

Oregon State University ASPRS Student Chapter

The OSU ASPRS student chapter is a small but growing academic club welcoming all students and staff interested in geomatics, spatial science, photogrammetry, and remote sensing. Our mission is to provide support, knowledge, and outreach for OSU students and members of the public wanting to engage and excel in these scientific fields. We accomplish our mission through student connection, community education, conference participation, ASPRS regional engagement, and personal research and activities.

Educational Outreach Highlights

Mini-Lidar and 3D Scanning Demo

We partner with the OSU Office of Precollege Programs to offer public educational outreach. At local events like Discovery Days and Family Science and Engineering Night, young students (K-12) cycle through several short demonstrations and activities presented by various science and engineering departments from Oregon State University. During these outreach events, we connect with kids and parents by introducing them to the field of

| Faculty Involvement | | | | |
|---------------------|--|--|--------------------------------|---|
| | <p>Dr. Michael Wing – Faculty advisor for the OSU Student Chapter</p> <ul style="list-style-type: none"> Associate professor of geomatics in the OSU Forest Engineering, Resources, and Management Department Directs the Aerial Information Systems Lab at Oregon State University | <p>Dr. Christopher Parrish – Supporting Faculty and ASPRS Vice President</p> <ul style="list-style-type: none"> Associate Professor of Geomatics in the OSU School of Civil and Construction Engineering Directs the ASPRS Lidar Division and the Parrish Research Group at Oregon State University | | |
| | <p>Katie Nicolato</p> | <p>Sudeera Wickramaratna</p> | <p>Selina Lambert</p> | <p>Matt Barker</p> |
| Position | President | Secretary | Public Relations and Outreach | Webmaster |
| Degree | MS Student | PhD Student | MS Student | PhD Student |
| Major | Sustainable Forest Management in Forest Geomatics | Sustainable Forest Management in Forest Geomatics | Civil Engineering in Geomatics | Sustainable Forest Management in Forest Geomatics |

ASPRS STUDENT ADVISORY COUNCIL

YOUSSEF KADDOURA
COUNCIL CHAIR

EVAN VEGA
DEPUTY COUNCIL CHAIR

JASON MCGLAUGHLIN
EDUCATION COUNCILOR

GERARDO ROJAS
DEPUTY EDUCATION COUNCILOR

TERRA MCKEE
COMMUNICATIONS COUNCILOR

JEFF PU
DEPUTY COMMUNICATIONS COUNCILOR

MADISON FUNG
SOCIAL MEDIA COMMITTEE CHAIR

AUSTIN STONE
NETWORKING COUNCILOR

VICTORIA SCHOLL
DEPUTY NETWORKING COUNCILOR

LAUREN MCKINNEY-WISE
CHAPTERS COMMITTEE CHAIR

DAVID LUZADER
SAC ECPC LIASON



geomatics, how lidar works, and why geospatial mapping is important. Student chapter officer Selina Lambert fabricated a portable lidar and 3D scanning demonstration for these events. She built an Arduino-controlled mini-lidar sensor and distance readout mounted on a carriage capable of moving 2-dimensionally over model terrain made from spray insulation foam and drywall plaster.

da Vinci Days Arts and Science Festival

The da Vinci Days Arts and Science Festival is an annual summer festival held on the third weekend of July in Corvallis, Oregon. It is one of the most highly attended yearly events in Corvallis and the Willamette Valley. The festival showcases people and organizations communicating scientific missions and creative accomplishments. The most exciting and anticipated part of the festival is the Graand Kinetic Challenge, wherein teams build intricate and aesthetic human-powered machines to compete in a 20-mile race across city streets, sand dunes, a mud bog, and

the Willamette River. The OSU ASPRS student chapter provided a booth, UAS flight demos, and aerial videography of the Graand Kinetic Challenge at the 2019 festival. At the booth, festival visitors were encouraged to sight through a total station, explore unmanned aircraft systems, browse geomatics literature, and watch a student-produced UAS video.

Media Links

Email

photogrammetry@oregonstate.edu

Instagram

<https://www.instagram.com/asprs1868/>

OSU Club Website

<https://clubs.oregonstate.edu/asprs>

Twitter

<https://twitter.com/asprs1868>

ASPRS STUDENT ADVISORY COUNCIL

YOUSSEF KADDOURA
COUNCIL CHAIR

EVAN VEGA
DEPUTY COUNCIL CHAIR

JASON MCGLAUGHLIN
EDUCATION COUNCILOR

GERARDO ROJAS
DEPUTY EDUCATION COUNCILOR

TERRA MCKEE
COMMUNICATIONS COUNCILOR

JEFF PU
DEPUTY COMMUNICATIONS COUNCILOR

MADISON FUNG
SOCIAL MEDIA COMMITTEE CHAIR

AUSTIN STONE
NETWORKING COUNCILOR

VICTORIA SCHOLL
DEPUTY NETWORKING COUNCILOR

LAUREN MCKINNEY-WISE
CHAPTERS COMMITTEE CHAIR

DAVID LUZADER
SAC ECPC LIASON

JOURNAL STAFF

Editor-In-Chief

Alper Yilmaz, Ph.D., PERSEditor@asprs.org

Associate Editors

Rongjun Qin, Ph.D., qin.324@osu.edu

Michael Yang, Ph.D., michael.yang@utwente.nl

Petra Helmholz, Ph.D., Petra.Helmholz@curtin.edu.au

Bo Wu, Ph.D., bo.wu@polyu.edu.hk

Clement Mallet, Ph.D., clemallet@gmail.com

Jose M. Pena, Ph.D., jmpena@ica.csic.es

Prasad Thenkabail, Ph.D., pthenkabail@usgs.gov

Ruisheng Wang, Ph.D., ruiswang@ucalgary.ca

Desheng Liu, Ph.D., liu.738@osu.edu

Valérie Gouet-Brunet, Ph.D., valerie.gouet@ign.fr

Dorota Iwaszczuk, Ph.D., dorota.iwaszczuk@tum.de

Qunming Wang, Ph.D., wqm11111@126.com

Filiz Sunar, Ph.D., fsunar@itu.edu.tr

Norbert Pfeifer, np@ipf.tuwien.ac.at

Jan Dirk Wegner, jan.wegner@geod.baug.ethz.ch

Hongyan Zhang, zhanghongyan@whu.edu.cn

Dongdong Wang, Ph.D., dddwang@umd.edu

Zhenfeng Shao, Ph.D., shaozhenfeng@whu.edu.cn

Assistant Editor

Jie Shan, Ph.D., jshan@ecn.purdue.edu

Contributing Editors

Feature Articles

featureeditor@asprs.org

Grids & Datums Column

Clifford J. Mugnier, C.P., C.M.S., cjmce@lsu.edu

Book Reviews

Sagar Deshpande, Ph.D., bookreview@asprs.org

Mapping Matters Column

Qassim Abdullah, Ph.D., Mapping_Matters@asprs.org

Sector Insight

Lucia Lovison-Golob, Ph.D., lucia.lovison@sat-drones.com

Bob Ryerson, Ph.D., FASPRS, bryerson@kimgeomatics.com

GIS Tips & Tricks

Alvan Karlin, Ph.D., CMS-L, GISP akarlin@Dewberry.com

ASPRS Staff

Assistant Director — Publications

Rae Kelley, rkelley@asprs.org

Electronic Publications Manager/Graphic Artist

Matthew Austin, maustin@asprs.org

Advertising Sales Representative

Bill Spilman, bill@innovativemediasolutions.com

PE&RS SEEKS HIGHLIGHT ARTICLES

Are you looking for publishing opportunities? Consider publishing a Highlight Article in PE&RS.

PE&RS Highlight Articles are semi-technical or non-technical articles that appeal to a broad range of industry professionals. A variety of topics in geospatial science and technology, photogrammetry, and remote sensing can be addressed.

- geomatics education and programs
- new technologies
- non-traditional applications
- historical events and development
- collaborative initiatives
- new or unusual approaches to common problems
- recent or historical developments in technology or the industry

PE&RS Highlight Articles are always open access, published in color, and assigned a DOI number. For more information on this publishing opportunity or to discuss other opportunities, contact Rae Kelley, rkelley@asprs.org.

NEW ASPRS MEMBERS

ASPRS would like to welcome the following new members!

At Large

Hurmain Ariffin

Salem Mohammed Ghaleb Essa

Cascadia

Keenan Ganz

Eastern Great Lakes

David Stone Linden

Florida

Thomas Murphy

Adam D. Riddle

Heartland

Wei Chen

Intermountain

Ryan Shields

Mid South

Emil A. Cherrington, Ph.D.

Bryan S. Haley

Matthew James McCarthy, Ph.D.

Steven B. McKinney, Ph.D.

Ashish Pandey

Liangwei Qu, Ph.D.

Northeastern

Rabia Munsaf Khan

Ruth Lasher

Pacific Southwest

Liliana Aliyazicioglu

Philip Griffin

Ben Hardin

Omar Ernesto Mora, Ph.D.

Nathaniel David Newman

Joel Sherman

Cynthia Wirick

Potomac

Joshua Anstead

Robert Stanley Beach

Freda Elikem Dorbu

Keith Owens

FOR MORE INFORMATION ON ASPRS MEMBERSHIP, VISIT
[HTTP://WWW.ASPRS.ORG/JOIN-NOW](http://www.asprs.org/join-now)

Your Path To Success In The Geospatial Community

ASPRS ANNOUNCES THE OPENING OF THE 2021 SCHOLARSHIP APPLICATION SEASON!

ASPRS is pleased to offer nine scholarship awards totaling more than \$30,000 in value! Available to both undergraduate and graduate student members of ASPRS, these resources have been generated with the intention of advancing academic and professional goals in the geospatial sciences. ASPRS recognizes that students are the future of these rapidly evolving fields and encourages all who are qualified to take advantage of these unique opportunities.

IMPORTANT DATES

- Scholarship Application Window: September 30 – November 15
- Letters of recommendation deadline: November 22
- Anticipated Award Announcements Mid-Late January
- Award winners will be honored at the ASPRS 2021 Annual Meeting

All complete applications must be received at ASPRS no later than midnight, Eastern time on November 15, 2020. The deadline for recommendation letters is November 22, 2020.

Visit www.asprs.org/education/asprs-awards-and-scholarships for more information!

Summary of ASPRS Awards & Scholarships

| Award/ Short name | Eligibility | Type of Grant | Grant Amount | Expectations |
|----------------------|--|----------------|--------------|---|
| Altenhofen | Undergraduate or Graduate Students | One Year Award | \$2,000 | Report of scholastic accomplishments to ASPRS |
| Anson* | Undergraduate Students; USA Only | One Year Award | \$2,000 | Final Report to ASPRS |
| Behrens* | Undergraduate Students; USA Only | One Year Award | \$2,000 | Final Report to ASPRS |
| Colwell* | Doctoral Students USA or Canada | One Year Award | \$7,000 | Final Report to ASPRS |
| Fischer | Current or Prospective Graduate Students | One Year Award | \$2,000 | Final Report to ASPRS |
| Moffitt* | Graduate or Undergraduate Students | One Year Award | \$7,000 | Final Report to ASPRS |
| Osborn* | Undergraduate Students; USA Only | One Year Award | \$2,000 | Final Report to ASPRS |
| Ta Liang | Graduate Students | Travel Grant | \$2,000 | Report of accomplishments to ASPRS and to Ta Liang's family |
| Wolf | Prospective Teachers/Graduate Students; USA only | One Year Award | \$4,000 | Final Report to ASPRS |

*Recipient also receives a complementary membership renewal in ASPRS.

Francis H. Moffitt Scholarship

The purpose of the award is to encourage upper-division undergraduate and graduate-level college students to pursue a course of study in surveying and photogrammetry leading to a career in the geospatial mapping profession.

Eligibility

Students currently enrolled or intending to enroll in a college or university in the United States or Canada, who are pursuing a program of study in surveying or photogrammetry leading to a career in the geospatial mapping profession.

Award

- The award consists of a certificate and a check in the amount of \$7,000 and a one-year student membership (renewal) in ASPRS.
- This award is presented by ASPRS through the ASPRS Foundation from funds donated by students, associates, colleagues, and friends of Frank Moffitt as a memorial to his lifetime contributions to the photogrammetric surveying profession.

William A. Fischer Scholarship

To facilitate graduate-level studies and career goals directed towards new and innovative uses of remote sensing data/techniques that relate to the natural, cultural, or agricultural resources of the Earth.

Eligibility

Current or prospective graduate student members of ASPRS.

Award

- One year scholarship of \$2,000 and a certificate.
- This award is presented by ASPRS with funding provided by a grant from the ASPRS Foundation, on behalf of individual and corporate contributions to the Foundation in memory of William A. Fischer, a pioneer in the use of remote sensing from space for the study of the planet Earth.

Robert N. Colwell Fellowship

The purpose of the Award is to encourage and commend college/university graduate students at the PhD level who display exceptional interest, desire, ability, and aptitude in the field of remote sensing or other related geospatial information technologies, and who have a special interest in developing practical uses of these technologies.

Eligibility

The Award is made to a graduate student (PhD level) currently enrolled or intending to enroll in a college or university in the United States or Canada who is pursuing a program of study aimed at starting a professional career where expertise is required in remote sensing or other related geospatial information technologies.

Award

- The award consists of a certificate and a check in the amount of \$7,000 and a one-year student membership (renewal) in ASPRS.
- The award is presented by the ASPRS Foundation from funds donated by students, associates, colleagues, and friends of Robert Colwell, one of the world's most respected leaders in remote sensing, a field that he stewarded from the interpretation of World War II aerial photographs to the advanced acquisition and analysis of many types of geospatial data from military and civilian satellite programs.

John O. Behrens Institute for Land Information (ILI) Memorial Scholarship

The purpose of the Award is to encourage students/persons who have an exceptional interest in pursuing scientific research or education in geospatial science or technology or land information systems/records to enter a professional field where they can use the knowledge of this discipline to excel in their profession.

Eligibility

The Scholarship is made to an under-graduate student currently enrolled or intending to enroll in a university in the United States for the purpose of pursuing a program of study that prepares them to enter a profession in which education in geospatial science or land information disciplines will advance the value of those disciplines within that profession.

Award

- The award consists of a certificate and a check in the amount of \$2,000 and a one year student membership (renewal) in the Society.
- Funds from the ILI have been donated to the ASPRS Foundation to support the John O. Behrens ILI memorial Scholarship in recognition of Mr. Behrens' outstanding contributions over the many years of his distinguished career

Ta Liang Award

The purpose of the award is to facilitate research-related travel by outstanding graduate students in remote sensing. Such travel includes field investigations, agency visits, participation in conferences, or any travel that enhances or facilitates a graduate research program.

Eligibility

Graduate Student members of ASPRS.

Award

- A grant of \$2,000 and a hand-engrossed certificate.
- This award is presented by ASPRS, with funding provided by a grant from the ASPRS Foundation on

behalf of individual and corporate contributions to the Foundation in memory of Ta Liang, a skilled civil engineer, an excellent teacher, and one of the world's foremost air-photo interpreters.

Abraham Anson Scholarship

The purpose of the Award is to encourage students/persons who have an exceptional interest in pursuing scientific research or education in geospatial science or technology related to photogrammetry, remote sensing, surveying and mapping to enter a professional field where they can use the knowledge of this discipline to excel in their profession.

Eligibility

The Award is made to an under-graduate student currently enrolled or intending to enroll in a college or university in the United States for the purpose of pursuing a program of study to enter a profession in which education in photogrammetry, remote sensing, surveying and mapping and geospatial science or technology disciplines will advance the value of those disciplines within that profession.

Award

- The award consists of a certificate, a check in the amount of \$2,000 and a one-year student membership (renewal) in the society.
- This award is presented by the ASPRS Foundation from funds donated by the Anson bequest and contributions from the Society and the Potomac Region as a tribute to Abe Anson's many contributions to the field of photogrammetry, remote sensing, and long, dedicated service to the Society.

Robert E. Altenhofen Scholarship

The purpose of the Award is to encourage and commend college students who display exceptional interest and ability in the theoretical aspects of photogrammetry

Eligibility

The Award is made to an undergraduate or graduate student currently enrolled in a college or university in the United States or elsewhere, who is either a student or active member of ASPRS.

Award

- Cash prize of \$2,000 and a certificate.
- The award is administered by the ASPRS Foundation from funds provided by the estate of Mrs. Helen Altenhofen as a memorial to her husband, Robert E. Altenhofen. A past president of ASPRS, Mr. Robert Altenhofen was an outstanding practitioner of photogrammetry and made notable contributions to the mathematical aspects of the science.

Paul R. Wolf Scholarship

The purpose of the Award is to encourage and commend college students who display exceptional interest, desire, ability, and aptitude to enter the profession of teaching Surveying, Mapping, or Photogrammetry.

Eligibility

The Award is made to a graduate student member of ASPRS currently enrolled or intending to enroll in a college or university in the United States, who is pursuing a program of study in preparation for entering the teaching profession in the general area of Surveying, Mapping, or Photogrammetry.

Award

- The award consists of a certificate and a check in the amount of \$4,000.
- This Award is administered by the ASPRS Foundation from funds donated by the friends and colleagues of Paul R. Wolf as a memorial to him. Recognized nationally and internationally, Paul was an outstanding educator and practitioner of Surveying, Mapping, and Photogrammetry and a great friend of the Society. As author, teacher, and mentor, Paul made significant educational and academic contributions to these fields.

Kenneth J. Osborn Scholarship

The purpose of the Scholarship is to encourage and commend college students who display exceptional interest, desire, ability, and aptitude to enter the profession of surveying, mapping, photogrammetry, or geospatial information and technology. In addition, the Scholarship recognizes students who excel at an aspect of the profession that Ken Osborn demonstrated so very well, that of communications and collaboration.

Eligibility

The Scholarship is made to an undergraduate student currently enrolled or intending to enroll in a college or university in the United States, who is pursuing a program of study in preparation for entering the profession in the general area of surveying, mapping, photogrammetry, or geospatial information and technology.

Award

- This annual Scholarship consists of a certificate and a check in the amount of \$2,000 and a one year student membership (renewal) in the Society.
- This award is presented by the ASPRS Foundation, with funding provided by donations from friends and colleagues of Kenneth Osborn as a tribute to him.

Uncertainty of Forested Wetland Maps Derived from Aerial Photography

Stephen P. Prisley, Jeffery A. Turner, Mark J. Brown, Erik Schilling, and Samuel G. Lambert

Abstract

Forested wetlands (FWs) are economically and environmentally important, so monitoring of change is done using remote sensing by several U.S. federal programs. To better understand classification and delineation uncertainties in FW maps, we assessed agreement between National Wetlands Inventory maps based on aerial photography and field determinations at over 16 000 Forest Inventory and Analysis plots. Analyses included evaluation of temporal differences and spatial uncertainty in plot locations and wetland boundaries. User's accuracy for the wetlands map was 90% for FW and 68% for nonforested wetlands. High levels of false negatives were observed, with less than 40% of field-identified wetland plots mapped as such. Epsilon band analysis indicated that if delineation of FW boundaries in the southeastern U.S. met the data quality standards (5 meters), then the area within uncertainty bounds accounts for 15% to 30% of estimated FW area.

Introduction

Forested wetlands (FWs) are ecologically and economically important. They support exceptional biodiversity, flood storage, high water quality, and can produce valued products in a sustainable manner (Loehle *et al.* 2009; Richardson 1994; Walbridge 1993). Therefore, understanding changes in the area, distribution, and functional status of FWs is crucial.

Federal agencies in the U.S. monitor land cover change (including FWs) with different remote sensing systems and areas of emphasis. Three such programs are the Multi-Resolution Land Cover Characteristics Consortium (MRLC), the National Resources Inventory (NRI), and the National Wetlands Inventory (NWI). The MRLC produces periodic land cover data (National Land Cover Data base [NLCD]) for the conterminous U.S. using 30 m resolution satellite imagery and includes a land cover category of "woody wetland". The NRI program of the Natural Resources Conservation Service publishes periodic reports on land-based natural resources on nonfederal lands using a sample of aerial photo plots. The NWI program of the U.S. Fish and Wildlife Service (USFWS) produces both a complete inventory (polygon map) of wetlands in the conterminous U.S. and periodic Status and Trends (S&T) reports documenting changes observed on photointerpreted sample blocks. The wetlands map produced by NWI is often considered the standard source of information about wetlands extent, due to the extensive coverage in the United States and the program focus on wetlands.

Mapping FWs with remote sensing poses significant challenges. The National Research Council (NRC) noted that mapping of FWs is difficult due to foliage obscuring the ground and, because

for most of the year, the water table is below the ground surface (NRC 1995). This statement is echoed by Tiner (1997), who reported that FWs are "conservatively mapped" due to these difficulties, and that temporarily flooded or seasonally saturated FWs may not appear on NWI maps especially along the Coastal Plain, where many of the FWs in the southern U.S. are located.

Given the difficulties in mapping FWs, it is important to assess and report accuracy and reliability of change detection. Accuracy assessment, reported quantitatively in standard formats, is needed to provide evidence that reported differences are beyond those that might be expected from sampling error, photointerpretation (classification) error, or boundary (delineation) uncertainty.

Despite the importance of wetlands information, there are few current, large-area, quantitative assessments of wetlands map accuracy. In many of the published studies, comparisons are made between wetlands delineated according to different definitions (e.g., Stolt and Baker 1995; Morrissey and Sweeney 2006; Gage, Cooper, and Lichvar 2020). Furthermore, many studies are focused on a narrow geographic scope (Stolt and Baker 1995; Kudray and Gale 2000; Morrissey and Sweeney 2006).

Nichols (1994) examined NWI accuracy in Maine using point intercept transects involving a total of 1800 sample points, reporting an overall accuracy of 95%. Nearly all of the wetlands identified in the field that were omitted in the NWI map were FWs. Kudray and Gale (2000), in a study in a national forest in Michigan involving 148 field plots, reported all nonforested wetlands (NFWs) were identified correctly, as were slightly over 90% of FWs. In a 20 000-ha area in Vermont, Morrissey and Sweeney (2006) found that NWI underestimated FW area by 64%, and overall wetland area by 39%.

There are two components crucial to understanding the reliability of a polygon map product such as NWI: (1) the accuracy of the classification of individual polygons and (2) the uncertainty of areas derived from polygon delineation. We sought to address these components through a comprehensive analysis of uncertainty in FW maps using an extensive validation data set. Specifically, our objectives were to: (1a) characterize the level of classification agreement between an aerial photo-based map of FWs and a field sample; (1b) assess the impact of spatial uncertainties and temporal mismatch on classification agreement; (1c) examine patterns of disagreement across forest conditions such as forest type, stand age, and physiographic class; and (2) develop estimates of delineation uncertainty for photo-delineated wetland polygons (Figure 1). We addressed classification agreement using data from NWI as the remote sensing source, and data from the U.S. Forest Service Forest Inventory and Analysis (FIA) program as a field validation data set. To assess delineation uncertainty, we conducted an epsilon band analysis using the NWI polygons.

Stephen P. Prisley is with the National Council for Air and Stream Improvement, 541 Washington Ave. SW, Roanoke, VA 24016 sprisley@ncasi.org.

Jeffery A. Turner, Mark J. Brown, and Samuel G. Lambert are with the U.S. Forest Service Southern Research Station, 4700 Old Kingston Pike, Knoxville, TN 37919.

Erik Schilling is with NCASI, 104 East Bruce St., Aubrey, TX 76227.

Photogrammetric Engineering & Remote Sensing
Vol. 86, No. 10, October 2020, pp. 609–617.
0099-1112/20/609–617

© 2020 American Society for Photogrammetry
and Remote Sensing
doi: 10.14358/PERS.86.10.609

Wetland Definitions

The first challenge in comparing estimates of FW area is to ensure consistency in wetland definitions. Most wetlands definitions involve some combination of three criteria: vegetation, soils, and hydrologic conditions (Federal Interagency Committee on Wetland Delineation 1989). The NRI and NWI use a definition from the Cowardin *et al.* (1979) classification system for wetlands:

Wetlands are lands transitional between terrestrial and aquatic systems where the water table is usually at or near the surface or the land is covered by shallow water. For purposes of this classification wetlands must have one or more of the following three attributes: (1) at least periodically, the land supports predominantly hydrophytes; (2) the substrate is predominantly undrained hydric soil; and (3) the substrate is nonsoil and is saturated with water or covered by shallow water at some time during the growing season of each year.

Therefore, for NWI mapping purposes, at least one of the three wetland elements must be present. This definition is more inclusive than that used for regulatory compliance within Section 404 of the Clean Water Act, which is based on the Federal Interagency Committee on Wetland Delineation (1989). This definition (herein referred to as the FICWD definition) requires all three components (hydrophytic vegetation, hydric soils, and wetland hydrology) to be present for an area to be defined as a wetland. Therefore, comparisons between wetlands mapped by NWI and wetlands mapped according to the FICWD definition (such as in Gage, Cooper, and Lichvar 2020) will usually find some discrepancies that can be attributed to definition rather than accuracy of the mapping process.

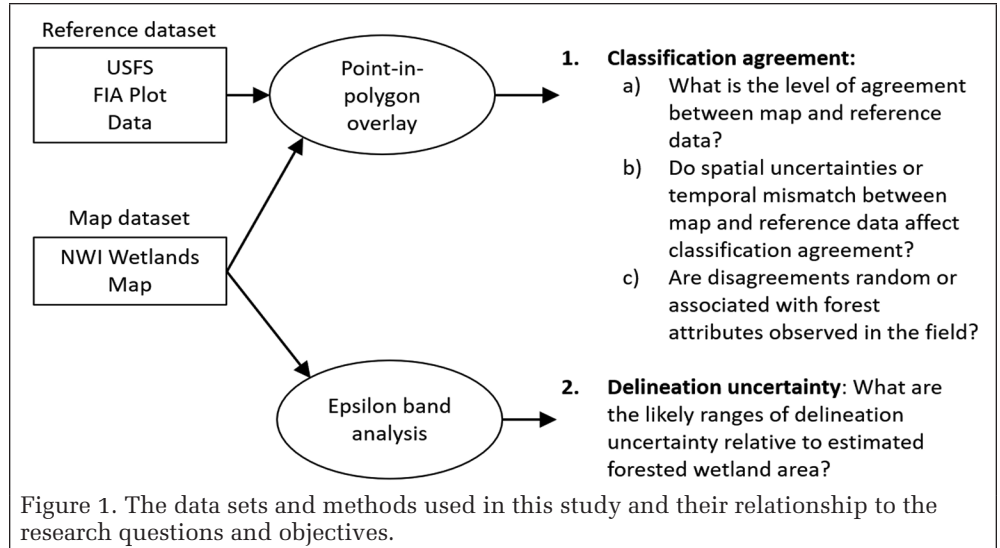
Forested wetlands are defined as wetlands characterized by forest cover, which requires dominance by trees (woody stems ≥ 12.7 cm diameter at 1.4 m above ground and at least 6 m in height). In the Cowardin *et al.* (1979) system, palustrine forested (PFO) and palustrine shrub-scrub (PSS) are the categories closely associated with FWs; the distinction between PFO and PSS can be simply a difference in seral stage. For the purposes of this study, we use the term FW to include any subcategory of PFO or PSS wetlands. All other land cover types (including both nonwetlands and wetlands other than PFO and PSS) are referred to herein as NFW.

Quantifying Uncertainties in Wetland Mapping from Remotely Sensed Imagery

The importance of accuracy assessment for estimating land cover change is underscored by Olofsson *et al.* (2014) who note that quantitative accuracy statements are needed to support confidence in products and in inferences made from them. Three primary components of uncertainty in wetland area change merit attention: (1) sampling error, (2) classification accuracy, and (3) delineation uncertainty.

Sampling Error

The NWI inventory map completely covers the conterminous U.S., so it represents a census or complete enumeration of wetlands; sampling error is not a factor. However, when change estimates (such as from NWI S&T or NRI) are derived from a



statistical sample (rather than complete enumeration), sampling error can indicate the uncertainty expected due to random chance in drawing the sample. Error from well-designed sampling efforts can be described from common statistical estimates such as standard errors, coefficients of variation, and confidence intervals that are based on characteristics of the sampling design and sample size. Dahl (2011, Appendix D) reported that based on the NWI status and trends sample of 5042 plots, 62 008 ha of palustrine FW changed to “upland forested plantation” during 2004–2009, with a coefficient of variation of 20% (corresponding to a 95% confidence interval of about $\pm 39.2\%$). Similarly, NRI reported (USDA 2015) that based on a sample of over 300 000 segments, 83 365 ha of palustrine and estuarine wetlands on nonfederal lands changed to upland between 2002 and 2007, with a 95% confidence interval of $\pm 28.9\%$. It should be noted that these confidence intervals reflect only sampling error; they do not include uncertainty based on misclassification or variability in delineation, and therefore represent a minimum level of uncertainty embodied in sample-based estimates of land cover change.

Classification Accuracy

The next component of uncertainty in wetlands mapping involves the ability to accurately assign land cover classes to mapped objects (points, pixels, or polygons). The literature on measuring and communicating classification accuracy is extensive, and the fundamental requirement is a contingency table (error matrix) that quantifies agreement between image points and reference data (Congalton 1991; Congalton and Green 2008; Olofsson *et al.* 2014). Commonly used metrics describing classification accuracy include percent correctly classified, and user’s and producer’s accuracy for individual classes (percentage of map classes and reference classes, respectively, that are correctly classified) (Story and Congalton 1986).

Standards for wetlands mapping identify minimum acceptable levels of classification accuracy. The USFWS (2004) states that maps must have 95% classification accuracy at the Cowardin Class level (e.g., PFO/PSS) to be considered acceptable. For NWI status and trends mapping as well, required accuracy is 95% (Dahl and Bergeson 2009; NSST 2017). The Federal Geographic Data Committee (FGDC) differentiates between “feature accuracy” (e.g., wetland versus upland) and “attribute accuracy” (e.g., individual wetlands class) (FGDC 2009). For feature accuracy, FGDC calls for 98% accuracy, and specifies 85% accuracy for the wetlands class.

Delineation Uncertainty

When wetland area is determined from polygons delineated from aerial photography, quantifying delineation uncertainty can inform users of the range in area estimates that might be expected from variability in the delineation process. The process of manual delineation of land cover polygons from interpretation of aerial photographs may involve multiple sources of uncertainty, including image registration (Dai and Khorram 1998; Hughes, McDowell, and Marcus 2006), variation between photointerpreters (Prisley and Luebbing 2011; Pengra *et al.* 2020), the nature of the boundary (crisp versus diffuse), the quality of the imagery, the shape of the features (complex or simple), and the sizes of features (perimeters and areas).

Accuracy standards have been developed for wetlands delineation. The USFWS (2004) states that wetland boundaries must be delineated within 33 feet (10 meters) of their location. Dahl and Bergeson (2009) called for image analysts to strive for “approximation of geographical position within 10 m”. Similarly, FGDC (2009) suggested a horizontal positioning accuracy (root-mean-square error) of 5 m for palustrine wetlands in the conterminous U.S. In a test of the accuracy of wetland boundary delineation, Barrette, August, and Golet (2000), using relatively large-scale (1:7200) aerial photographs, found that only 75% of tested delineations were within 6 m of the field boundary location. Such assessments of boundary delineation that involve field verification are rare, meaning other approaches for quantifying uncertainty are needed.

One way to quantify the effect of boundary delineation uncertainty on polygon area is to use error-band models (Wernette *et al.* 2017). A variety of such models are described by Shi (2010) and Foy *et al.* (2015). The simplest is the epsilon band model that represents an error band as a buffer (with radius denoted as epsilon) around a vector object (point, line, or polygon). Conceptually, the error band can be treated as a spatial confidence interval for an area estimate (Foy *et al.* 2015): if 95% of points along a boundary are within epsilon distance (e.g., 5 m) of a “true” line, then the epsilon band area is analogous to the size of a 95% confidence interval on polygon area. For example, consider an FW polygon from the Florida NWI map (Figure 2). An epsilon band of 10 m width (5 m to the inside and 5 m to the outside) comprises 2.06 ha, or 22% of the polygon area of 9.2 ha. In this way, the epsilon band model can relate statements about boundary delineation accuracy (e.g., 5 m) to an area interval that may be interpreted as a reasonable range of uncertainty (e.g., $\pm 11\%$).

Methods

Data Sets

Forest Inventory and Analysis Plots

Field data came from inventories by the U.S. Forest Service’s FIA program in the 1990s. The FIA program has collected field measurements of forest conditions at sample plots across the U.S. since the 1940s. Currently, plots are located using a stratified random sampling design with an intensity of one plot per approximately 2400 ha (Bechtold and Patterson 2005). While publicly available plot locations are perturbed for privacy considerations, our analysis used actual coordinates as recorded by FIA.

The 1990s inventories in five southeastern U.S. states (Florida, Georgia, South Carolina, North Carolina, and Virginia) included a field determination of wetland status at each timberland plot; this was the only region in the country to do so. Timberland refers to forest land capable of producing $1.4 \text{ m}^3 \text{ ha}^{-1} \text{ yr}^{-1}$ of industrial wood and not withdrawn from timber use; this definition excludes some FWs withdrawn from use due to their location within National Parks or National Fish and Wildlife Refuges (such as the Great Dismal Swamp in Virginia or the Okefenokee Swamp in Georgia). Field procedures

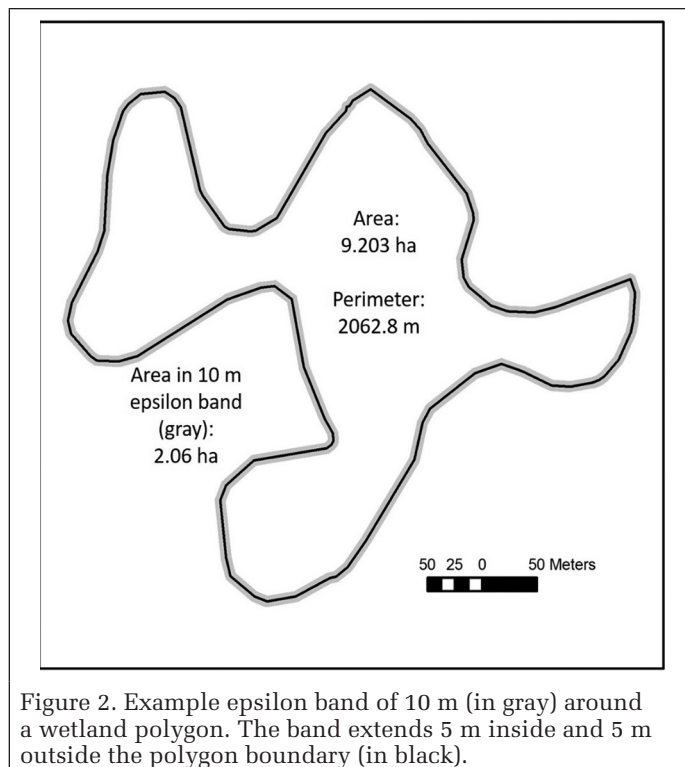


Figure 2. Example epsilon band of 10 m (in gray) around a wetland polygon. The band extends 5 m inside and 5 m outside the polygon boundary (in black).

for wetland classification followed the Federal Interagency Committee for Wetland Delineation (1989) standard (Brown, Smith, and McCollum 2001). Field crews recorded the presence or absence of each of the three wetland indicator components: hydrophytic vegetation, hydric soils, and wetland hydrology. Summaries of these inventories, including land areas, ownership and forest types, timber growth and harvest, and other data, including sampling error estimates are reported in Brown, Smith, and McCollum (2001). Wetland determination is no longer part of the FIA field sampling protocol.

National Wetlands Inventory Maps

We used the NWI map product as the source of photo-derived wetland boundaries. The NWI map is publicly available as digital vector spatial data by state or watershed and includes extensive metadata, including date, type, and scale of imagery used for mapping. National Wetlands Inventory mapping of wetlands builds on a widely adopted classification system (Cowardin *et al.* 1979) and standards for data quality (USFWS 2004; FGDC 2009). While revisions and updates to the NWI map are made when possible, much of the wetlands delineation in the southeastern U.S. is based on aerial imagery acquired prior to the 1990s. For change estimation, a similar but distinct program within USFWS known as “Status and Trends” uses aerial photography of thousands of sample blocks (each approximately 1036 ha) for periodic determination of wetland change (Dahl and Bergeson 2009; NSST 2017). Delineations at the block level are not publicly available, nor are summaries by state or geographic region provided in the program reports (e.g., Dahl 2000; Dahl 2006; Dahl 2011). Because the same types of imagery and photointerpretation guidelines are used for both the NWI map and S&T mapping, results from our analysis should apply equally to both.

Classification Accuracy

We assessed classification agreement by tabulating the NWI class occurring at FIA plot locations through spatial overlay. While assessments of field plot data reported by Brown, Smith, and McCollum (2001) and Brown (1997) used the FICWD (1989) definition for wetland, for consistency with the NWI map we used the NWI definition to assign plots as either

Table 1. FIA plot coordinate confidence ratings and uncertainty distances assigned.

| Coordinate confidence | Description | Number of plots | Uncertainty distance (m) |
|-----------------------|--|-----------------|--------------------------|
| HIGH | Locations collected with GPS during subsequent inventories | 11 197 | 10 |
| MEDIUM | Locations digitized from larger scale photographs with higher precision | 4924 | 50 |
| LOW | Locations digitized from smaller scale photographs with low precision, or from other sources | 9609 | Not used |

FW or NFW. For the NWI data, we considered areas mapped as PFO or PSS as FW, and anything else as NFW.

Classification accuracy was assessed using standard metrics from cross-tabulation of plots by reference class (columns) and map class (rows). Thus, FIA field data represented the reference data set being compared to map classes and were used this way in expression of user's accuracy and producer's accuracy.

To address research objective 1b (Figure 1), we tabulated classification agreement using two spatial overlay approaches. A "simple overlay" approach used direct spatial overlay of the FIA plot centers with the NWI polygons. Because spatial overlay of disparate data sets for comparative purposes should consider spatial uncertainties in each layer, we incorporated uncertainty using a "probable overlay" approach as described below.

Spatial Uncertainties

Plot locations in the 1990s were recorded by FIA by digitizing pinprick locations on hardcopy aerial photographs. Based on the scale of the imagery and the challenge of precisely locating plots within large blocks of forest, FIA staff estimated that locations were likely reliable within about 50 m. Many of the plots measured in the 1990s were later incorporated in the subsequent FIA annual survey design, and eventually had locations recorded in the field using Global Positioning System (GPS) receivers. An early field test of spatial accuracy of GPS receivers used by FIA reported average errors of about 8 m, with maximum errors up to 20 m (Jasumback 1996; McRoberts *et al.* 2002). For this study, plots were assigned a coordinate confidence class based on the best information available from FIA staff and records (Table 1). The coordinates recorded for many plots in the LOW confidence class placed them in areas known not to be timberland (e.g., offshore, in bays, and estuaries). Therefore, we restricted our overlay analysis to plots with MEDIUM or HIGH coordinate confidence; this resulted in using 16 121 out of 25 730 timberland plots.

We evaluated the combined impact of spatial uncertainty by buffering FIA plot locations with a variable radius that incorporated uncertainty from both FIA plot locations and NWI wetland boundaries. The radius included the plot uncertainty distances from Table 1 and NWI boundary uncertainties as described below.

For NWI polygons, we used metadata from the NWI map data set, which included the scale and date of imagery that was used to map each quadrangle. Image scale varied widely over time and across the region (Table 2). About 75% of field points were in areas where the NWI mapping was based on imagery collected prior to 1990, and at scales smaller than 1:40 000. After 2000, most imagery used in NWI was at a scale of 1:20 000 or larger. Because image scale/resolution has an influence on the ability to accurately map locations from an image, we assumed a relationship between image scale and the uncertainty distance chosen for the NWI polygon boundaries. Using a 10 m uncertainty value for images at 1:20 000 coincides with the FGDC (2009) standard and represents the predominant image scale in use at the time the standard was developed. We assumed a linear relationship between image scale and uncertainty distance, such that polygons derived from 1:40 000 imagery were assigned a value of 20 m, etc. This relationship (1 m uncertainty per 2000 image scale units) represents a location uncertainty of 0.5 mm at image scale.

Table 2. Numbers of FIA plots by scale and decade of imagery used for NWI mapping of locations in the field sample.

| Image scale 1: | Decade | | | | | TOTAL |
|-------------------|--------|--------|-------|-------|-------|--------|
| | 1970s | 1980s | 1990s | 2000s | 2010s | |
| Less than 20 000 | 0 | 0 | 26 | 1083 | 841 | 1950 |
| 20 000–39 999 | 0 | 0 | 39 | 0 | 0 | 39 |
| 40 000–59 999 | 3 | 11 471 | 1459 | 561 | 0 | 13 494 |
| 60 000–79 999 | 250 | 7 | 54 | 0 | 0 | 311 |
| 80 000 or greater | 327 | 0 | 0 | 0 | 0 | 327 |
| TOTAL | 580 | 11 478 | 1578 | 1644 | 841 | 16 121 |

For each plot, we added the uncertainty distance for the plot (Table 1) to the boundary uncertainty based on image scale to get a total uncertainty distance. We then buffered plot locations using the total uncertainty distance to obtain circles representing the area that we considered as including both plot location and wetland boundary uncertainty.

For the probable overlay approach, we computed proportions of the circles in each NWI mapped class (FW, NFW) as representing the probability that the plot landed in the class. To illustrate our reasoning, consider an FIA plot that was determined to be FW in the field (Figure 3). This plot was located with medium confidence (50 m uncertainty) in an area where the NWI delineations were made from imagery at a scale of 1:40 000 (20 m uncertainty). The plot was buffered at a radius of 70 m, resulting in a 1.54 ha circle. We consider this circle as containing the likely locations of the plot relative to the wetland boundary, given the recorded plot location and our estimate of location uncertainty. If we assume a uniform probability distribution of possible plot locations across this circle, then the proportion of area within each class

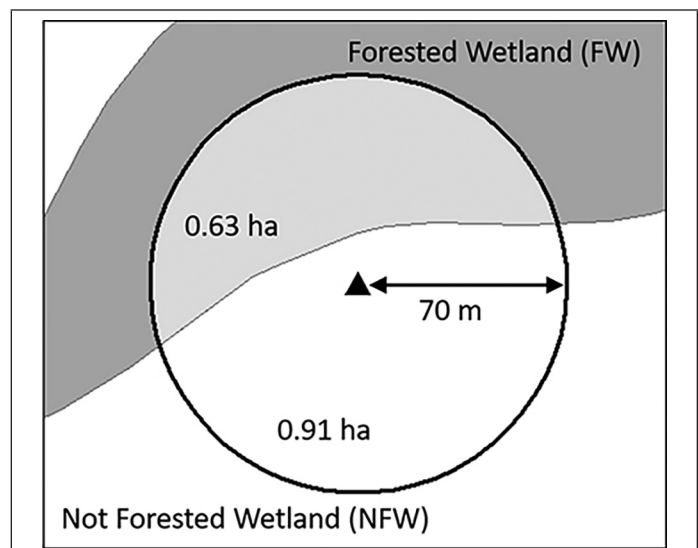


Figure 3. Example of probable overlay of a wetland FIA plot (triangle) on NWI wetland map (gray polygon). The circle represents an uncertainty radius of 70 m. A uniform distribution of possible plot locations within this zone results in a probability of agreement of 0.41 (0.63/1.54).

represents the probability that the plot fell within the class. While a uniform probability distribution is less likely than a bivariate normal probability ellipse (Shi 2010), it is much easier to evaluate mathematically, and was therefore chosen as a simplifying assumption.

With simple overlay, the FW plot in Figure 3 fell just outside an FW boundary, indicating disagreement. However, within the uncertainty circle, 41% of the area was mapped as FW and 59% as NFW. Thus, we would expect a 0.41 probability of agreement that the FIA plot landed in an NWI FW. There was then a 0.59 probability of disagreement. In tabulating this plot in a contingency table, we recorded it as 0.41 for FIA:FW/NWI:FW and 0.59 for FIA:FW/NWI:NFW. Cells in the resulting contingency table represented the summed probabilities that plots observed in the field (column class) matched the mapped (row) class.

Temporal Disagreement

Because field inventory and aerial photo acquisition were not simultaneous, it is possible that some observed disagreement was due to temporal change in wetland status. Thus, we needed to consider the likelihood of change in wetland conditions between field sampling and aerial photo dates. We chose to establish a null hypothesis that FWs in the study area were experiencing net loss rates comparable to the national averages reported in the status and trends reports (Dahl 2000; Dahl 2006; Dahl 2011). We then compared the disagreements observed in our data to disagreements expected under this null hypothesis. Using the change matrices reported in the status and trends reports, we found that national net losses from FWs (PFO and PSS) to other classes (NFW) occurred at annual rates of 0.01% yr⁻¹ from 1986 to 1997, 0.08% yr⁻¹ from 1998 to 2004, and 0.13% yr⁻¹ from 2004 to 2009. For this analysis, we conservatively set the null hypothesis to assume the most extreme rate of wetland loss reported by status and trends of 0.13% yr⁻¹. We then examined the disagreement that would be expected due to temporal change in wetland status and compared it to the disagreement observed; if the observed rates of disagreement were similar to those expected under the null hypothesis, then attributing disagreement to temporal differences rather than to misclassification was supported.

Characterizing disagreements: To identify patterns in disagreement across forest conditions, we tabulated misclassified plots by variables from the plot data. These variables included the age of the forest at the time of the imagery, the physiographic class recorded for the plot (e.g., various classes of xeric, mesic, and hydric physiography), the broad forest type of the plot (upland hardwood, bottomland hardwood, pine, and mixed pine-hardwood), and the stand origin (planted or naturally regenerated). We performed chi-squared goodness-of-fit tests to determine if the observed distribution of misclassifications was different than would be expected if misclassification occurred proportional to class membership.

Delineation uncertainty: We chose the epsilon band model (Shi 2010; Wernette *et al.* 2017) as a simple characterization of the delineation uncertainty for the polygons in the five-state study area. First, NWI FWs were dissolved at the class level to eliminate boundaries between adjacent polygons belonging to the same class (e.g., PFO and PSS, such boundaries being irrelevant in FW area computation). Epsilon band area was then defined as the area contained within an outside and inside buffer, each of radius epsilon, around the resulting FW polygons.

The area within a buffer distance of a line (such as a polygon boundary) is approximately equal to the line length (e.g., polygon perimeter) times the buffer width. Thus, a close approximation to the area within an epsilon band around wetland polygons can be obtained by simply multiplying total wetland perimeter by twice epsilon (for an inner and outer

buffer). For example, the area in the epsilon band in Figure 2 could be approximated by total bandwidth (10 m) multiplied by the polygon perimeter (2062.8 m), resulting in an approximated epsilon band area of 20 628 m². Epsilon band area for this polygon, as measured by geographic information system (GIS) buffer operations, was 20 612 m², a difference of less than 0.1%. This approximation is straightforward and is expected to yield results comparable to the epsilon band area that would be obtained by buffering all FW polygons. Buffering of the large set of complex NWI polygons (1.4 million polygons across five states) frequently failed in our GIS system, possibly due to computer memory or other limitations. For simplicity in this approximation, we chose to use a single epsilon width for all polygons, rather than a differing epsilon width based on image scale as used in the classification accuracy assessment; such a detailed analysis would require splitting all polygons along photo boundaries (for cases in which adjacent photos were of different scales) and applying the image-based epsilon band width to portions of polygons within different photos.

We chose an epsilon value of 5 m based on the FGDC standard for horizontal error in wetlands data sets (FGDC 2009). This may be an optimistic estimate, as other standards specified an accuracy of 10 meters (USFWS 2004; Dahl and Bergeson 2009), and this standard was not met in the wetlands mapping test conducted by Barrette, August, and Golet (2000). In guidelines for the wetlands change detection mapping in the S&T program (Dahl and Bergeson 2009; NSST 2017), analysts are instructed to perform on-screen edits at a scale of 1:7000 to 1:10 000. At this scale, a 5 m ground distance is 0.5 to 0.7 mm on the computer screen. Thus, standards calling for accuracy within 5 m expect that analysts will be able to capture boundaries to a tolerance of about half a millimeter while digitizing from photos on the computer screen. For these reasons, an epsilon value of 5 m may be viewed as a best-case threshold for delineation uncertainty.

Performance of this approximation was then tested by comparison to buffers around 1000 randomly selected FW polygons from each state. Delineation uncertainty is then expressed as epsilon band area as a percentage of total FW area.

Results

Classification Accuracy

Agreement between field plots and the NWI map, based on simple overlay and probable overlay, is reported in Table 3. Because cells in the probable overlay table are summed probabilities, they take on decimal values, but column totals (numbers of plots) remain the same.

Table 3. Contingency tables showing number of plots by FIA field determinations and NWI photo-derived wetland determinations based on two overlay techniques.

| NWI map determination | FIA field determination: Simple overlay | | | FIA field determination: Probable overlay | | |
|-----------------------|---|------|--------|---|--------|----------|
| | FW | NFW | TOTAL | FW | NFW | TOTAL |
| FW | 2716 | 278 | 2994 | 2642.2 | 293.9 | 2936.1 |
| NFW | 4202 | 8925 | 13 127 | 4275.8 | 8909.1 | 13 184.9 |
| Total | 6918 | 9203 | 16 121 | 6918.0 | 9203.0 | 16 121.0 |

Based on these tables, summary metrics are presented in Table 4. Percent overall agreement and user's and producer's accuracy for the individual classes are computed as in Story and Congalton (1986).

Temporal Disagreement

Imagery used for NWI mapping at field plot locations ranged in acquisition year from 1972 to 2014. We report a variable "YR-SAFTER" as the year of inventory for a plot minus the year of

image acquisition for NWI mapping at the plot location. Thus, a plot in Georgia measured in 1997 that coincided with a portion of the NWI map based on 1982 aerial photography would have YRSAFTER = 15. For our data, YRSAFTER ranged from -23 to 23, with about 18% of plots having field and image data collection within five years of each other (Table 5). Over three quarters of plots were measured after the date of imagery used in mapping the wetlands at their location.

Table 4. Summary classification accuracy metrics for two ways of tabulating agreement (all values in percent).

| | Simple overlay | Probable overlay |
|---------------------------|----------------|------------------|
| Percent overall agreement | 72.2 | 71.7 |
| User's accuracy: FW | 90.7 | 90.0 |
| User's accuracy: NFW | 68.0 | 67.6 |
| Producer's accuracy: FW | 39.2 | 38.2 |
| Producer's accuracy: NFW | 97.0 | 96.8 |

Table 5. Differences in year of FIA field inventory and year of image acquisition for NWI mapping.

| Inventory year was: | Number of plots | Mean YRSAFTER |
|--|-----------------|---------------|
| >10 years prior to image year (YRSAFTER < -10) | 1444 | -17.3 |
| 6 to 10 years prior to image year (YRSAFTER -6 to -10) | 1041 | -9.1 |
| 1 to 5 years prior to image year (YRSAFTER -1 to -5) | 1152 | -1.3 |
| The same as image year (YRSAFTER = 0) | 20 | 0.0 |
| 1 to 5 years after image year (YRSAFTER 1 to 5) | 1753 | 3.5 |
| 6 to 10 years after image year (YRSAFTER 6 to 10) | 4162 | 7.9 |
| More than 10 years after image year (YRSAFTER > 10) | 6549 | 14.7 |

YRSAFTER was calculated as year of field inventory minus year of imagery.

Table 6. Contingency table of plots for which FIA inventory was more than 10 years prior to image acquisition, using simple overlay.

| | | FIA Field Determination (Time 1) | | |
|---------------|-------|----------------------------------|-----|-------|
| | | FW | NFW | TOTAL |
| NWI map | FW | 466 | 26 | 492 |
| determination | NFW | 498 | 454 | 952 |
| (Time 2) | TOTAL | 964 | 480 | 1444 |

Table 7. Summary of temporal differences (numbers of plots) observed and expected under a null hypothesis of annual wetland loss of 0.13%.

| YRSAFTER | Number of plots | t1 FW plots | Plots FW t1 and NFW t2 | Plots NFW t1 and FW t2 | Observed net loss* | Expected net loss** |
|-----------|-----------------|-------------|------------------------|------------------------|--------------------|---------------------|
| <-10 | 1444 | 964 | 498 | 26 | 472 | 22 |
| -10 to -6 | 1041 | 448 | 296 | 22 | 274 | 5 |
| -5 to -1 | 1152 | 723 | 441 | 21 | 420 | 1 |
| 0 | 20 | NA | NA | NA | NA | NA |
| 1 to 5 | 1753 | 290 | 11 | 743 | -732 | 1 |
| 6 to 10 | 4162 | 470 | 31 | 1182 | -1151 | 5 |
| >10 | 6549 | 1262 | 167 | 1035 | -868 | 24 |

YRSAFTER is computed as the inventory year minus the imagery year, so when YRSAFTER is negative, FIA plots represent time 1 (t1) and NWI delineations represent time 2 (t2).

*Computed as number of plots that were FW at time 1 and NFW at time 2, minus plots that were NFW at time 1 and FW at time 2. Negative net loss represents net gain of FW from NFW.

**Expected net loss is computed as an annual rate of 0.13% yr⁻¹ times the mean YRSAFTER value from Table 5 times the number of time 1 FW plots.

To determine potential temporal disagreement between field and photo determinations, we examined contingency tables of subsets of plots with ranges of elapsed time between field inventory and photo acquisition. As an example, considering just the 1444 plots for which the inventory year was more than 10 years prior to the image year (first row in Table 5), the mean difference between inventory and image years was 17.3 years. These plots were tabulated in contingency table form (using simple overlay) (Table 6). In this case, we see 498 plots representing FW at time 1 (FIA) and NFW at time 2 (NWI), offset by 26 plots that were NFW at time 1 and FW at time 2. This would represent an apparent net loss of FW to NFW of 472 plots, or 49% of the time 1 FW sample. Under the null hypothesis, we would expect to see 17.3 years of annual FW net loss of 0.13% yr⁻¹, or 2.25%, which would be about 22 plots. Therefore, for this case, we expected 22 plots exhibiting net loss under the null hypothesis and observed 472 (Table 7). Substantial discrepancies in Table 7 between observed net losses and those expected under a temporal change null hypothesis suggest that the temporal lag between field visits and photo acquisition does not explain the disagreements observed. We note that whenever field inventory preceded photo acquisition, we observed high apparent net loss. Whenever field inventory followed image acquisition, we observed high levels of apparent net gain.

Furthermore, if temporal differences between field inventory and image acquisition were responsible for disagreements between the two, we would expect to see agreement decrease as temporal differences increased. In fact, there is no strong trend in decreasing agreement, rather higher levels of agreement associated with longer temporal differences (Table 8).

Table 8. Classification agreement (percent correctly classified) by temporal differences between field inventory and image acquisition (using simple overlay).

| Temporal difference | Number of plots | % correctly classified |
|---------------------|-----------------|------------------------|
| 0 years | 20 | 65.0 |
| 1-5 years | 2905 | 58.1 |
| 6-10 years | 5203 | 70.6 |
| 11-15 years | 4012 | 76.2 |
| 16-20 years | 3697 | 89.8 |
| >20 years | 284 | 74.6 |

Characterizing Disagreements

Using the results from simple overlay analysis, we tabulated numbers of misclassified plots by forest condition variables from the FIA plot data. Chi-squared goodness-of-fit tests were conducted to determine if misclassifications occurred as would be expected under random assignment (Table 9).

Delineation Uncertainty

An approximate estimate of delineation uncertainty was computed as the area within a band of 10 m width ($2 \times \text{epsilon}$) around the perimeter of FW polygons in the NWI data set. Performance of this approximation was tested by buffering 1000 randomly selected FW polygons per state with a radius of epsilon (5 m) (Table 10). Across the study region, the approximated epsilon area was within 3% of the area derived by buffering polygons. Adjustment factors (buffered area divided by approximate area) were derived and applied to approximated epsilon area for each state (Table 11). The area within the 10 m epsilon band around FW polygons ranged from about 15 to 30% of FW area, and averaged 17.5% across the southeastern U.S. Thus, we could state that FW area in the five-state region was 8 million ha with delineation uncertainty of $\pm 705\,000$ ha (8.8%).

Discussion

Objective 1a: Level of Classification Agreement

All accuracy measures (overall, producer's, and user's) for both overlay approaches were below the levels called for in the various standards (USFWS 2004; FGDC 2009; Dahl and Bergeson 2009; NSST 2017), even at the "feature" (upland/wetland) level evaluated here.

Table 9. Results of chi-squared goodness-of-fit tests comparing misclassification frequency across classes of forest condition variables.

| Variable | df | Chi-squared value | Disagreement higher than expected in: |
|---------------------|----|-------------------|--|
| Stand age class | 8 | 338.98 | Younger stands (age < 30) |
| Physiographic class | 11 | 1456.62 | Flat areas outside floodplains (flatwoods) |
| Broad forest type | 3 | 322.08 | Pine forest types |
| Stand origin | 1 | 269.53 | Planted stands |

df = degrees of freedom. All variables had $p < 0.0005$.

Table 10. Comparison of approximate and buffered epsilon analysis for 1000 FW polygons selected randomly from each state.

| State | Forested wetland area (ha) | Perimeter (m) | Approx. epsilon area (ha) | Buffered epsilon area (ha) | Adjustment factor |
|-----------|----------------------------|---------------|---------------------------|----------------------------|-------------------|
| Fla. | 13 392 | 2 017 965 | 2018 | 2011 | 0.9964 |
| Ga. | 15 645 | 2 507 859 | 2508 | 2427 | 0.9678 |
| N.C. | 11 082 | 1 984 186 | 1984 | 1903 | 0.9591 |
| S.C. | 14 496 | 1 815 442 | 1815 | 1778 | 0.9792 |
| Va. | 2519 | 992 245 | 992 | 950 | 0.9569 |
| SOUTHEAST | 57 134 | 9 317 696 | 9318 | 9068 | 0.9732 |

Approximate epsilon area is epsilon band width (10 m) times total perimeter. The adjustment factor is the buffered epsilon area divided by the approximate area. (Fla. = Florida, Ga. = Georgia, N.C. = North Carolina, S.C. = South Carolina, Va. = Virginia.)

Table 11. Summary of delineation uncertainty analysis for NWI FWs in each state.

| State | Number of polygons* | Area (ha) | Perimeter (m) | Approx. epsilon area (ha) | Adjusted epsilon area (ha) | Adj epsilon area (percent) |
|-----------|---------------------|-----------|---------------|---------------------------|----------------------------|----------------------------|
| Fla. | 269 463 | 2 822 215 | 407 517 353 | 407 517 | 406 034 | 14.4 |
| Ga. | 220 254 | 1 964 809 | 411 457 723 | 411 458 | 398 195 | 20.3 |
| N.C. | 114 060 | 1 540 269 | 247 954 462 | 247 954 | 237 819 | 15.4 |
| S.C. | 184 513 | 1 299 850 | 253 047 514 | 253 048 | 247 772 | 19.1 |
| Va. | 128 902 | 414 604 | 128 208 336 | 128 208 | 122 685 | 29.6 |
| SOUTHEAST | 917 192 | 8 041 747 | 1 448 185 388 | 1 448 185 | 1 409 347 | 17.5 |

Adjusted epsilon area is the approximate area multiplied by the appropriate adjustment factor from Table 10 and expressed in the last column as percent of total wetland area. (Fla. = Florida, Ga. = Georgia, N.C. = North Carolina, S.C. = South Carolina, Va. = Virginia.)

*Following dissolving by FW class (PFO/PSS).

It is apparent that field observation resulted in substantially more wetland determinations than did the aerial photo-based process employed for the NWI map; FIA recorded 2.3 times as many plots as wetland than did the NWI map. This is consistent with Tiner's (1997) statement that:

By current design, NWI maps tend to err more by omission (Type I error) than by commission (Type II error). This means that if an NWI map indicates the presence of wetland in a given area, it is highly likely that a wetland is there... Conversely, if an NWI map does not indicate a wetland, one is usually not there, but users should not be surprised to find unmapped wetlands, especially drier-end wetlands and wetlands that are difficult to photo-interpret (such as certain evergreen forested wetlands, farmed wetlands, mowed and grazed wetlands, and significantly drained wetlands).

Similarly, NRC (1995) noted that NWI maps were less inclusive of wetlands than other maps, citing several studies that found wetland areas not mapped by NWI.

Some underclassification of FWs may be due to the baseline assumptions used in mapping change. In a technical procedures document (Dahl and Bergeson 2009), S&T mappers were instructed to assume that pine (*Pinus* spp.) plantations are not wetland unless specific, visible evidence indicates otherwise. However, such evidence may be rare when wetland signatures such as surface water are obscured by forest canopies, especially in evergreen stands or when photography is taken in a leaf-on condition. Indicators such as hydric soils, hydrophytic understory vegetation, and even surface water may be obscured under a closed forest canopy. If mapping at one time is done without a forest canopy (e.g., a young forest stand prior to canopy closure), when water or wet soil is visible, and compared to a later aerial photograph with no evidence of wetland hydrology, it could be easy to assume the area has lost wetland characteristics.

The default assumption that planted forest is not wetland is reflected in the S&T reports which include a forested plantation

subclass of upland (nonwetland), implying that all forested plantations are uplands (there is no forested plantation class in the freshwater wetlands grouping) (Dahl 2000; Dahl 2006; Dahl 2011). To the contrary, Brown, Smith, and McCollum (2001), reported that 768 500 ha of pine plantation in the five southeastern states were field-determined to be wetland, even using the more stringent FICWD definition. In a recent revision of the S&T technical procedures document (NSST 2017), the default assumption for planted forest has been removed; however, the default assumption in the previous version may have affected much of the mapping being analyzed here.

Objective 1b: Impact of Spatial Uncertainty and Temporal Mismatch

Results from the simple and probable overlays were remarkably similar. This may be due to the very large and robust sample (over 16 000 observations) and prevalence of single-condition (“pure”) uncertainty buffers: 85% of plot buffers contained either all NWI NFW or all NWI FW. Thus, while consideration of spatial uncertainty remains important in overlay analyses, it did not substantially affect the results in this case. All further discussion herein will focus on simple overlay results.

Evaluation of temporal disagreement showed no evidence that disagreements were caused by wetland change during the interval between field inventory and aerial photo acquisition. Rates of misclassification did not rise with increased temporal differences. The overwhelming signal observed in the data was that because field observation classified more sites as wetland, when aerial photos were taken after field observation, net wetland conversion to NFW was implied. When field inventory was conducted after aerial photo acquisition, net wetland gains were implied.

Objective 1c: Characterizing Disagreements

For all forest condition variables, patterns of misclassification were significantly different than would be expected if misclassifications occurred at random, proportional to overall class membership. Misclassifications were significantly higher than expected in younger stands, in the flatwoods physiographic class (defined as “flat or fairly level sites outside flood plains... Excludes deep sands and wet, swampy sites”), in pine forest types, and in planted stands (Table 9). It is possible that these are all related to forest type, as a higher proportion of pine stands are in younger age classes than any other forest type, pine stands are the predominant forest type in flatwoods, and most planted stands are pine. Closed pine canopies obscure the ground from view year-round, making accurate identification of wetland conditions difficult. This difficulty, combined with the Dahl and Bergeson (2009) instructions for mappers to consider planted stands as upland unless direct visual evidence indicated otherwise, could explain higher than expected misclassification rates in these classes.

Objective 2: Delineation Uncertainty

We tested an approximate approach to epsilon band area estimation and found that it was within about 3% of the epsilon band area that would be obtained using spatial buffering. Using the best-case assumption that all wetland delineations were within the narrow tolerances described in the standards (5 m), the epsilon band model suggested that a 95% confidence interval on FW area is in the range of ± 7 to 15%.

Implications for Change Detection

Inference about change detection must consider the underlying uncertainty of estimates at the two points in time. An example of the way classification accuracy could be incorporated in change estimates would be to consider the probability of correct detection of a specific change given observed misclassification rates. If the classification disagreement observed in this study applies equally to two points in time, we can estimate the probability that wetland conversion has occurred

in areas mapped as such. This would be the product of the user's accuracy for FW times the user's accuracy for NFW (i.e., the joint probability of correctly mapping FW at time 1 and correctly mapping NFW at time 2). Assuming independent and equal misclassification rates at time 1 and time 2, we get $0.907 \times 0.680 = 0.626$. That is, a mapped indication of wetland conversion may be incorrect more than a third of the time.

Combining sources of uncertainty, we note (1) sampling errors with coefficients of variation around 20% (Dahl 2011), (2) change detection accuracies of about 63%, and (3) area estimates with confidence intervals of 7 to 15%. These levels of uncertainty provide little confidence to support inferences about annual FW conversion rates in the range of 0.13%.

Conclusions

Accurate mapping of FWs from aerial photography or other remote sensing systems requires that a photointerpreter or machine classification can detect the presence of (a) hydrophytic vegetation, (b) hydric soils, or (c) wetland hydrology. Successful identification requires the use of imagery with adequate resolution and acquisition at a time when phenomena such as wet soils or surface water are visible and may be impossible when dense forest canopies obscure the ground. For these reasons, it should not be surprising that field observations identified wetland conditions on 2.3 times the number of plots than did aerial photo interpretation, using comparable definitions for FW.

Delineation uncertainty, even using best-case assumptions about delineation error, was shown to lead to large uncertainty in wetland area estimates. Combined with classification accuracy that was below levels called for in standards, the uncertainty in aerial photo-based delineation of FWs leads to serious concerns about its fitness for inference about change in FW area.

Due to the availability of an extensive, if dated, reference data set, this study focused on the southeastern Atlantic seaboard states; results may not be uniformly applicable to other U.S. regions. It is also worth noting that our results from the use of FIA timberland plots apply only to mapping of FWs, not to NFWs such as ponds or marshes.

The use of a large sample of field observations proved valuable in assessing not only overall mapping accuracy, but in identifying factors that influenced classification performance. While FIA no longer conducts wetlands identification at field plots, the use of a point sample such as the FIA plot network facilitates statistical estimates of reliability (see Brown, Smith, and McCollum 2001) and can be conducted in an objective, comprehensive, and transparent design. Because the use of a point sample for area estimates avoids issues with boundary delineation uncertainty, it could prove to be a useful (and potentially less expensive) alternative to a polygon-based change analysis approach such as the current S&T mapping (Munoz *et al.* 2009).

This analysis confirms what has been previously reported: accurate mapping of FWs from remote sensing is extremely difficult (NRC 1995; Tiner 1997). When forest canopies are removed through harvesting, it is possible to observe wet soils or surface water on aerial photography, provided the photos are acquired during wet periods of the year. The absence of such visible conditions does not signify wetland loss, as noted in the revised technical procedures for S&T mapping (NSST 2017).

References

- Barrette, J., P. August and F. Golet. 2000. Accuracy assessment of wetland boundary delineation using aerial photography and digital orthophotography. *Photogrammetric Engineering and Remote Sensing* 66 (4):409–416.
- Bechtold, W. A. and P. L. Patterson, eds. 2005. The Enhanced Forest Inventory and Analysis Program—National Sampling Design and Estimation Procedures. General Technical Report SRS-80. Asheville, N.C.: U.S. Department of Agriculture Forest Service, Southern Research Station.
- Brown, M. J. 1997. Distribution and characterization of forested wetlands in the Carolinas and Virginia. *Southern Journal of Applied Forestry* 21 (2):64–70.
- Brown, M. J., G. M. Smith and J. McCollum. 2001. Wetland Forest Statistics for the South Atlantic States. Resource Bulletin SRS-62. Asheville, N.C.: U.S. Department of Agriculture, Forest Service, Southern Research Station.
- Congalton, R. G. 1991. A review of assessing the accuracy of classifications of remotely sensed data. *Remote Sensing of Environment* 37 (1):35–46.
- Congalton, R. G. and K. Green. 2008. *Assessing the Accuracy of Remotely Sensed Data: Principles and Practices*, 2d ed. CRC Press.
- Cowardin, L. M., V. Carter, F. C. Golet and E. T. LaRoe. 1979. Classification of Wetlands and Deepwater Habitats of the United States. FWS/OBS-79/31. Washington, D.C.: U.S. Fish and Wildlife Service.
- Dahl, T. E. 2000. *Status and Trends of Wetlands in the Conterminous United States 1986 to 1997*. Washington, D.C.: U.S. Department of the Interior, Fish and Wildlife Service.
- Dahl, T. E. 2006. *Status and Trends of Wetlands in the Conterminous United States 1998 to 2004*. Washington, D.C.: U.S. Department of the Interior, Fish and Wildlife Service.
- Dahl, T. E. 2011. *Status and Trends of Wetlands in the Conterminous United States 2004 to 2009*. Washington, D.C.: U.S. Department of the Interior, Fish and Wildlife Service.
- Dahl, T. E. and M. T. Bergeson. 2009. *Technical Procedures for Conducting Status and Trends of the Nation's Wetlands*. Washington, D.C.: U.S. Fish and Wildlife Service, Division of Habitat and Resources Conservation.
- Dai, X. and S. Khorram. 1998. The effects of image misregistration on the accuracy of remotely sensed change detection. *IEEE Transactions on Geoscience and Remote Sensing* 36 (5):1566–1577.
- Federal Geographic Data Committee (FGDC) Wetlands Subcommittee. 2009. Wetlands Mapping Standard. FGDC Document Number FGDC-STD-015-2009.
- Federal Interagency Committee for Wetland Delineation (FICWD). 1989. *Federal Manual for Identifying and Delineating Jurisdictional Wetlands*. Washington, D.C.: U.S. Army Corps of Engineers, U.S. Environmental Protection Agency, U.S. Department of Agriculture, Fish and Wildlife Service, Soil Conservation Service.
- Foy, A. S., L. W. Carstensen, S. P. Prisley, J. B. Campbell and R.L. Dymond. 2015. A review and evaluation of uncertainty classification and the error-band geometry model. *Transactions in GIS* 19 (4):604–618.
- Gage, E., D. J. Cooper and R. Lichvar. 2020. Comparison of USACE three-factor wetland delineations to national wetland inventory maps. *Wetlands*. <<https://doi.org/10.1007/s13157-019-01234-y>>
- Hughes, M. L., P. F. McDowell and W. A. Marcus. 2006. Accuracy assessment of georectified aerial photographs: Implications for measuring lateral channel movement in a GIS. *Geomorphology* 74:1–16.
- Jasumback, T. 1996. *GPS Evaluation: West Coast Test Site*. Missoula, Mont.: USDA Forest Service, Technology Development Center.
- Kudray, G. M. and M. R. Gale. 2000. Evaluation of National Wetland Inventory maps in a heavily forested region in the upper Great Lakes. *Wetlands* 20 (4):581–587.
- Loehle, C., B. T. Wigley, E. Schilling, V. Tatum, J. Beebe, E. Vance, P. Van Deusen and P. Weatherford. 2009. Achieving conservation goals in managed forests of the Southeastern Coastal plain. *Environmental Management* 44:1136–1148.
- McRoberts, R. E., D. G. Wendt, M. D. Nelson and M. H. Hansen. 2002. Using a land cover classification based on satellite imagery to improve the precision of forest inventory area estimates. *Remote Sensing of Environment* 81:36–44.
- Morrissey, L. A. and W. R. Sweeney. 2006. Assessment of the National Wetlands Inventory: Implications for wetland protection. In *Proceedings of the Geographic Information Systems and Water Resources IV—AWRA Spring Specialty Conference*, held in Houston, Tex.
- Munoz, B., V. M. Lesser, J. R. Dorney and R. Savage. 2009. A proposed methodology to determine accuracy of location and extent of geographically isolated wetlands. *Environmental Monitoring and Assessment* 150:53–64. doi: 10.1007/s10661-008-0672-0.
- National Research Council. 1995. *Wetlands: Characteristics and Boundaries*. Washington, D.C.: The National Academies Press. <<https://doi.org/10.17226/4766>>
- National Standards and Support Team (NSST). 2017. *Technical Procedures for Conducting Status and Trends of the Nation's Wetlands (Version 2)*. Washington, D.C.: U.S. Fish and Wildlife Service, Division of Budget and Technical Support.
- Nichols, C. 1994. Map Accuracy of National Wetlands Inventory Maps for Areas Subject to Land Use Regulation Commission Jurisdiction. Ecological Services report R5-94/6. Hadley, Mass.: U.S. Fish and Wildlife Service.
- Olofsson, P., G. M. Foody, M. Herold, S. V. Stehman, C. E. Woodcock and M. A. Wulder. 2014. Good practices for estimating area and assessing accuracy of land change. *Remote Sensing of Environment* 148:42–57.
- Pengra, B. W., S. V. Stehman, J. A. Horton, D. J. Dockter, T. A. Schroeder, Z. Yang, W. B. Cohen, S. P. Healey and T. R. Loveland. 2020. Quality control and assessment of interpreter consistency of annual landcover reference data in an operational national monitoring program. *Remote Sensing of Environment* 238:111261. <<https://doi.org/10.1016/j.rse.2019.111261>>
- Prisley, S. P. and C. L. Luebbing. 2011. Uncertainty exposed: A field lab exercise where GIS meets the real world. *Journal of Natural Resources and Life Sciences Education* 40:144–149.
- Richardson, C. J. 1994. Ecological functions and human values in wetlands: A framework for assessing forestry practices. *Wetlands* 14 (1):1–9.
- Shi, W. 2010. *Principles of Modeling Uncertainties in Spatial Data and Spatial Analyses*. Boca Raton, Fla.: CRC Press.
- Stolt, M. H. and J. C. Baker. 1995. Evaluation of National Wetland Inventory maps to inventory wetlands in the southern Blue Ridge of Virginia. *Wetlands* 15:346–353. <<https://doi.org/10.1007/BF03160889>>
- Story, M. and R. G. Congalton. 1986. Accuracy assessment: A user's perspective. *Photogrammetric Engineering and Remote Sensing* 52:397–399.
- Tiner, R. W. 1997. NWI maps: What they tell us. *National Wetlands Newsletter*: March–April.
- U.S. Fish and Wildlife Service (USFWS). 2004. *National Standards and Quality Components for Wetlands, Deepwater and Related Habitat Mapping*. Arlington, Va.: U.S. Fish and Wildlife Service, Division of Habitat and Resource Conservation, Branch of Habitat Assessment.
- U.S. Department of Agriculture (USDA). 2015. *Summary Report: 2012 National Resources Inventory*. Washington, D.C.: Natural Resources Conservation Service and Ames, Iowa: Center for Survey Statistics and Methodology, Iowa State University. <<http://www.nrcs.usda.gov/technical/nri/12summary>>
- Walbridge, M. R. 1993. Functions and values of forested wetlands in the southern United States. *Journal of Forestry* 91 (5):15–19.
- Wernette, P., A. Shortridge, D. P. Lusch and A. F. Arbogast. 2017. Accounting for positional uncertainty in historical shoreline change analysis without ground reference information. *International Journal of Remote Sensing* 38(13):3906–3922. doi: 10.1080/01431161.2017.1303218.

Call for Submissions

Special Issue on Urban Remote Sensing

Photogrammetric Engineering and Remote Sensing (PE&RS) is seeking submissions for a special issue on Urban Remote Sensing.

The formulation of the 17 Sustainable Development Goals (SDGs) is a major leap towards humankind's quest for sustainability. In recent decades, global urban areas have been rapidly expanding, especially in developing countries. The prospect is that the urbanization rate will reach 60% by 2030. Urban expansion will inevitably increase vulnerability to natural hazards, natural vegetation cover decline and arable land loss, urban heat islands, air pollution, hydrological cycle alteration and biotic homogenization. Since urban ecosystems are strongly influenced by anthropogenic activities, a considerable amount of research has been conducted all around the world to understand the spatial patterns, driving forces and the ecological and social consequences of urbanization. It is not only crucial for characterizing the ecological consequences of urbanization but also for developing effective economic, social and environmental policies in order to mitigate its adverse impacts.

Remote sensing has been widely used for investigating urban environment and the associated drivers during the urbanization process, as it can quickly and frequently monitor large area surface change with lower cost, compared to field survey or in situ measurements. Digital archives of remotely sensed data provide an excellent opportunity to study historical urban changes and to relate their spatio-temporal patterns to environmental and human factors. With the rapid development of Earth observation techniques, it has become convenient to obtain a large number of remotely-sensed imagery over a certain area at different times, from hundreds of Earth observation platforms. However, this brings challenges to researchers to timely process the remote sensing big data as well as to rapidly transfer the data into information and knowledge.

Considering this, this special issue of *PE&RS* is aimed at reporting novel studies on exploiting remote sensing big data to monitor and improve urban environment, and showing the potential of remote sensing in developing sustainable cities, including but not limited to:

- Urban remote sensing big data
- Remote sensing information interpretation
- Urban expansion, dynamics and associated environment consequences
- Remote sensing of urban water quality

- Remote sensing of urban thermal environment
- Remote sensing of urban geological environment
- Urban sustainability assessment
- Urban sustainable development
- Urban Spatiotemporal analysis
- Urban Sustainability Indicators
- Urban environmental Monitoring

Papers must be original contributions, not previously published or submitted to other journals. Submissions based on previous published or submitted conference papers may be considered provided they are considerably improved and extended. Papers must follow the instructions for authors at <http://asprs-pers.edmgr.com/>.

Important Dates

- July 1, 2020 Submission system opening
- October 31, 2020 Submission system closing
- Planned publication date: Dec. 2020
- Submit your manuscript to <http://asprs-pers.edmgr.com/> by Oct. 31, 2020.

Guest Editors

Zhenfeng Shao, *Wuhan University, China*

Prof. Zhenfeng Shao, Professor at the State Key Laboratory of Information Engineering in Surveying, Mapping and Remote Sensing, Wuhan University, China. His research interests include urban remote sensing. He is now an associate editor of Email: shaozhenfeng@whu.edu.cn.

Orhan Altan, *Istanbul Technical University, Turkey*

Prof. Orhan ALTAN, Professor at the Department of Geomatics Engineering, Istanbul Technical University, Turkey. He is Past President and Honorary Member of ISPRS, Honorary Member of Science Academy. He has published more than 200 scientific papers in scientific journals and conferences, and editor or co-editor of more than 20 international books. Email: oaltan@itu.edu.tr

J.L.van Genderen, *University of Twente, Netherlands*

Professor J.L.van Genderen, Prof. at the Department of Earth Observation Science, Faculty of Geo-information Science and Earth Observation(ITC),University of Twente, Netherlands, he is an associate Editor of Geo-Spatial Information Science. His research interests include photogrammetry and remote sensing, urban remote sensing and computer vision. Email: Genderen@alumni.itc.nl.

Weighted Spherical Sampling of Point Clouds for Forested Scenes

Alex Fafard, Ali Rouzbeh Kargar, and Jan van Aardt

Abstract

Terrestrial laser scanning systems are characterized by a sampling pattern which varies in point density across the hemisphere. Additionally, close objects are over-sampled relative to objects that are farther away. These two effects compound to potentially bias the three-dimensional statistics of measured scenes. Previous methods of sampling have resulted in a loss of structural coherence. In this article, a method of sampling is proposed to optimally sample points while preserving the structure of a scene. Points are sampled along a spherical coordinate system, with probabilities modulated by elevation angle and squared distance from the origin. The proposed approach is validated through visual comparison and stem-volume assessment in a challenging mangrove forest in Micronesia. Compared to several well-known sampling techniques, the proposed approach reduces sampling bias and shows strong performance in stem-reconstruction measurement. The proposed sampling method matched or exceeded the stem-volume measurement accuracy across a variety of tested decimation levels. On average it achieved 3.0% higher accuracy at estimating stem volume than the closest competitor. This approach shows promise for improving the evaluation of terrestrial laser-scanning data in complex scenes.

Introduction

Lidar (light detection and ranging) has become an established tool in the general field of remote sensing, given its ability to collect active three-dimensional spatial measurements of a scene (Lim and Suter 2009; Dassot, Constant and Fournier 2011). By emitting pulses of light and detecting rebounds with precise timing, and assuming a homogeneous scan medium, a measurement of distance is obtained. Depending on the task that is being conducted, a lidar unit is typically built with either a raster or a spherical scan path (Hopkinson *et al.* 2004). In the case of airborne platforms, the raster paradigm is usually implemented, since it affords the ability to follow a whisk-broom sensor path as the platform moves forward. Due to this motion, and given a sufficiently high temporal frequency, sampling is relatively uniform with the velocity vector (Lin, Benziger and Habib 2016). In the case of a spherical scan path, as in a semispherical ground-scanning (terrestrial) lidar unit, there is a nonuniform density of samples accrued over the surface of constant phase. This implies that at a fixed radius from the origin of capture, the density of the inscribed spherical surface will vary as a function of position. This can be readily visualized by imagining that at some elevation angle ϕ there are L_ϕ azimuthal steps which take the system through some angular ring $E \in \{0, 2\pi\}$ (Figure 1). Given that the angular spacings $\Delta\phi$ and $\Delta\theta$ between samples along the set of axes are held to be constants, the spatial density of points will be significantly greater as one approaches the elevation “poles” of the sphere of constant phase. In other words, the

distance between azimuthal rings decreases as the elevation angle approaches $b\pi$, where b is any integer. These azimuthal rings are illustrated as the black circular samples in Figure 2.

In practice, this effect is found to manifest as an over-sampling of points which are near either nadir or zenith to the sensor. This can introduce a bias in the structural assessment of lidar data and affect the accuracy of mapping and modeling

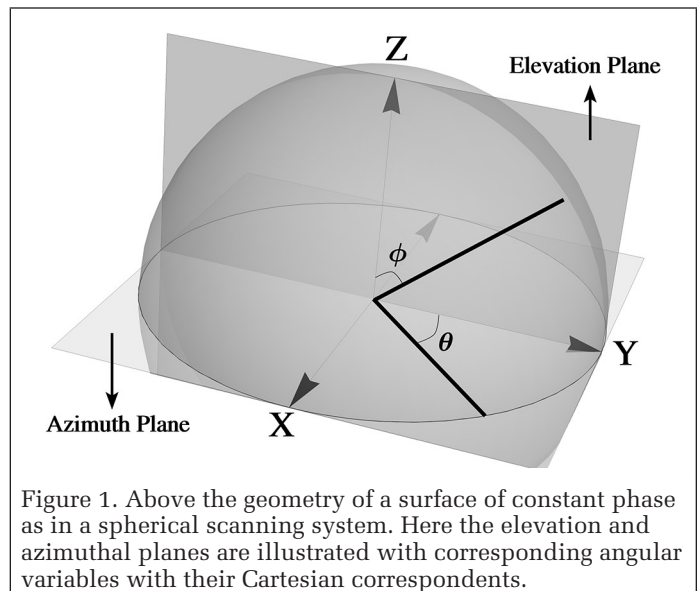


Figure 1. Above the geometry of a surface of constant phase as in a spherical scanning system. Here the elevation and azimuthal planes are illustrated with corresponding angular variables with their Cartesian correspondents.

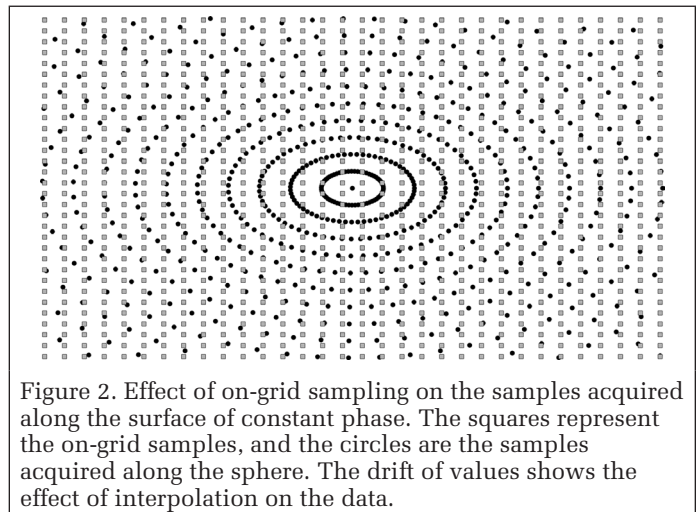


Figure 2. Effect of on-grid sampling on the samples acquired along the surface of constant phase. The squares represent the on-grid samples, and the circles are the samples acquired along the sphere. The drift of values shows the effect of interpolation on the data.

Alex Fafard, Ali Rouzbeh Kargar, and Jan van Aardt are with the Department of Imaging Science, Rochester Institute of Technology, Rochester, NY, 14623 (Ajf4163@rit.edu).

Photogrammetric Engineering & Remote Sensing
Vol. 86, No. 10, October 2020, pp. 619–625.
0099-1112/20/619–625

© 2020 American Society for Photogrammetry
and Remote Sensing
doi: 10.14358/PERS.86.10.619

these attributes. The complexity of the structures in the point cloud, especially in the areas closer to the scanner, can aggravate the impact of over-sampling (Sugimoto *et al.* 2017). The distribution of points illustrates the effect of over-sampling, which is present at the poles under a spherical sampling paradigm. This effect is undesirable, as it results in a statistical bias of points if left unaddressed. Additionally, this bias can impair the functionality of many three-dimensional algorithms for tasks like registration (Elseberg, Borrmann and Nüchter 2011; Aoki *et al.* 2019), feature detection (Elseberg *et al.* 2011; Lang, Manor and Avidan 2019), and surface reconstruction (Schaefer *et al.* 2019).

Previous Work

This effect has been addressed in past research efforts through various down-sampling or resampling schemes (Mandow *et al.* 2010; Orts-Escolano *et al.* 2013; Miknis *et al.* 2015; Sugimoto *et al.* 2017; Lang *et al.* 2019; Nezhadarya *et al.* 2019). One simple and standard solution, often used for the down-sampling of three-dimensional data, is based on a random sample of points (Knuth 1998). This technique has proven insufficient due to the nature of the problem posed. That is, a uniformly random sample of biased data is itself biased (Hopkinson *et al.* 2004; Yang *et al.* 2019). Traditional grid-based down-sampling relies on restricting Cartesian density to some predefined grid size. These techniques interpolate points to a grid. In principle, this solves the problem; however, interpolation-based resampling is nonideal, because it distorts data points (Sugimoto *et al.* 2017). This effect reduces the quality and fidelity of data to an often unacceptable degree. The effect of this grid sampling is shown in Figure 2.

Another technique which is able to mitigate this data drift to a degree uses voxel grids to calculate voxel-block centroids based on the point population within each voxel block. These techniques take the centroid of each populated voxel block to get a more accurate resample without distorting it to a fixed grid. These techniques have the advantage of being simple to implement and based on first principles. Unfortunately, they suffer from two shortcomings. The first is that voxel-based methods unequally resample variably dense surfaces and require an optimally selected voxel-block size to achieve good results (Laine and Karras 2010). Approaches based on k -d trees and octrees (k -d trees with each node possessing eight children) leverage the hyperplane separation in Cartesian space, implied by tree construction, to rapidly subset point clouds based on tree depth and population (Schnabel and Klein 2006). These constructs have the advantage of not needing to resample points in space and are able to operate in linear $O(n)$ time with a volume of n points (Shu and Kankanhalli 1994). Resampling to a quota and to a given node depth allows for effective point picking. This technique, while rapid, shares the weakness of the voxel-based approach, requiring a good selection of node depth for well-posed data extraction.

Poisson dart and disk sampling are two methods which are used to resample point clouds, often with good results. These methods rely on distribution samples which result in a balanced point selection. Generally, their results are good; however, the base implementations of these methods are computationally expensive (White, Cline and Egbert 2007).

Graph-based methods take a more dynamic approach to reducing the points in a point cloud. In the work of Chen *et al.* (2018), the graph-based approach constructs a representation of a point cloud as an actionable graph. It frames point-cloud resampling as an optimization problem, seeking to retain maximum local variation in the data. Redundant point-cloud information is removed in this way, leaving primarily the contours of the scene. The results exhibited from this technique are impressive, but the technique is more complicated and computationally expensive than others (Natali *et al.* 2011).

One consideration which is not often explicitly accounted for in any of these alternatives (Puttonen *et al.* 2013) is the weighting of more distal points relative to points near the scanner origin (Mandow *et al.* 2010). In a spherical scanning system, more distant points are sparse due to angular sampling and therefore richer in information content (Marsaglia 1972; Knuth 1998). It is desirable that these observations be weighted commensurate with their projected point size.

Additionally, it is desirable to avoid resampling by proxy of interpolation or a center-of-mass-based calculation, since this alters the data, especially in the presence of noise or extreme outliers (Sugimoto *et al.* 2017). Another consideration is that the algorithm should be rapid and simple to implement, such that resampling can occur in real time with modest computational resources.

Contribution of a Novel Solution

This article produces a geometric sampling correction for a quasi-spherical scanning system. This sampling takes into account the angular position along the surface as well as the distance of points from the origin centroid. This method is computationally simple and competitive with other techniques.

In the following sections, the representation of the scanning system is described and the proposed method is introduced. After that, the proposed method is validated with three methods of evaluation, including a case study and synthetic data. Finally, the results are discussed.

Methods

For a laser scanning system which samples on a sphere, we describe the representation of points and then the proposed method.

Terrestrial Laser-Scanner Point-Cloud Representation

Points in Cartesian and spherical space are represented, respectively, as $C[x,y,z]$ and $C[\theta,\phi,\rho]$, where

$$x = \rho \cos \theta \sin \phi, \quad (1)$$

$$y = \rho \sin \theta \sin \phi, \quad (2)$$

$$z = \rho \cos \theta, \quad (3)$$

and obviously

$$C[x,y,z] \triangleq C[\theta,\phi,\rho]. \quad (4)$$

Then the function which describes the discretely sampled surface of a spherical scan is given by

$$S(\theta,\phi,\rho) = \sum_{n_\theta=0}^{Q_\theta} \sum_{n_\phi=0}^{Q_\phi} \rho_{n_\theta, n_\phi} \cdot \delta(\theta - \psi_\theta \cdot n_\theta, \phi - \psi_\phi \cdot n_\phi), \quad (5)$$

where δ is the Dirac delta function, which is used to capture discrete samples along a constant surface, and ψ_{dim} describes the step size between samples n_θ and n_ϕ as

$$\psi_{\text{dim}} = \frac{E_{\text{dim}}}{Q_{\text{dim}}}. \quad (6)$$

In this case, E_{dim} is the angular span of the scan (2π in the case of a full rotation in a given dimension) and Q_{dim} is the number of steps allowed in that span.

In the case of a full scan with a constant phase or range (i.e., a sphere, where $\rho = c$), Equation 5 is reduced to

$$S(\theta,\phi,\rho = c) = c \sum_{n_\theta=0}^{Q_\theta} \sum_{n_\phi=0}^{Q_\phi} \delta\left(\theta - \frac{2\pi}{Q_\theta} \cdot n_\theta, \phi - \frac{2\pi}{Q_\phi} \cdot n_\phi\right). \quad (7)$$

This sampled surface of constant phase is a simulation of what is captured by a spherical scanner at a constant range. On this sphere, the normalized number of points per unit area is illustrated in Figure 3. It is immediately apparent that the

distribution of points along the spherical surface varies with the elevation angle of the scanner. This realization of the surface of constant phase inspires the following section, where the sphere is sampled according to this distribution.

Proposed Method

Weisstein (1999) notes that the distribution of points on such a surface varies only as a function of the elevation angle, as has been previously observed in Figure 3. Taking note of the definition of the projected area being a function of the elevation angle, the distribution of points on such a sampled hemisphere P is derived as

$$P_\phi = \frac{1}{2} \sin \phi. \quad (8)$$

This distribution describes the relative affinity for points to be sampled at the pole of the scan path. Inversely, it represents the relative weighting term along a hemisphere.

This distribution is symmetric, and therefore it can be extended to the full terrestrial laser-scanning (TLS) scan path by looking at the full sphere instead of a hemisphere:

$$\Omega \text{weight}(\phi) = \frac{1}{2} |\sin \phi|. \quad (9)$$

Framing the mitigation of sampling bias as a point-picking problem, we can leverage this information to provide probabilities for point excision. This symmetric distribution can then be subtracted from a uniform point distribution to produce a likelihood function for point removal as a function of elevation angle. In Figure 4, a likelihood function is shown for a sphere.

Thus a means of assigning probabilities for point selection is produced and can be used to bring the distribution of preserved points closer to a uniform distribution.

This is a useful conclusion for the angular correction of a spherically sampled scene. This likelihood function L allows for a weighted selection of points along the surface of a sphere. It should also be made to vary with the distance from the scanner origin, to provide greater weighting to more distant objects. The projected area of a point increases as the square of the radial distance ρ from the scanner as the beam diverges. In order to compensate for this, a radial weighting factor is added that increases the likelihood of preserving more distant points.

The likelihood function L can then be rewritten in terms of radial distance and elevation angle. A square factor for distance is used due to the distance-squared relationship of the subtended point area away from the scanner:

$$\begin{aligned} L(\phi, \rho) &= \rho^2 \left(1 - \Omega_{\text{weight}}(\phi) \right) \\ &= \rho^2 \left(1 - \frac{1}{2} |\sin \phi| \right). \end{aligned} \quad (10)$$

After normalizing this function into a probability distribution for input points, a weighted permutation can then be conducted. The k retained points then represent a close approximation of spherically uniform sampled points.

Results

The proposed technique is compared with three other standard techniques used for point-cloud sampling: voxel grid sampling, Poisson dart sampling, and random sampling (White *et al.* 2007; Laine and Karras 2010). These techniques are all used as standards in point-cloud processing. This evaluation is based on three criteria: a visual density assessment on a unit sphere, visual retention of salient structure in a complex forested scene, and stem-volume assessment with a known ground truth.

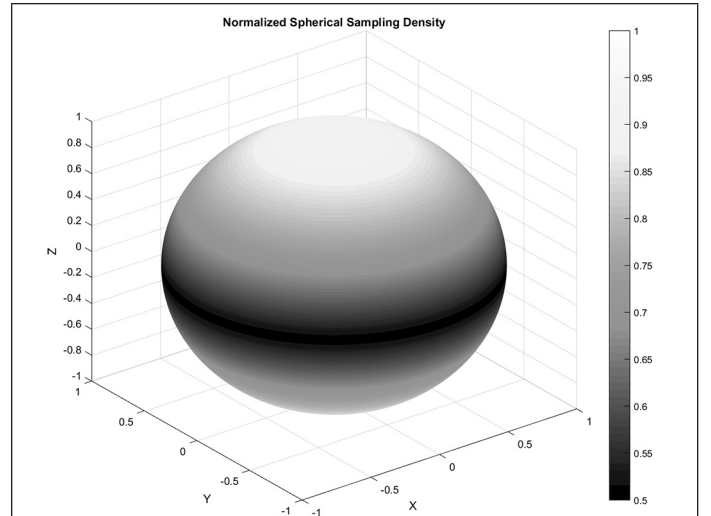


Figure 3. Normalized density plot of the surface of constant phase, generated by Equation 7. It can be observed that the poles of the surface represent high relative amounts of sampling compared to the rest of the sphere.

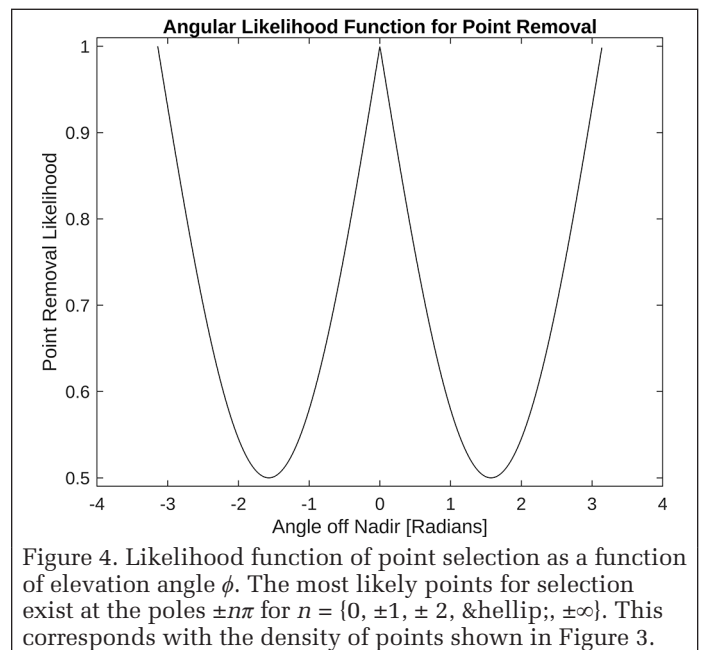


Figure 4. Likelihood function of point selection as a function of elevation angle ϕ . The most likely points for selection exist at the poles $\pm n\pi$ for $n = \{0, \pm 1, \pm 2, \dots, \pm\infty\}$. This corresponds with the density of points shown in Figure 3.

Case Study

Mangrove forests represent a complex form of forest environments, containing structures like aboveground root mass that can introduce challenges to automatic structural-assessment approaches. This complexity can accentuate the effect of over-sampling and affect the result of structural evaluation. Challenges from this complexity make mangrove forests an excellent candidate for validation of the proposed technique.

Terrestrial lidar data were collected using a low-cost, mobile, rapid-scan system (Compact Biomass LiDAR [CBL]; Kelbe *et al.* 2013; Kargar and van Aardt YYYYY). CBL uses a 905-nm laser pulsing at 27 kHz and provides coverage for a $270^\circ \times 360^\circ$ “hemisphere”; the 90° cone underneath the unit is unscanned. The measured range for CBL is 0.5 to 50 m, with a range accuracy of ± 30 mm. Its resolution is $0.250.25^\circ$, with a minimum angular step width of 4.36 mrad. A maximum of two returns are captured for each pulse. This system enables us to rapidly sample its surroundings, but at a lower angular resolution compared to higher-cost commercial scanners. As a result, one should allow for the challenges caused by lower

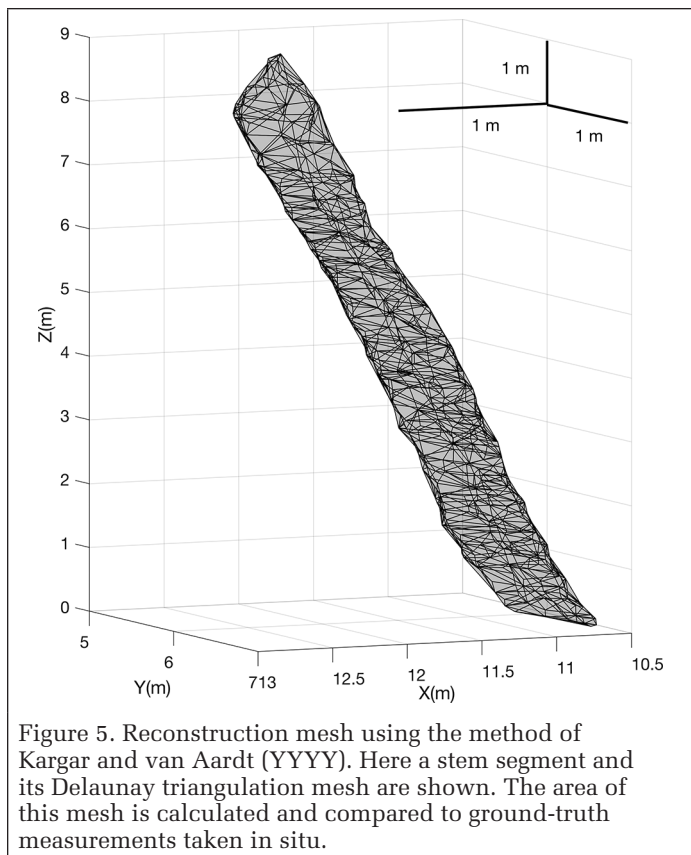


Figure 5. Reconstruction mesh using the method of Kargar and van Aardt (YYYY). Here a stem segment and its Delaunay triangulation mesh are shown. The area of this mesh is calculated and compared to ground-truth measurements taken in situ.

angular resolutions while developing algorithms for processing such data. It is also necessary to remove the bias resulting from over-sampling in the areas closer to the scanner to obtain a more consistent point density distribution throughout the point cloud. However, since the resolution of these data is arguably low, preserving the structural characteristics is of great importance. This concern led us to the idea that the proposed down-sampling scheme might ameliorate the structural-evaluation results.

Data were collected from mangrove forests located on the western Pacific island of Pohnpei, which is an eastern island state in the Federated States of Micronesia and in the Caroline Island chain (6°50'59.99" N, 158°12'60.00" E). In these mangrove forests, eight scans per plot were collected for 20 plots. These scans had a 45° angular separation, with the analysis performed on the point cloud resulting from registration of all eight scans. All trees which were measured that were greater than 5 cm in diameter at breast height (DBH) were identified in the volume assessment, and DBH was measured to the nearest 0.1 cm. For trees with prop roots, the point of measurement for determining DBH was 15 cm above the highest prop root that could safely be measured. Species-specific allometric equations developed for Pohnpei by Cole, Ewel, and Devoe (1999) were then used to convert live-tree DBH measurements into volume, after which the volume of each tree was summed for each plot and the total plot volume within each plot was divided by the area of that plot (m³/ha). In these data, individual trees had DBH ranging from 16.8 to 41.8 cm measured directly in the field. Using the appropriate allometric equations, the plot-level volume range varied between 91.71 and 1105.5 m³/ha.

As a case study, the effect of the presented down-sampling approach is assessed on mangrove-forest stem-volume evaluation using data collected by the CBL system.

Kargar and van Aardt (YYYY) have used a three-dimensional classification approach for detecting stems in mangrove forest. In that work, stems were detected using a three-dimensional point-cloud classifier whose training set was acquired

by filtering the lidar point cloud based on the angular orientation of the points. The detected stems were then simulated using alpha shapes for volume estimation. The average consistency was acquired by comparing the plot-level stem volume (m³/ha) between lidar and field data.

In our accuracy assessment, we summed the volumes of all the stems in a plot and divided it by the area of the plot, producing a measure in meters cubed per hectare, which is common in forestry (van Aardt, Wynne and Oderwald 2006). This measurement is compared to the same measurement from field data to directly measure accuracy as

$$\text{Accuracy} = (Fv - |Fv - Lv|) \cdot Fv^{-1}, \quad (11)$$

where Fv is the measured field volume and Lv is the lidar-measured volume.

The accuracy of the volume measurement using the proposed down-sampling method was 85% at 10% sampling. This is significantly better than the original point cloud, which achieved an accuracy of only 64%. This accuracy is the result of comparison between the plot-level lidar stem-volume measurements and field-measured volume data. This algorithm was evaluated for stem-volume assessment accuracy using the same data, comparing the results obtained from a variety of down-sampling techniques: voxel grid sampling (Laine and Karras 2010), Poisson dart sampling (White *et al.* 2007), and random sampling in addition to the proposed method. Each down-sampling method was used to excise some percentage of the points from the original point cloud before attempting to estimate stem volume. The methods were tested for 50%, 10%, 5%, and 1% point retention.

In Table 1, the results of the stem-volume assessment are summarized. At all sampling levels the proposed method was measured to have the highest accuracy of the tested techniques. At the lowest sampling levels (e.g., 1%), the results of all the methods are very similar. This is likely due to the point set being so sparse in regions that it is difficult to extract stem volume regardless of the sampling method. At the 5% sampling mark the results start to become more pronounced, with the proposed method showing a clear increase in stem-volume measurement accuracy. This trend continues through the 10% and 50% marks, with the peak accuracy occurring with the proposed method at 10% sampling. The decrease in accuracy between the 10% and 50% levels may be attributed to the reduction of redundant over-sampled regions during the stem reconstruction.

We performed a Mann-Whitney U test in order to statistically evaluate the significance of the difference between the sets of volume measurements at each sampling level. This test is nonparametric, implying that there is no assumption made on the form of the distribution of the data; and since our data are not normally distributed, this test is ideal for our study (Mann and Whitney 1947). The significance level used here was 0.05. When the U value found using the Mann-Whitney test between two sets of data is lower than the critical U value, it implies that the difference between the two sets of data is statistically significant. In Table 1, the observed U value and corresponding p value are summarized. These results show that the difference between the two sets of data—stem volume before and after down-sampling—is statistically significant for the random and grid-based approaches across all decimation levels. The proposed method also outperformed the voxel- and Poisson-based methods across all sampling levels, although it did not perform significantly better.

With the large differences in stem-reconstruction accuracy from the different down-sampling techniques, it is apparent that the presented down-sampling approach in this work can have a significant impact on the structural and statistical assessment of lidar point clouds. This effect is most structurally

Table 1. Stem-volume measurement accuracy for various sampling levels.

| Sampling Level (%) | Down-Sampling Method | Stem-Volume Measurement Accuracy (%) | Critical U Value | Obtained U Value | p |
|--------------------|----------------------|--------------------------------------|------------------|------------------|------|
| 100 | Original | 64 | 127 | 118 | 0.02 |
| | Proposed | 58 | — | — | — |
| | Random | 54 | 69 | 93 | 0.08 |
| 1 | Grid-based | 57 | 69 | 93 | 0.08 |
| | Voxel centroid | 58 | 69 | 93 | 0.08 |
| | Poisson dart | 58 | 69 | 93 | 0.08 |
| | Proposed | 84 | — | — | — |
| 5 | Random | 70 | 113 | 106 | 0.03 |
| | Grid-based | 79 | 113 | 119 | 0.08 |
| | Voxel centroid | 80 | 113 | 138 | 0.09 |
| | Poisson dart | 81 | 113 | 138 | 0.09 |
| 10 | Proposed | 85 | — | — | — |
| | Random | 69 | 127 | 118 | 0.02 |
| | Grid-based | 79 | 127 | 122 | 0.04 |
| | Voxel centroid | 80 | 127 | 178 | 0.09 |
| 50 | Poisson dart | 83 | 127 | 178 | 0.09 |
| | Proposed | 81 | — | — | — |
| | Random | 61 | 70 | 41 | 0.02 |
| | Grid-based | 69 | 70 | 41 | 0.02 |
| | Voxel centroid | 73 | 70 | 65 | 0.04 |
| | Poisson dart | 74 | 70 | 65 | 0.04 |

apparent at the 50% sampling mark in our study, though the method is effective down to small sampling sizes.

Artificial-Data Results

The proposed method was used on a simulated spherical object function with 80 000 points spread in a spherical sampling pattern. This pattern is generated directly from Equation 7, which describes the sampling pattern of a TLS. Experimentally, the sphere was sampled at $k = 2000$ using a random permutation and the proposed method. The results are shown graphically in Figure 6. Visually, the random permutation retains the biased point selection along the poles. This bias is markedly repaired by the proposed method, and there appears to be a relatively uniform distribution of points along the sphere.

Results of Visual Application

A scene from a mangrove forest is shown in Figure 7. In the top left subplot, the original point cloud is shown with 6 747 951 points. This scene represents a typical mangrove forest, with a high degree of complexity and structure. The ground and points from objects close to the scanner are greatly

over-sampled due to the effects already described. With this original scene, multiple candidate sampling techniques were used to down-sample the point cloud to 0.1% of its original size. This extreme level of down-sampling provides a good visualization of how structure is retained in point selection. In the random permutation, angular bias from the original point cloud is carried over, resulting in greatly over-sampled proximal objects and ground. The random permutation scarcely looks like the original point cloud, with a large loss of structure, especially for objects at greater range. Both the Poisson-dart and voxel-grid approaches do a good job of ameliorating angular over-sampling, with fewer over-sampled ground points, but much of the structure of the objects from the original point cloud is not particularly well preserved. With the proposed method, a much larger portion of stem structure is retained, even at more distant ranges from the scanner. At the same time, this method works well to remove angular sampling bias.

Discussion

The proposed method has been evaluated both quantitatively and qualitatively through a case study and visual results. Visually, it is demonstrated to reduce sampling bias along the poles of a synthetic sphere. This range-independent correction is the result of Equation 9. In Figure 6 it can be seen that the sampling bias near the poles of the z-axis is reduced with the proposed method. This quality can be observed again in the CBL collect in Figure 7.

The proposed technique shows the best overall preservation of structure among the down-samples. The Poisson dart also performs competitively, with good structure preservation from the point cloud. The random permutation demonstrates a large degree of bias, particularly to the proximal and ground points. The voxel-grid method preserves structure fairly well but resamples the point cloud to a grid, resulting in some loss of clarity. The proposed method preserves stem structure even at an extreme decimation level (0.1% retention). Compared to the tested methods, the combined use of the inverse range and spherical correction is very effective in preserving stem structure.

In more quantitative assessment, stem reconstruction and volume assessment have been used for a proxy of sampling performance by Kargar and van Aardt (YYYY). The decrease in accuracy was higher in the plots with more structural complexity and density in terms of lidar points.

This is attributed to the fact that our down-sampling algorithm maintains the structure of the point cloud. This is achieved by providing a more uniform density distribution with respect to elevation angle and prioritizing more distant points. As a result, the impact of structural complexity—e.g., aboveground roots in this case—in the areas closer to the

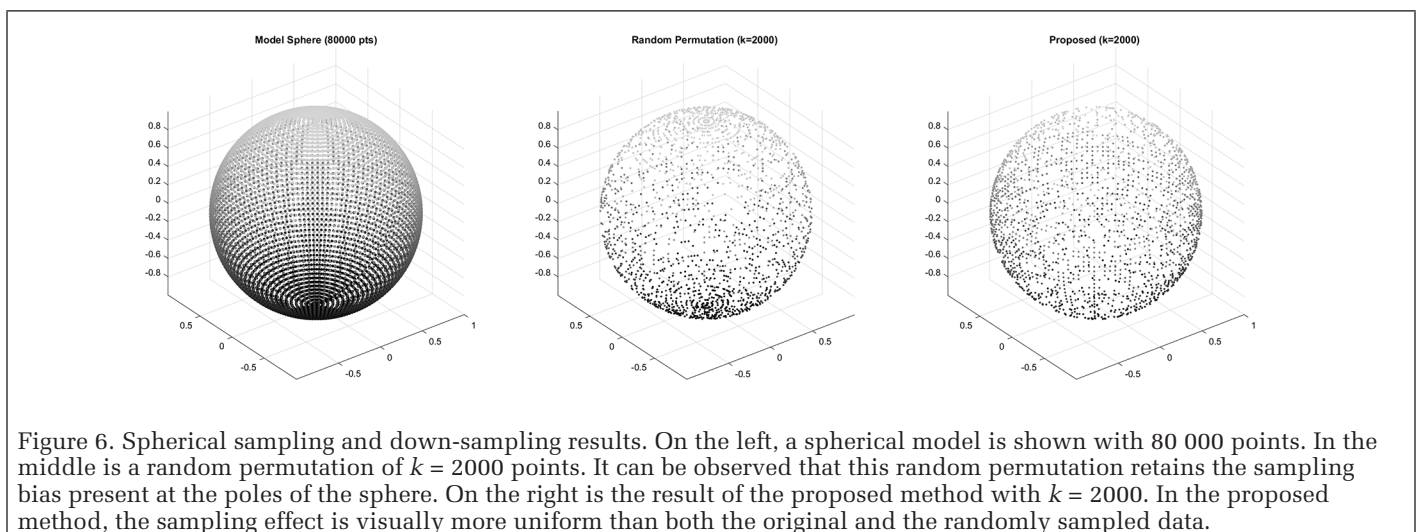


Figure 6. Spherical sampling and down-sampling results. On the left, a spherical model is shown with 80 000 points. In the middle is a random permutation of $k = 2000$ points. It can be observed that this random permutation retains the sampling bias present at the poles of the sphere. On the right is the result of the proposed method with $k = 2000$. In the proposed method, the sampling effect is visually more uniform than both the original and the randomly sampled data.

scanner that are highly over-sampled is reduced. At 50% this effect is observed most prominently, with the disparity in structural sampling reflected in the accuracy of the techniques. At 10% the volume assessment is actually more accurate after sampling for all methods, but the proposed method still performs the best. This is reflected at lower sampling levels as well, but the difference between methods is diminished as the sampling becomes extremely sparse ($\approx 1\%$).

Though this method has only been validated in mangrove-forest environments, we feel that it may hold promise for a wider variety of use cases. We hypothesize that in more sparse environments with great distance in range, the benefits of the proposed method will be even more pronounced. This proposed sampling method is based on first principles and should demonstrate similar performance on any TLS sampled evenly in spherical coordinates. In the future, it would be beneficial to understand the performance of this method as applied to other environments and use cases. For example, urban point clouds exhibit different spatial properties than those of many forested environments. The use of this method in such conditions will be a future area of research. In particular, it is of interest to examine the functional impact of sampling on three-dimensional tasks such as point-set registration (Aoki *et al.* 2019) in complex and noisy environments.

Conclusions

Spherical lidar scanners present a sampling problem when scanned in a conventional mode, where the poles of the sampling sphere are over-sampled relative to other hemispherical scan positions. Conventional methods of down-sampling (e.g., randomly selecting points) have failed to address this bias. A method of down-sampling by permutation, which uses weights derived from the geometry of the sampling, has been

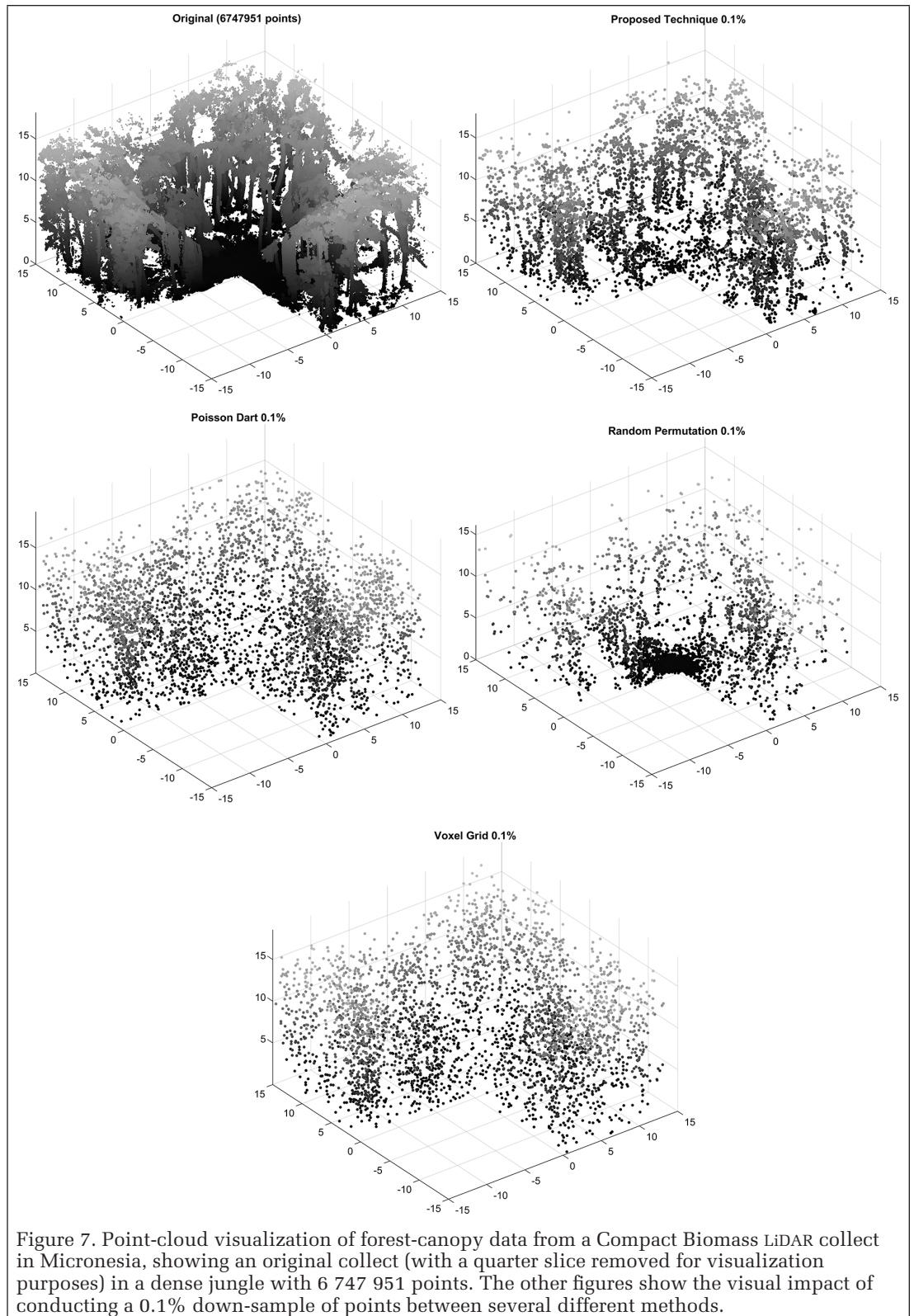


Figure 7. Point-cloud visualization of forest-canopy data from a Compact Biomass LiDAR collect in Micronesia, showing an original collect (with a quarter slice removed for visualization purposes) in a dense jungle with 6 747 951 points. The other figures show the visual impact of conducting a 0.1% down-sample of points between several different methods.

presented here and found to be effective in the reduction of this scanning bias. Specifically, this technique appears to be highly effective at preserving structure during sampling. This is observed under even extreme reduction scenarios (as low as 0.1%) in samples. We validated our hypothesis by applying this approach to forestry TLS data as a case study (stem-volume assessment in a complex mangrove forest). Stem-volume accuracy was compared between the proposed technique and several conventional down-sampling techniques at the same

decimation level. Our down-sampling approach resulted in statistically more accurate volume measurement of stems, averaging a 3.0% increase in accuracy compared to the next best method. In addition to quantitative measures, the proposed method results in visually more uniform point clouds along both spherical and natural sets of points. This method may be effective for preprocessing TLS point clouds to down-sample and remove spherical bias. Future work should involve more extensive case studies of how this technique could affect structural assessment and statistical conclusions derived from terrestrial scanning systems in other environments.

References

- Aoki, Y., H. Goforth, R. A. Srivatsan and S. Lucey. 2019. PointNetLK: Robust & efficient point cloud registration using PointNet. Pages 7163–7172 in *2019 IEEE/CVF Conference on Computer Vision and Pattern Recognition (CVPR)*, held in Long Beach, Calif., 16–20 June 2019. Edited by J. Editor. Los Alamitos, Calif.: IEEE.
- Chen, S., D. Tian, C. Feng, A. Vetro and J. Kova evi . 2018. Fast resampling of three-dimensional point clouds via graphs. *IEEE Transactions on Signal Processing* 66 (3):666–681. <https://doi.org/10.1109/TSP.2017.2771730>.
- Cole, T. G., K. C. Ewel and N. N. Devoe. 1999. Structure of mangrove trees and forests in Micronesia. *Forest Ecology and Management* 117 (1–3):95–109. [https://doi.org/10.1016/S0378-1127\(98\)00474-5](https://doi.org/10.1016/S0378-1127(98)00474-5).
- Dassot, M., T. Constant and M. Fournier. 2011. The use of terrestrial LiDAR technology in forest science: Application fields, benefits and challenges. *Annals of Forest Science* 68 (5):959–974. <https://doi.org/10.1007/s13595-011-0102-2>.
- Elseberg, J., D. Borrmann and A. Nüchter. 2011. Efficient processing of large 3D point clouds. Paper 49 in *2011 XXIII International Symposium on Information, Communication and Automation Technologies*, held in Sarajevo, Bosnia and Herzegovina, 27–29 October 2011. Edited by A. Salihbegovi , J. Velagi , H. Šupi and A. Sadžak. Los Alamitos, Calif.: IEEE. <https://doi.org/10.1109/ICAT.2011.6102102>.
- Hopkinson, C., L. Chasmer, C. Young-Pow and P. Treitz. 2004. Assessing forest metrics with a ground-based scanning lidar. *Canadian Journal of Forest Research* 34 (3):573–583. <https://doi.org/10.1139/x03-225>.
- Kargar, A. R. and J. van Aardt. YYYY. Stem and root assessment in mangrove forests using a low-cost, rapid-scan terrestrial laser scanner. Unpublished manuscript.
- Kelbe, D., P. Romanczyk, J. van Aardt and K. Cawse-Nicholson. 2013. Reconstruction of 3D tree stem models from low-cost terrestrial laser scanner data. *Proceedings of SPIE* 8731:873106. <https://doi.org/10.1117/12.2015963>.
- Knuth, D. E. 1998. *The Art of Computer Programming, Vol. 2: Seminumerical Algorithms*, 3rd ed. Boston: Addison-Wesley.
- Laine, S. and T. Karras. 2010. Efficient sparse voxel octrees. Pages 55–63 in *Proceedings of I3D 2010: The 2010 ACM SIGGRAPH Symposium on Interactive 3D Graphics and Games*, held in Washington, DC, 19–21 February 2010. Edited by J. Editor. New York: ACM. <https://doi.org/10.1145/1730804.1730814>.
- Lang, I., A. Manor and S. Avidan. 2019. SampleNet: Differentiable point cloud sampling. arXiv 1912.03663.
- Lim, E. H. and D. Suter. 2009. 3D terrestrial LIDAR classifications with super-voxels and multi-scale Conditional Random Fields. *Computer-Aided Design* 41 (10):701–710. <https://doi.org/10.1016/j.cad.2009.02.010>.
- Lin, Y.-J., R. R. Benziger and A. Habib. 2016. Planar-based adaptive down-sampling of point clouds. *Photogrammetric Engineering and Remote Sensing* 82 (12):955–966. <https://doi.org/10.14358/PERS.82.12.955>.
- Mandow, A., J. L. Martínez, A. J. Reina and J. Morales. 2010. Fast range-independent spherical subsampling of 3D laser scanner points and data reduction performance evaluation for scene registration. *Pattern Recognition Letters* 31 (11):1239–1250. <https://doi.org/10.1016/j.patrec.2010.03.008>.
- Mann, H. B. and D. R. Whitney. 1947. On a test of whether one of two random variables is stochastically larger than the other. *The Annals of Mathematical Statistics* 18 (1):50–60. <https://doi.org/10.1214/aoms/1177730491>.
- Marsaglia, G. 1972. Choosing a point from the surface of a sphere. *The Annals of Mathematical Statistics* 43 (2):645–646. <https://doi.org/10.1214/aoms/1177692644>.
- Miknis, M., R. Davies, P. Plassmann and A. Ware. 2015. Near real-time point cloud processing using the PCL. Pages 153–156 in *2015 22nd International Conference on Systems, Signals and Image Processing*, held in London, UK, 10–12 September 2015. Edited by P. Liatsis, A. Uus and S. Miah. Los Alamitos, Calif.: IEEE. <https://doi.org/10.1109/IWSSIP.2015.7314200>.
- Natali, M., S. Biasotti, G. Patanè and B. Falcidieno. 2011. Graph-based representations of point clouds. *Graphical Models* 73 (5):151–164. <https://doi.org/10.1016/j.gmod.2011.03.002>.
- Nezhadarya, E., E. Taghavi, R. Razani, B. Liu and J. Luo. 2019. Adaptive hierarchical down-sampling for point cloud classification. arXiv 1904.08506.
- Orts-Escolano, S., V. Morell, J. García-Rodríguez and M. Cazorla. 2013. Point cloud data filtering and downsampling using growing neural gas. Pages PP–PP in *The 2013 International Joint Conference on Neural Networks (IJCNN)*, held in Dallas, Texas, 4–9 August 2013. Edited by J. Editor. Los Alamitos, Calif.: IEEE. <https://doi.org/10.1109/IJCNN.2013.6706719>.
- Puttonen, E., M. Lehtomäki, H. Kaartinen, L. Zhu, A. Kukko and A. Jaakkola. 2013. Improved sampling for terrestrial and mobile laser scanner point cloud data. *Remote Sensing* 5 (4):1754–1773. <https://doi.org/10.3390/rs5041754>.
- Schaefer, A., J. Vertens, D. Büscher and W. Burgard. 2019. A maximum likelihood approach to extract finite planes from 3-D laser scans. Pages PP–PP in *2019 International Conference on Robotics and Automation (ICRA)*, held in Montreal, 20–24 May 2019. Edited by J. Editor. Los Alamitos, Calif.: IEEE. <https://doi.org/10.1109/ICRA.2019.8794318>.
- Schnabel, R. and R. Klein. 2006. Octree-based point-cloud compression. Pages 111–120 in *Point-Based Graphics 2006: Eurographics/IEEE VGTC Symposium Proceedings*, held in Boston, 29–30 July 2006. Edited by M. Botsch and B. Chen. Aire-la-Ville, Switzerland: Eurographics Association. <https://doi.org/10.2312/SPBG/SPBG06/111-120>.
- Shu, R. and M. S. Kankanhalli. 1994. Efficient linear octree generation from voxels. *Image and Vision Computing* 12 (5):297–303. [https://doi.org/10.1016/0262-8856\(94\)90035-3](https://doi.org/10.1016/0262-8856(94)90035-3).
- Sugimoto, K., R. A. Cohen, D. Tian and A. Vetro. 2017. Trends in efficient representation of 3D point clouds. Pages 364–369 in *Ninth Asia-Pacific Signal and Information Processing Association Annual Summit and Conference (APSIPA ASC 2017)*, held in Kuala Lumpur, Malaysia, 12–15 December 2017. Edited by J. Editor. Los Alamitos, Calif.: IEEE. <https://doi.org/10.1109/APSIPA.2017.8282059>.
- van Aardt, J. A. N., R. H. Wynne and R. G. Oderwald. 2006. Forest volume and biomass estimation using small-footprint lidar-distributional parameters on a per-segment basis. *Forest Science* 52 (6):636–649.
- Weisstein, E. W. 1999. Sphere Point Picking. <<http://mathworld.wolfram.com/SpherePointPicking.html>> Accessed DD Month YYYY.
- White, K. B., D. Cline and P. K. Egbert. 2007. Poisson disk point sets by hierarchical dart throwing. Pages 129–132 in *IEEE/EG Symposium on Interactive Ray Tracing 2007*, held in Ulm, Germany, 10–12 September 2007. Edited by A. Keller and P. Christensen. Los Alamitos, Calif.: IEEE.
- Yang, G., X. Huang, Z. Hao, M.-Y. Liu, S. Belongie and B. Hariharan. 2019. PointFlow: 3D point cloud generation with continuous normalizing flows. arXiv 1906.12320.

WHO'S WHO IN ASPRS

BOARD OF DIRECTORS

BOARD OFFICERS

President

Jeff Lovin
Woolpert

President-Elect

Jason M. Stoker, Ph.D.
U.S. Geological Survey

Vice President

Christopher Parrish, Ph.D.
Oregon State University

Past President

Thomas Jordan, Ph.D.
University of Georgia

Treasurer

Stewart Walker, Ph.D.

Secretary

Lorraine B. Amenda, PLS, CP

BOARD MEMBERS

Sustaining Members Council – 2021

Chair: Joe Cantz
www.asprs.org/About-Us/Sustaining-Members-Council.html

Committee Chairs Council – 2022

Chair: Mike Zoltek
Vice-Chair: TBA

Early-Career Professionals Council – 2021

Chair: Bobby Arlen
Vice Chair: Melissa Martin

Region Officers Council – 2021

Chair: Lorraine B. Amenda, PLS, CP
Vice Chair: Demetrio Zourarakas

Student Advisory Council – 2021

Chair: Youssef Kaddoura
<http://www.asprs.org/Students/Student-Advisory-Council.html>

Technical Division Directors Council – 2021

Chair: Bandana Kar, Ph.D.
Vice Chair: Denise G. Theunissen

TECHNICAL DIVISION OFFICERS

Geographic Information Systems Division – 2021

Director: Xan Fredericks
Assistant Director: Denise G. Theunissen
www.asprs.org/Divisions/GIS-Division.html

Lidar Division – 2022

Director: Joshua Nimetz, CMS
Assistant Director: Ajit Sampath
www.asprs.org/Divisions/Lidar-Division.html

Photogrammetric Applications Division – 2022

Director: Kurt Rogers
Assistant Director: Benjamin Wilkinson
www.asprs.org/Divisions/Photogrammetric-Applications-Division.html

Primary Data Acquisition Division – 2021

Director: Jon Christopherson
Assistant Director: J. Chris Ogier
www.asprs.org/Divisions/Primary-Data-Aquisition-Division.html

Professional Practice Division – 2022

Director: Harold W. Rempel, III, CP
Assistant Director: Bill Swope
www.asprs.org/Divisions/Professional-Practice-Division.html

Remote Sensing Applications Division – 2022

Director: Raechel A. Portelli, Ph.D.
Assistant Director: Amr Abd-Elrahman
www.asprs.org/Divisions/Remote-Sensing-Applications-Division.html

Unmanned Autonomous Systems (UAS) – 2022

Director: Megan Ritelli, Ph.D.
Assistant Director: Dan Hubert

REGION PRESIDENTS

Alaska Region

David Parret
<http://www.asprsalaska.org/>

Cascadia Region

Robert Hairston-Porter

Eastern Great Lakes Region

Shawana P. Johnson, Ph.D, GISP
<http://egl.asprs.org/>

Florida Region

Xan Fredericks
<http://florida.asprs.org/>

Heartland Region

Whit Lynn
<http://heartland.asprs.org/>

Mid-South Region

<https://www.asprs.org/all-regions/mid-south.html>

Northeast Region

(representing the merger of The New England and Central New York Regions)
Trevis Gliotti, Interim President

North Atlantic Region

Richard W. Carlson, Jr., P.L.S., C.P.
<http://natlantic.asprs.org/>

Pacific Southwest Region

Omar G. Mora
<https://pswasprs.org/>

Potomac Region

Dave Lasko
<http://www.asprspotomac.org/>

Rocky Mountain Region

<http://www.asprs-rmr.org/>

Western Great Lakes Region

Brandon Krumwiede
<http://wgl.asprs.org/>

Redefining the Directional-Hemispherical Reflectance and Transmittance of Needle-Shaped Leaves to Address Issues in Their Existing Measurement Methods

Jun Wang, Jing M. Chen, Lian Feng, Jianhui Xu, and Feifei Zhang

Abstract

The directional-hemispherical reflectance and transmittance of needle-shaped leaves are redefined in this study. We suggest that the reflected and transmitted radiation of a leaf should be distinguished by the illuminated and shaded leaf surfaces rather than the usual separation of the two hemispheres by a plane perpendicular to the incoming radiation. Through theoretical analysis, we found that needle directional-hemispherical reflectance and transmittance measured by two existing techniques, namely Daughtry's method and Harron's method, could be significantly biased. This finding was proved by ray-tracing simulations intuitively as well as by inversions of the PROSPECT model indirectly. We propose the following requirements for needle spectral measurement in an integrating sphere: needles should be fully exposed to the light source, the interfusion of reflected and transmitted radiation on convex needle surfaces should be avoided, and multiple scattering of radiation among needles should be minimized.

Introduction

Needle-leaved plants represent a significant fraction of natural terrestrial ecosystems. For example, the boreal forest, the second-largest needle-leaf-dominated forest biome in the world (Astrup *et al.* 2018), covers ~50% of the North American boreal zone (Brandt *et al.* 2013) and nearly one-third of the Earth's forest area (MacDicken *et al.* 2015). Thus, monitoring the temporal and spatial variation of needle-leaved plants is in the interest of studies of global change. The advent of spectroscopy and remote sensing has made such monitoring more efficient, convenient, and intuitive. The accuracy of relevant results, as well as the validity of corresponding conclusions, heavily depends on the fidelity of collected leaf

Jun Wang and Lian Feng are with the School of Environmental Science and Technology, Southern University of Science and Technology, Shenzhen, China (fengl@sustech.edu.cn).

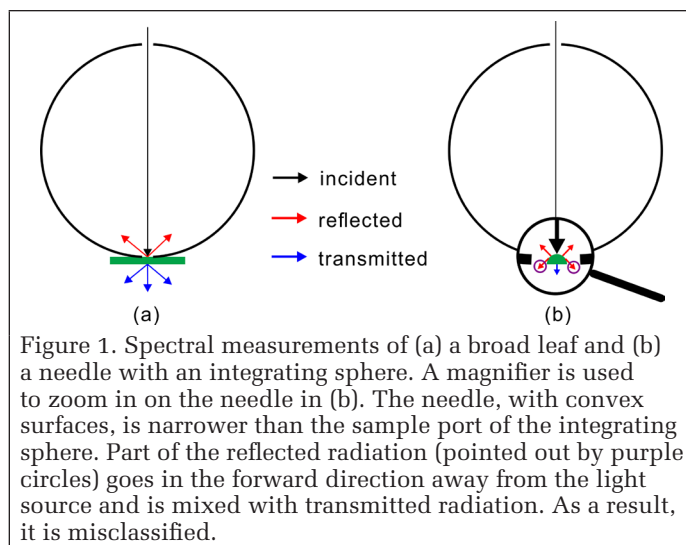
Jing M. Chen is with the International Institute for Earth System Science, Nanjing University, Nanjing, China (jing.chen@utoronto.ca).

Jianhui Xu is with the Key Laboratory of Guangdong for Utilization of Remote Sensing and Geographical Information System, Guangdong Open Laboratory of Geospatial Information Technology and Application, Guangzhou Institute of Geography, Guangzhou, China; and the Southern Marine Science and Engineering Guangdong Laboratory, Guangzhou, China.

Feifei Zhang is with the Department of Computer Science, Guangdong University of Education, Guangzhou, China.

spectra, which are the basic data required for retrieving leaf biochemical and biophysical traits.

An integrating sphere is a device commonly used in the remote-sensing community for leaf spectral measurements, due to its solid theoretical basis (Jacquez and Kuppenheim 1955; Miller and Sant 1958). It is a highly reflective cavity in appearance, with several holes or ports reserved for attaching samples, holding a light source or a white reference. When connected with a spectrometer, signals within the sphere can be captured so as to produce a reflectance, transmittance, or absorption curve. In most circumstances, the sample port of an integrating sphere can be completely covered by broad leaves, whose reflected and transmitted radiation can be clearly separated in this way (Figure 1a). However, needle-shaped leaves have distinct morphological characteristics. They are always too narrow to completely cover the sample port of an integrating sphere. Existing techniques, namely Daughtry's method and Harron's method, measure the directional-hemispherical reflectance (DHR) and transmittance (DHT) of needle-shaped leaves by putting an array of needle samples into a sample holder, which has to be no smaller than the sample port to be attached (the sample holder is also called a *carrier* in other studies). As already mentioned, an integrating sphere only



Photogrammetric Engineering & Remote Sensing
Vol. 86, No. 10, October 2020, pp. 627–641.
0099-1112/20/627–641

© 2020 American Society for Photogrammetry
and Remote Sensing
doi: 10.14358/PERS.86.10.627

captures signals within the sphere; therefore, the two faces of the sample holder serve as the *de facto* reference plane for needles to distinguish reflected and transmitted radiation. The validity of such methods needs to be examined, as some radiation can be hard to define. For example, the radiation indicated by purple circles in Figure 1b is reflected at the needle surface but goes in the forward direction away from the light source and is not captured by the integrating sphere. As a result, it will be regarded as transmitted radiation. This phenomenon pushed us to review the definitions of DHR and DHT for needle-shaped leaves. However, we failed to find a clear definition in the existing literature. In order to solve the problem, it is necessary to define the DHR and DHT for needle-shaped leaves.

The DHR and DHT of a unit surface already have clear definitions (Schaeppman-Strub *et al.* 2006). However, leaves are more than just flat surfaces, as they can also be thick objects. When a ray hits a surface without thickness, it will be either reflected from the surface or refracted after penetrating through the surface, following physical laws described by Fresnel or Snell's equations; but when a leaf has a certain thickness, the ray penetrating through the leaf surface will undergo an additional radiative transfer process by interacting with the interior of the leaf. In this case, the reflectance from the surface contains two parts: the surface reflection and the internal scattering (Jacquemoud and Ustin 2008). In most circumstances, a lamina bifacial leaf has upper (facing incoming radiation) and lower (shaded) surfaces on which reflectance and transmittance can be defined. In these circumstances, the definitions of DHR and DHT for a unit surface can be applied directly to flat leaves such as broad leaves. But needle-shaped leaves are quite special and different in their morphological characteristics. With comparable width and thickness, needles could have many sides or circular or semicircular cross-sectional shapes, which do not have clear upper and lower surfaces. This raises an important issue for spectral measurements of needle reflectance and transmittance: how

to distinguish reflected and transmitted radiation for needle-shaped leaves? This issue can be addressed faithfully by extending the DHR and DHT from unit surfaces to needles.

The goal of this article is to investigate the methods to separate reflected and transmitted radiation from needle-shaped leaves, based on which the DHR and DHT of needle-shaped leaves can be defined. The potential drawbacks of two existing techniques for measurements of needle DHR and DHT are also analyzed to demonstrate the importance of this separation. The specific objectives of this article are to demonstrate that the reflected and transmitted radiation of a leaf should be distinguished by the illuminated and shaded leaf surfaces, and to investigate the requirements for measuring needle reflectance and transmittance.

Theory

Defining the DHR and DHT for Needle-Shaped Leaves

In this section, a needle with a semicircular cylindrical shape is shown as an example (Table 1). The definition given in the present study can also be applied to needles of other shapes. The needle has two degrees of freedom to describe its angular position, according to Chen and Black (1992): the longitudinal axis of the cylinder and the normal to the surface of some reference plane associated with the leaf. Only the cross-sectional views of the needle are displayed. All directions in three-dimensional space are projected into the cross-sectional plane.

Identifying the Reflected and Transmitted Radiation of a Needle by the Illuminated and Shaded Leaf Surfaces

The DHR of a unit surface is defined as the ratio of the radiant flux for light reflected by a unit surface area into the view hemisphere to the illumination radiant flux (Figure 2a; Schaeppman-Strub *et al.* 2006). When the definition applies to a broad surface, no matter flat or rough, the total reflected radiant flux integrated over the whole illuminated face should be

Table 1. Simulating Daughtry's, Harron's and Defined reflectance and transmittance for two different needle shapes when light strike on two different sides of the needles.

| Needle shape | Semicircular Needle | | Regular Triangular Needle | |
|--------------|---------------------|-----------|---------------------------|-----------|
| | Convex Side | Flat Side | Convex Side | Flat Side |
| Daughtry's | | | | |
| Harron's | | | | |
| Defined | | | | |

--> Incident radiation - - -> Reflected radiation - - -> Transmitted radiation

used instead (Figure 2b). Therefore, it can be inferred that the reflected and transmitted radiation of a broad surface should be distinguished by the illuminated and shaded faces. Similarly, the surface of a thick object such as a leaf (including but not limited to needles) can always be split into an illuminated part and a shaded part when exposed to collimated light, and the reflected and transmitted radiation can be separated by these two types of leaf surfaces (Figure 2c). All reflections happening at the leaf surface illuminated by the direct light (Figure 2c), regardless of their directions, contribute to the reflectance. The total reflectance also includes internally scattered radiation escaping from the illuminated side of the needle. The radiation escaping from the leaf interior via the shaded side of the needle is included in transmittance. It should be noted that the method proposed here to separate reflected and transmitted radiation is a generalized method which is also applicable to broad leaves. The shaded surface of a broad leaf includes the edges, which are always neglected in spectral measurements since little radiation comes out from this part of the leaf surface if the illuminated leaf surface is large enough (for example, as large as the sample port of an integrating sphere).

The Needle Being Measured Must Be Fully Illuminated

Although the reflectance and transmittance of a broad leaf may vary from one position to another due to the primary and secondary veins or due to surface roughness, they have been assumed to be quasi-identical across the whole leaf face, and the averaged values at several different points absent the primary veins are practically used in remote-sensing studies (e.g., Qiu *et al.* 2018). Therefore, broad leaves do not need to be fully illuminated in spectral measurements. In contrast, needle-shaped leaves are usually thick and narrow, and their leaf sides form a closed surface, not necessarily parallel or quasi-parallel. The reflectance and transmittance of a needle may change significantly when the needle is illuminated by collimated light in different directions (Figures 3 and 11). Thus a needle being measured must be fully illuminated (Figure 3b)—i.e., when the projected area of the needle (PAN) on a plane perpendicular to the incident direction is equal to the projected area of the needle's illuminated surface (PAI).

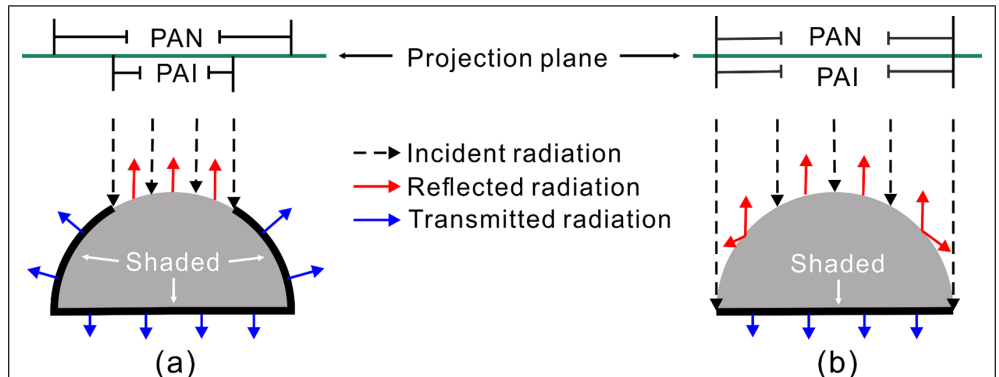
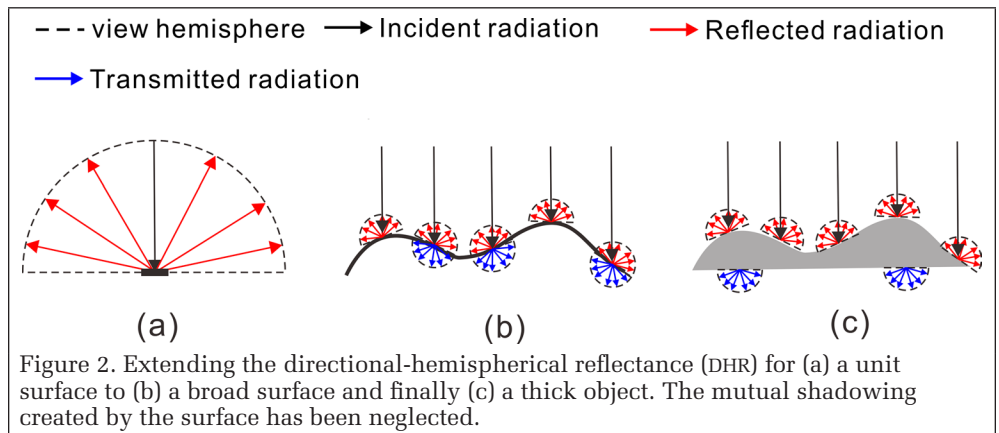


Figure 3. Illustrations of (a) partial and (b) full illumination of a needle. The needle surface is illuminated by collimated light in the same direction. The shaded leaf surfaces are highlighted by the thick black lines. PAN is the projected area of the needle on a plane perpendicular to the incident direction (green lines). PAI is the projected area of the needle's illuminated surface on a plane perpendicular to the incident direction. When PAN equals PAI, the needle is fully illuminated.

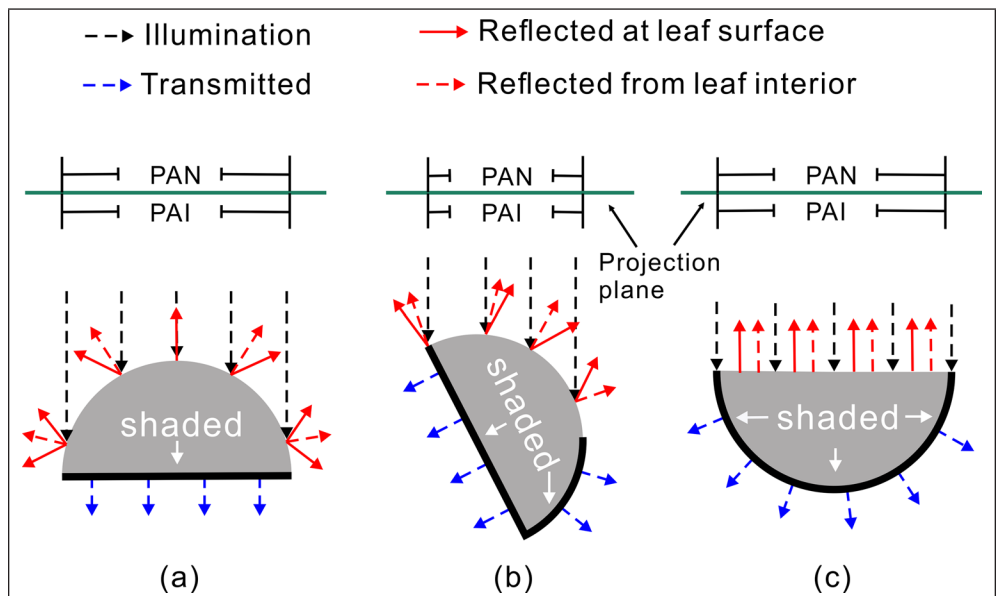


Figure 4. Directional-hemispherical reflectance and transmittance of a needle when it is fully illuminated by collimated light from different directions. The needle has a semicircular cross section (gray areas). PAN is the projected area of the needle on a plane perpendicular to the incident direction (green solid lines). The reflected and transmitted radiations are identified by the illuminated and shaded leaf surfaces. Note that in (a) and (b) the reflected radiation travels downward, crossing the horizontal plane. The shaded leaf surfaces are highlighted by thick black lines. All reflections happening at the leaf surface illuminated by direct light, regardless of their direction, contribute to the reflectance (red solid arrows). The total reflectance also includes internally scattered radiation escaping from the illuminated side of the needle (red dotted arrows). The radiation escaping from the leaf interior through the shaded side of the needle is included in the transmittance (blue dotted arrows).

Combined with the two points already mentioned, the DHR (DHT) of a needle is defined as the ratio of the total radiant flux reflected at or escaping from the illuminated surface (the internally scattered radiant flux escaping from the shaded surface) to the illumination radiant flux, when the needle is fully exposed to collimated light (Figure 4). The DHR and DHT of a needle may change with the illumination direction (Figures 4 and 11), and this change could be very large, since the needle morphology determines the distribution of incident angles—which is important for both the specular reflection at the needle surface and the diffuse scattering within the leaf tissues (McClen-don 1984; Grant, Daughtry and Vanderbilt 1993). Therefore, the uncertainties caused by the illumination direction should be minimized, and it is strongly recommended to measure the DHR and DHT when the PAN is maximum and the illuminated leaf surface area is minimum (i.e., Figure 4c), which ensures a maximum probability of incidences happening at near-normal angles so that more light can enter into the needle. However, in some scenarios, such as simulating canopy reflectance by a geometrical-optical model, where needles are illuminated by light from various directions, it is better to average the DHR and DHT over different illumination angles.

Potential Drawbacks of Existing Techniques for Needle DHR and DHT Measurements

According to the review by Yáñez-Rausell *et al.* (2014), there are three main approaches to measuring DHR or DHT of needle-shaped leaves: Hosgood's (Hosgood *et al.* 1995), Harron's (Harron 2002), and Daughtry's method (Daughtry, Biehl and Ranson 1989). The first approach measures the infinite reflectance of a needle stack contained in a glass cuvette by putting the cuvette against the sample port of an integrating sphere, and therefore it is not a focus of this article. The other two approaches use a sample holder instead of a glass cuvette to expose a mat of needles to the sample port, and in this way the averaged DHR and DHT of a single needle can be measured. This section will make a brief introduction to the two existing methods for DHR and DHT measurement and analyze their strengths and limitations. There are other integrating-sphere-based methods to measure the reflectance and transmittance of needlelike leaves, such as double-integrating-sphere systems (Pickering *et al.* 1992; Pickering *et al.* 1993; Potková *et al.* 2016; Möttus, Hovi and Rautiainen 2017). The sample holders used in these methods are similar to that used in Daughtry's method; therefore, we regard them the same as Daughtry's method.

Daughtry's Method

The method proposed by Daughtry *et al.* (1989) measures the DHR and DHT by placing a mat of needles on tape (Figure 5) against the sample port of an integrating sphere.

The key process of this method is to determine the gap fraction (GF) between needles, which was originally addressed by a painting technique with two-series measurements. However, the painting of each needle sample is labor-intensive and time-consuming, and therefore several studies (e.g., Middleton *et al.* 1996; Mesarch *et al.* 1999; Malenovský *et al.* 2006; Lukeš *et al.* 2013; Marín *et al.* 2016; Hovi, Raitio and Rautiainen 2017;

Abdullah *et al.* 2018) have used an image-capture technique instead to make a more direct and faster determination of the GF. Noda *et al.* (2013) even tried to skip the annoying GF-determination step by attaching a white paper to the back of the sample holder. A recent application of Daughtry's method is to measuring chlorophyll fluorescence spectral properties of needle-shaped leaves (Rajewicz *et al.* 2019).

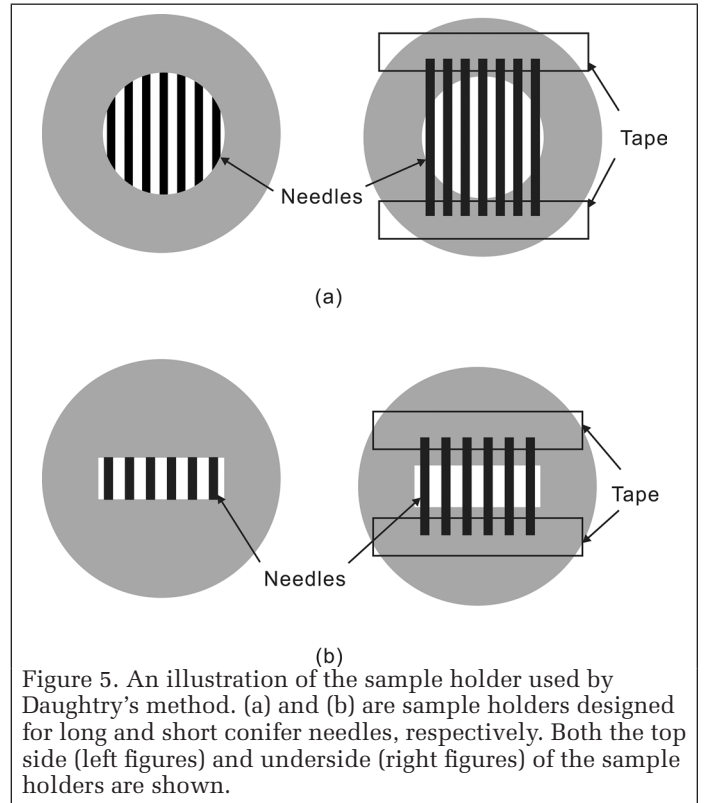


Figure 5. An illustration of the sample holder used by Daughtry's method. (a) and (b) are sample holders designed for long and short conifer needles, respectively. Both the top side (left figures) and underside (right figures) of the sample holders are shown.

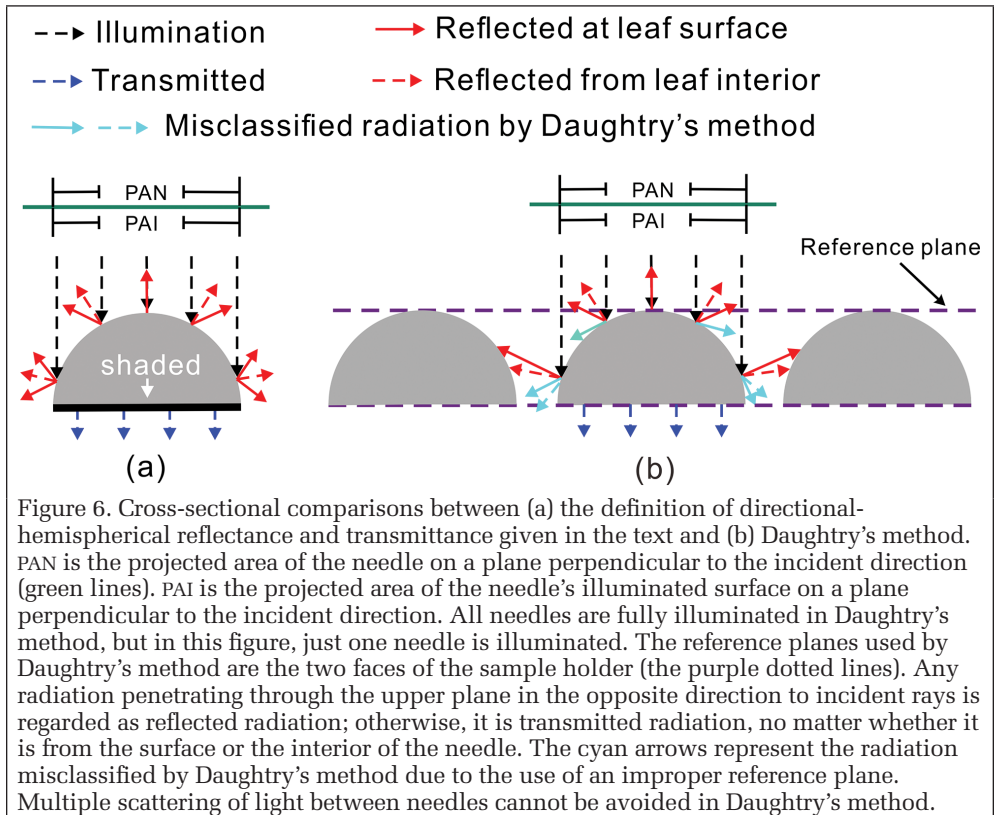


Figure 6. Cross-sectional comparisons between (a) the definition of directional-hemispherical reflectance and transmittance given in the text and (b) Daughtry's method. PAN is the projected area of the needle on a plane perpendicular to the incident direction (green lines). PAI is the projected area of the needle's illuminated surface on a plane perpendicular to the incident direction. All needles are fully illuminated in Daughtry's method, but in this figure, just one needle is illuminated. The reference planes used by Daughtry's method are the two faces of the sample holder (the purple dotted lines). Any radiation penetrating through the upper plane in the opposite direction to incident rays is regarded as reflected radiation; otherwise, it is transmitted radiation, no matter whether it is from the surface or the interior of the needle. The cyan arrows represent the radiation misclassified by Daughtry's method due to the use of an improper reference plane. Multiple scattering of light between needles cannot be avoided in Daughtry's method.

The major drawback of Daughtry's method is that the two faces of the sample holder, rather than the illuminated and shaded surfaces of needles, are the *de facto* reference to distinguish the reflected and transmitted radiation (Figure 6). The radiation scattered at needle edges may penetrate through the sample holder and be counted as transmitted radiation by mistake (Figure 6b). Moreover, multiple scattering between needles is not considered when calculating the final DHR and DHT (shown in Figure 6b). According to Mesarch *et al.* (1999), if interactions between needles are ignored, the optical properties measured by Daughtry's method will be more accurate in samples of smaller GF. However, smaller GF means stronger radiative interactions between needles, which cannot be neglected for accurate spectral measurements. Theoretically, Daughtry's method is able to measure the absorption of needles accurately as long as multiple scattering between needles is neglected, since all reflected and transmitted radiation can be captured—even though they may be misclassified due to the improper reference planes for separating reflected and transmitted radiation (i.e., the faces of sample holder). However, Olascoaga *et al.* (2016) compared the needle absorption measured directly by their revised internal method (needle reflectance and transmittance cannot be measured by this method) with the absorption measured by Daughtry's method under different GFs and found significant differences between these two products. Multiple scattering between needles is likely to be responsible for the inconsistency between the experimental results and our theoretical analysis.

Harron's Method

The reference used by Harron's (2002) method to distinguish reflected and transmitted radiation is one of the faces of the sample holder as well. The main difference between Daughtry's method and Harron's lies in the design of the sample holder. Harron specially molds a pair of black anodized-aluminum carriers with independent slots, each of which holds a needle (Figure 7). In this way, multiple scattering between needles can be eliminated effectively. However, different needle species need different types of carriers, since the slots must fit well to the needles.

Moreover, when wrapped in slots, needles cannot be fully exposed to light (as the examples shown in Figure 4), so part of the internally scattered radiation will be absorbed by slot walls, prohibiting a full consideration of the optical properties (Figure 8).

Materials and Methods

Simulating Daughtry's, Harron's, and Defined Reflectance and Transmittance by Ray Tracing

A two-dimensional ray-tracing technique was used to simulate DHR and DHT of needle-shaped leaves. Ray tracing can be implemented by sending massive rays and tracing the reflection, transmission, scattering, and absorption of each ray at leaf surfaces or within the leaf interior. Summing over the reflected and transmitted fluxes of all rays and dividing by the total incident flux produces the final reflectance and transmittance.

There are three sets of DHR and DHT to compare in this study: those simulated based on Daughtry's and

Harron's protocols and the definitions given in the present study. Hereafter, they are called Daughtry's, Harron's, and reference and transmittance. With the help of ray tracing, differences among these three sets of reflectance and transmittance were investigated for two needle shapes (triangular and semicircular) when collimated light was incident on different needle sides (flat or convex; Table 1). In order to simplify the radiative transfer of rays, the leaf interior was assumed to be homogeneous. Possible mutual masking created by leaf roughness (Bousquet *et al.* 2005), the hot spot (Comar *et al.* 2012), and scattering happening inside needles were neglected. All the needles were supposed to have rough surfaces, which was implemented in codes by giving needle surfaces a random tilt angle to ensure an incident angle in $[0^\circ, 40^\circ]$ for rays traveling from air to needle (Bousquet *et al.* 2005) and one in $[0^\circ, 90^\circ]$ for rays traveling from needle to air. The refraction and

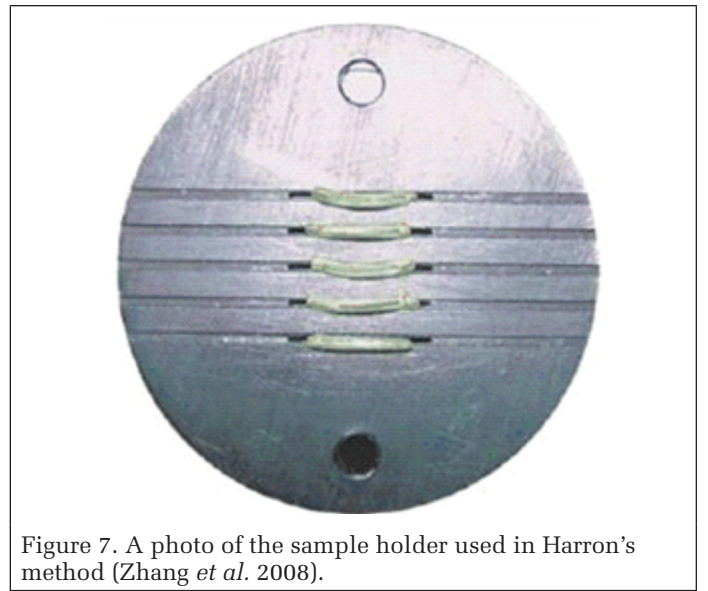


Figure 7. A photo of the sample holder used in Harron's method (Zhang *et al.* 2008).

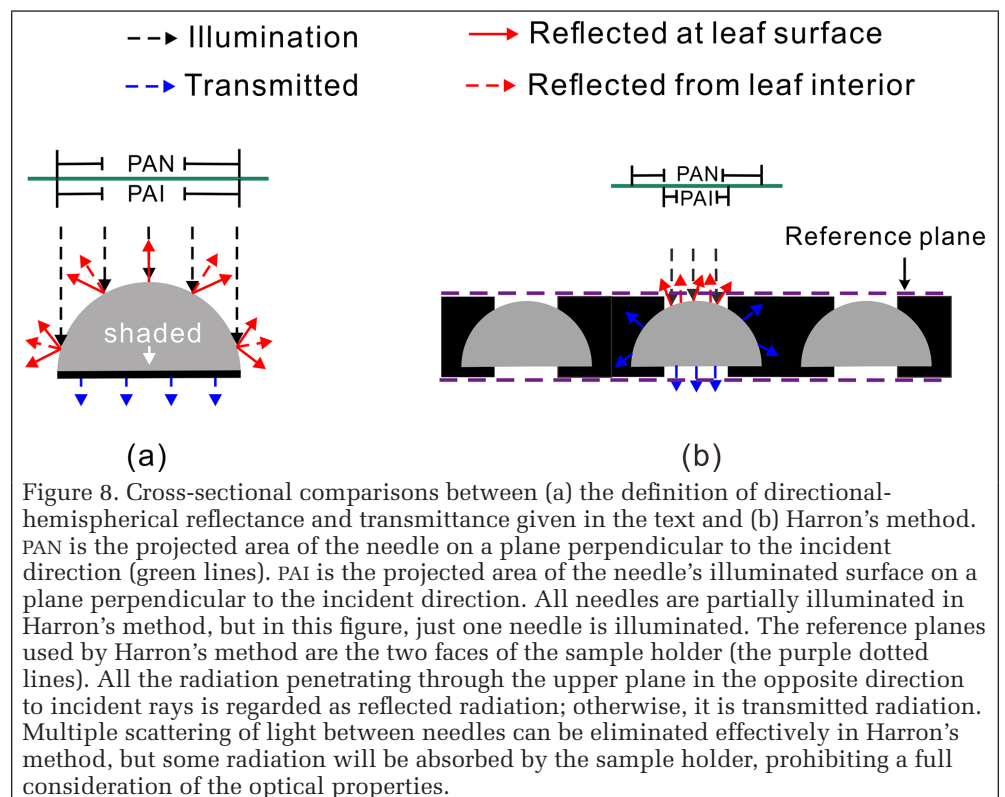


Figure 8. Cross-sectional comparisons between (a) the definition of directional-hemispherical reflectance and transmittance given in the text and (b) Harron's method. PAN is the projected area of the needle on a plane perpendicular to the incident direction (green lines). PAI is the projected area of the needle's illuminated surface on a plane perpendicular to the incident direction. All needles are partially illuminated in Harron's method, but in this figure, just one needle is illuminated. The reference planes used by Harron's method are the two faces of the sample holder (the purple dotted lines). All the radiation penetrating through the upper plane in the opposite direction to incident rays is regarded as reflected radiation; otherwise, it is transmitted radiation. Multiple scattering of light between needles can be eliminated effectively in Harron's method, but some radiation will be absorbed by the sample holder, prohibiting a full consideration of the optical properties.

reflection happening at needle surfaces were quantified by Fresnel equations and Snell's law, while the absorption by leaf tissues was calculated by the Beer–Lambert law. Four biochemical constituents were included. They are chlorophyll, carotenoid, water, and dry matter. Absorption coefficients of these four constituents as well as leaf surface refractive indices were taken from PROSPECT-5 (Feret *et al.* 2008).

The needles used in ray tracing are simplexes, not microscopic anatomical images of real needles, for three reasons: The anatomical structures of real leaves are too complex; it requires too much computation to trace the optical properties of needles by microscopic images, because multiple complicated processes are involved, such as vectorization; and no matter what the object being measured is, the differences between Daughtry's method, Harron's method, and our definition can always be investigated as long as the object is same for all methods. We have maintained primary physical and chemical traits of real needles (leaf surface roughness, needle shape, and biochemical constituents) as much as we can, but even so, the ray-tracing technique is not guaranteed to produce real and accurate needle reflectance and transmittance.

The ray number and tracing repetitions need to be optimized to avoid excessive tracing as well as to save computational costs. Less noise was observed with more rays (Figure 9a), but the spectra basically overlapped after being smoothed with a 10-nm moving-window averaging scheme (Figure 9b). Thus, 1500 rays were sent in this study. The radiant flux of a ray decreased when the ray was traced more times, and can be neglected after 10 tracings (Figure 9c). Therefore, the tracing repetitions were set to be 10 for all rays.

In this study, the reference reflectance and transmittance were treated as the benchmark based on which the absolute error (AE) and relative error (RE) of Daughtry's and Harron's reflectance, transmittance, and absorption were calculated, according to the equations

$$AE(\lambda) = S^*(\lambda) - S(\lambda) \quad (1)$$

$$RE(\lambda) = [S^*(\lambda) - S(\lambda)] / S(\lambda), \quad (2)$$

where $S^*(\lambda)$ represents Daughtry's or Harron's reflectance, transmittance, or absorption at wavelength λ and $S(\lambda)$ denotes the corresponding reference reflectance, transmittance, or absorption.

Demonstrating the Incompleteness of Harron's Reflectance and Transmittance Indirectly by Model Inversions

One of the main conclusions drawn in this study is that DHR and DHT measured by Harron's method can be incomplete, which will result in prominent overestimation of needle absorption. This conclusion can be proved by inversions of an optical-properties model. Existing optical-properties models are built on the same basic premise: the sum of reflectance R , transmittance T , and absorption A equals 1—that is,

$$R + T + A = 1. \quad (3)$$

If leaf absorption is overestimated, it will result in overestimation of leaf biochemical contents. So if significant positive biases are observed for estimated biochemical constituents, the absorption is overestimated, in support of our conclusion.

In this study, the PROSPECT-5 model (Jacquemoud and Baret 1990; Féret *et al.* 2008) was chosen. There are other optical-properties models, such as LIBERTY (Dawson, Curran and Plummer 1998), LEAFMOD (Ganapol *et al.* 1998), and SLOP (Maier, Lüdeker and Günther 1999). We chose PROSPECT-5 because it has been widely used in the remote-sensing community. The LIBERTY model, which was developed for needle-shaped leaves, was not used in this study because several potential flaws in its physical architecture have been found (Wang and Ju 2017).

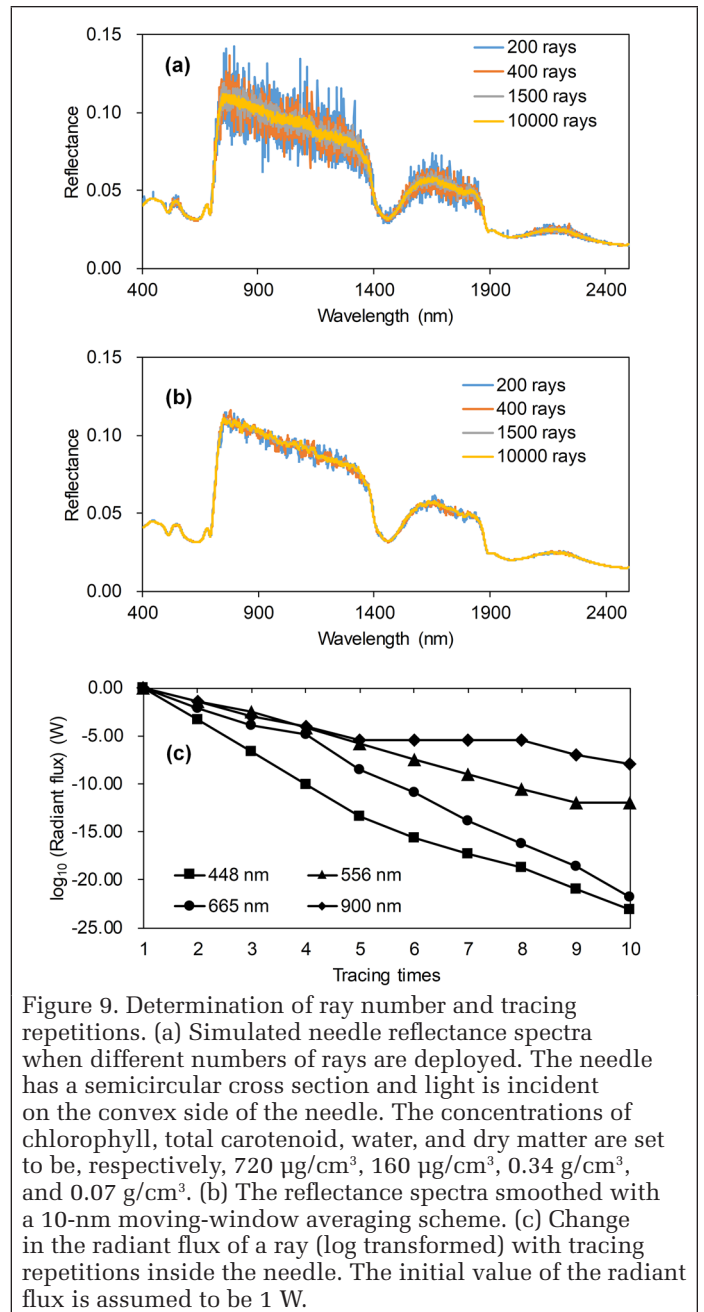


Figure 9. Determination of ray number and tracing repetitions. (a) Simulated needle reflectance spectra when different numbers of rays are deployed. The needle has a semicircular cross section and light is incident on the convex side of the needle. The concentrations of chlorophyll, total carotenoid, water, and dry matter are set to be, respectively, 720 $\mu\text{g}/\text{cm}^3$, 160 $\mu\text{g}/\text{cm}^3$, 0.34 g/cm^3 , and 0.07 g/cm^3 . (b) The reflectance spectra smoothed with a 10-nm moving-window averaging scheme. (c) Change in the radiant flux of a ray (log transformed) with tracing repetitions inside the needle. The initial value of the radiant flux is assumed to be 1 W.

We did not recalibrate parameters of PROSPECT-5 for needles as Malenovsky *et al.* (2006) did, because such calibrations are not necessary if the measured spectra are likely to be inaccurate, which we have already theoretically explained.

Model inversion, in essence, is to find the optimal combination of the input parameters to minimize the difference between simulated and measured optical spectra. This can be achieved by minimizing the merit function

$$K(N, C_1, \dots, C_n) = \sum_{\lambda} [(R_{\text{mod}}(\lambda) - R_{\text{mes}}(\lambda))^2 + (T_{\text{mod}}(\lambda) - T_{\text{mes}}(\lambda))^2] \quad (4)$$

where N is the structural parameter in PROSPECT-5; C_1, \dots, C_n are biochemical constituents to be estimated; $R_{\text{mes}}(\lambda)$ and $T_{\text{mes}}(\lambda)$ are the measured reflectance and transmittance at the wavelength λ (nm); and $R_{\text{mod}}(\lambda)$ and $T_{\text{mod}}(\lambda)$ are the modeled reflectance and transmittance. The optimization is performed using a constrained Powell line search for finding the minimum of the merit function. The parameterization of the method can be found in Table 3.

Since only chlorophyll and carotenoid are available in this study, to explore the influences of the measured partial reflectance and transmittance on model inversions we first run the PROSPECT-5 model in backward mode, with the spectral range restricted to 400–690 nm and the absorption assumed to be determined only by chlorophyll and carotenoid (Scheme 1). The spectral range was selected according to the absorption coefficient spectra available in this model. To allay concerns about the influences of other biochemical constituents on the inversion results, another scheme (Scheme 2) was also carried out. In this scheme, PROSPECT-5 was run in backward mode to estimate chlorophyll, carotenoid, equivalent water thickness, and leaf mass per area simultaneously using the spectral information of 400–900 nm. Wavelengths longer than 900 nm were removed due to low signal-to-noise ratio. Finally, the coefficient of determination (R^2) and relative mean standard error (RMSE) were calculated for both chlorophyll and carotenoid.

Data

Study Sites and Needle Sampling

Four field experiments were carried out in June, July, and August of 2003 and August of 2004 near Sudbury, Ontario, Canada (46°49'13" N to 47°12'9" N, 81°22'2" N to 81°54'30" N), where 10 large black spruce (*Picea mariana* (Mill.)) stands were selected as study sites. In each site, five trees were marked for sampling. Usually, one shoot is taken from each tree for subsequent spectral measurements and chemical analysis. But some trees had obvious young or old needles, and therefore additional shoots were sampled for these trees. In August of 2004, a medium-sized tree from one mature site was selected to analyze the influences of needle age and branch orientation on the variation of needle optical, biophysical, and biochemical parameters. Four shoots were sampled from this tree from four orientations—i.e., north, south, east, and west branches. Needles of different age classes (1998–2004) were taken from each shoot for biochemical measurements. There were 91 samples in total, but four were discarded due to loss of the spectra file. In the end, only 87 samples were available in this study.

Measurements of Needle Optical Properties

Harron's method was adopted to measure the reflectance and transmittance of black-spruce needles. The equipment used in this method include a FieldSpec Pro FR spectroradiometer (Analytical Spectral Devices, Inc., Boulder, Colo.) and a LI-COR 1800-12S integrating sphere (LI-COR, Inc., Lincoln, Neb.). They were connected with each other via an optical fiber. The spectroradiometer captures signals from the integrating sphere and produces spectra ranging from 350 to 2500 nm at 1-nm intervals. There are five ports in the integrating sphere. The measurements include the reference signal (RSS), the transmittance signal (TSP), the reflectance internal standard (RTS), the reflectance ambient (RSA), and the dark measurement (DRK). The detailed configurations of the integrating sphere for these five parameters are

listed in Table 2 and illustrated in Figure 10. The DHR and DHT of leaves were calculated as

$$\text{DHR}(\lambda) = \left(\frac{\text{RSS} - \text{RSA}}{\text{RTS} - \text{RSA}} \right) \cdot R_r(\lambda) \quad (5)$$

$$\text{DHT}(\lambda) = \left(\frac{\text{TSP} - \text{DRK}}{\text{RTS} - \text{RSA}} \right) \cdot R_r(\lambda) \quad (6)$$

Table 2. Configuration of the integrating sphere in Figure 10.

| Parameter | Port A | Port B | Port C | Port D | Port E |
|-----------|--------|--------|--------|---------------|--------|
| RSA | L | W | EC | P | P |
| RSS | L | W | C | P | P |
| RTS | L | C | W | P | P |
| TSP | P | W | O | L + C | P |
| DRK | P | W | C | L (power off) | P |

C = sample holder with samples; DRK = dark measurement; EC = empty sample holder; L = light source; O = empty port with light trap; P = white plug; RSA = reflectance ambient; RSS = reference signal; RTS = reflectance internal standard; TSP = transmittance signal; W, white reference.

Table 3. Maximum, minimum, and initial values for PROSPECT-5 in the backward inversion.

| Statistic | N | C_{ab} ($\mu\text{g}/\text{cm}^2$) | C_{xc} ($\mu\text{g}/\text{cm}^2$) | EWT (cm) | LMA (g/cm^2) |
|-----------|---|--|--|----------|--------------------------------|
| Maximum | 6 | 150 | 30.0 | 0.100 | 0.0300 |
| Minimum | 1 | 8 | 0.0 | 0.001 | 0.0010 |
| Initial | 3 | 28 | 6.3 | 0.011 | 0.0054 |

C_{ab} = chlorophyll a + b; C_{xc} = total carotenoid; EWT = equivalent water thickness; LMA = leaf mass per area; N = number of plates (the structural parameter in PROSPECT-5).

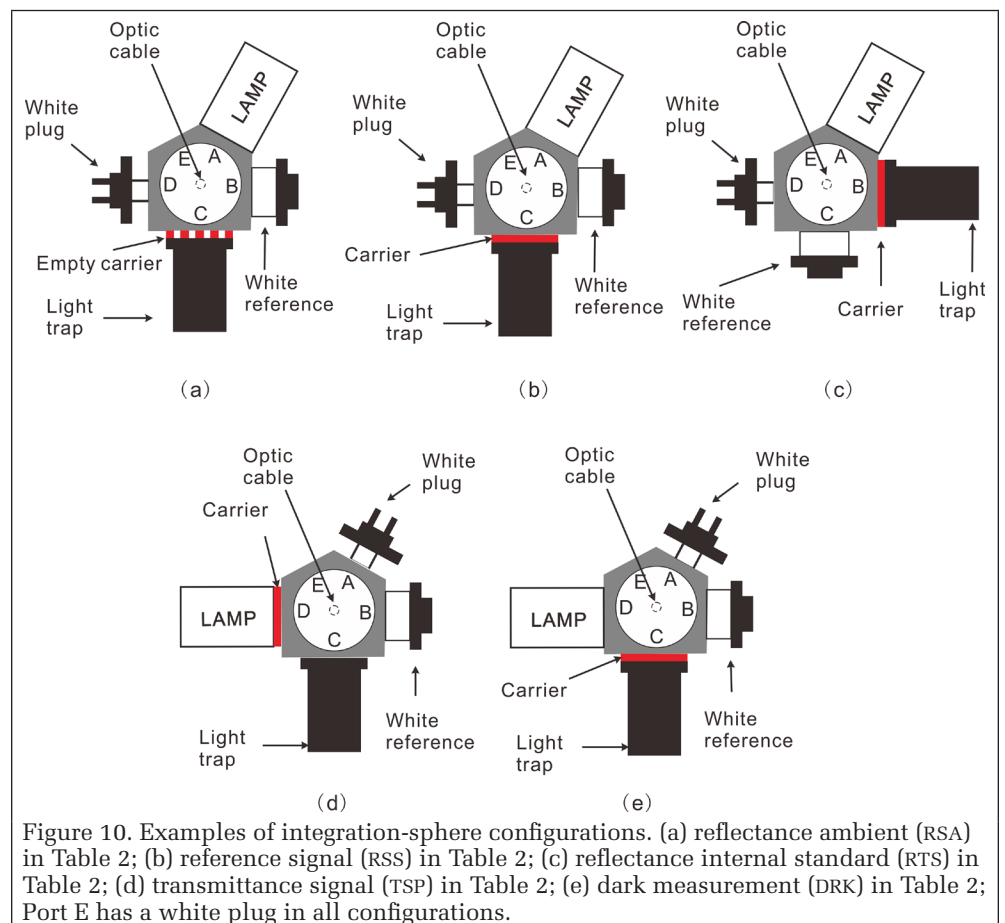


Figure 10. Examples of integration-sphere configurations. (a) reflectance ambient (RSA) in Table 2; (b) reference signal (RSS) in Table 2; (c) reflectance internal standard (RTS) in Table 2; (d) transmittance signal (TSP) in Table 2; (e) dark measurement (DRK) in Table 2; Port E has a white plug in all configurations.

where $R_r(\lambda)$ is the reflectance of the calibrated reference standard at wavelength λ (nm), which has been provided by the manufacturer of the integrating sphere. Other parameters needed in Equations 5 and 6 are listed in Table 2.

A pair of black anodized-aluminum carriers designed by Harron (2002) were used in this study to hold needle samples. Five needles were mounted in the five independent slots of the carriers against the sample port of the integrating sphere during measurements. Harron's protocol has been evaluated in detail with Boreal Ecosystem-Atmosphere Study (BOREAS; RSS-04 1994) data on the jack pine.

Measurements of Needle Biophysical Properties and Chlorophyll Contents

Following the needle optical measurements, the width and thickness of individual needles were measured using a digital caliper (Marathon Company, City, Canada). The needles were then stored in separate freezer bags and placed in a cooler with ice (0°C) for transport to a laboratory and stored at -23°C after arrival. Further measurements were conducted in a laboratory of the Ontario Forest Research Institute before the needles were dehydrated and shrunk. Needle chlorophyll content was measured using the method described by Moorthy, Miller, and Noland (2008). Table 4 provides a summary of the measured structural parameters, chlorophyll content (C_{ab}), and total carotenoid content (C_{xc}). Descriptions of the black-spruce data set are also given by Zarco-Tejada *et al.* (2004) and Zhang *et al.* (2008).

Table 4. Statistics of the structural parameters, chlorophyll content (C_{ab}), and total carotenoid content (C_{xc}) of the black-spruce data set.

| Statistic | Width (cm) | Thickness (cm) | C_{ab} ($\mu\text{g}/\text{cm}^2$) | C_{xc} ($\mu\text{g}/\text{cm}^2$) |
|---------------|-----------------|-----------------|--|--|
| Minimum | 0.11 | 0.07 | 11.97 | 3.18 |
| Maximum | 0.22 | 0.12 | 48.71 | 10.29 |
| Mean \pm SD | 0.16 \pm 0.03 | 0.09 \pm 0.01 | 28.95 \pm 8.62 | 6.33 \pm 1.62 |

Results

Accuracy of Daughtry's and Harron's Methods

We compared Daughtry's and Harron's reflectance and transmittance with the reference reflectance and transmittance of the same needle shape simulated under the same illumination conditions (Figure 11) and found that both Daughtry's and Harron's reflectance and transmittance are biased with respect to the reference. Moreover, the bias varies with wavelength.

There are larger discrepancies for Daughtry's method when measuring reflectance and transmittance at wavelengths in the near-infrared region (NIR, 800–1400 nm) and shortwave infrared (1500–1900 nm), where light is rarely absorbed. However, at wavelengths with strong absorption characteristics, such as the visible spectral region and the atmospheric window, this method shows better performance. A trade-off was found between the biases of Daughtry's reflectance and transmittance (Figure 12b). Therefore, the absorption measured by Daughtry's method agrees well with the reference absorption across the whole spectral range (400–2500 nm) if and only if multiple scattering between needles is neglected.

By contrast, Harron's reflectance and transmittance contain larger errors than Daughtry's. Both the reflectance and transmittance were underestimated across the whole spectral range compared with the reference, with more obvious underestimation in weak-absorbing spectral regions, resulting in significant overestimation of the needle absorption.

Influence of Incident Direction of Light on the Accuracy of Daughtry's and Harron's Methods

Daughtry's reflectance and transmittance were biased regardless of the incident direction ($\max |RE| > 50\%$), while no obvious bias was observed for the absorption (Figure 12), due to the trade-off between the biases of the reflectance and transmittance. So Daughtry's method will not underestimate or overestimate needle absorption if multiple scattering between needles is not considered.

When light struck on the flat sides of the needles, Daughtry's reflectance was overestimated and transmittance underestimated, whereas when it struck on the convex sides, the reflectance and transmittance were underestimated and overestimated, respectively, demonstrating the great influence of incident direction on accuracy with Daughtry's method.

The error of Daughtry's reflectance changed little across the whole spectral region when the convex sides of the needles were illuminated. But the transmittance showed much larger biases in strongly absorbing some spectral regions than others ($|RE| \approx 40\%$ near 400 nm). When the flat sides of the needles were illuminated, the reflectance contained greater errors at wavelengths where light is weakly absorbed ($|RE| > 50\%$) than at other wavelengths, but the relative error of transmittance was smaller than 10%.

Both Harron's reflectance and transmittance were negatively biased, while absorption was positively biased no matter whether the convex or flat sides of the needles were illuminated. The most

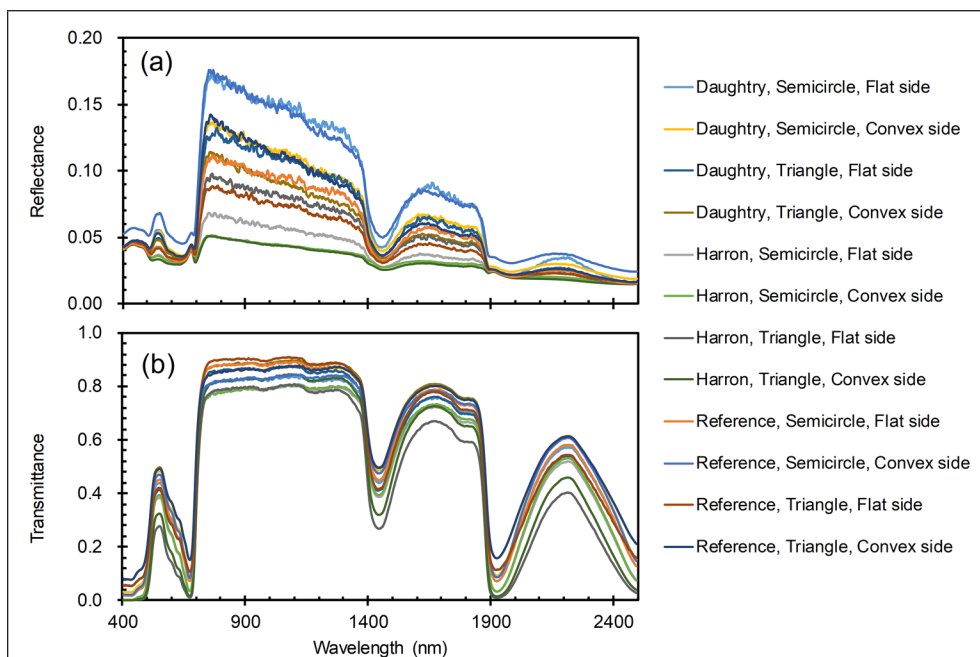


Figure 11. Simulated directional-hemispherical (a) reflectance and (b) transmittance spectra of needles with different shapes under different measurement protocols. Measurement technique, needle shape, and incident direction are noted in the legend. The concentrations of chlorophyll, total carotenoid, water, and dry matter are set to be, respectively, 720 $\mu\text{g}/\text{cm}^3$, 160 $\mu\text{g}/\text{cm}^3$, 0.34 g/cm^3 , and 0.07 g/cm^3 . The needle width is 0.15 cm. The slot width of Harron's method is set to 0.075 cm. The refractive indices are taken from PROSPECT-5.

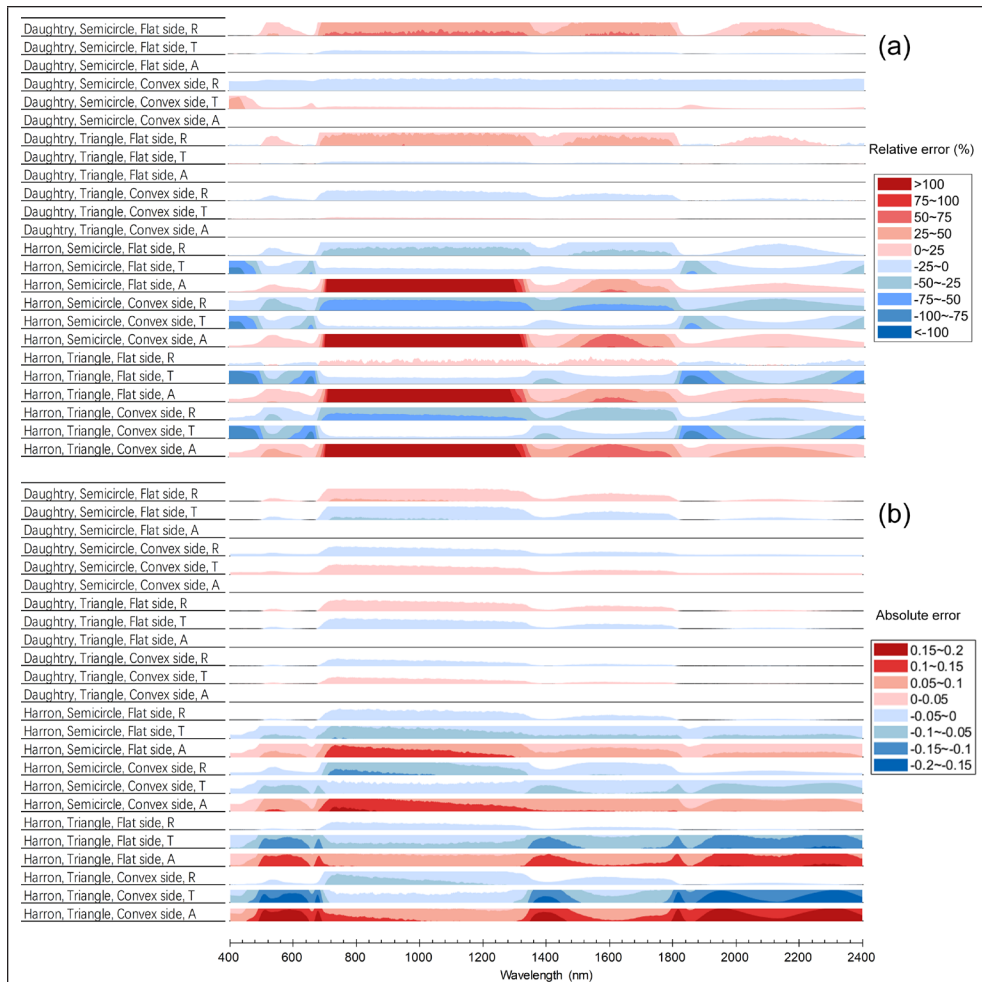


Figure 12. Horizon graph of (a) relative error and (b) absolute error of all simulated spectra. Measurement technique, leaf shape, incident direction, and spectrum type are given in the left panel. The color represents the range of error, while the height of the area plot indicates the difference between the positive relative or absolute error and the lower bound of the corresponding range (for negative relative or absolute error, the upper bound of the range). The concentrations of chlorophyll, total carotenoid, water, and dry matter are set to be, respectively, $720 \mu\text{g}/\text{cm}^3$, $160 \mu\text{g}/\text{cm}^3$, $0.34 \text{ g}/\text{cm}^3$, and $0.07 \text{ g}/\text{cm}^3$. The needle width is 0.15 cm . Relative errors of Daughtry's absorption lie in the range of -25% to 25% . The refractive indices are taken from PROSPECT-5. The error is assessed with respect to the reference proposed in this study (Equations 1 and 2).

shocking overestimation of absorption happened in NIR ($|RE| \approx 1500\%$; see Figure 12).

In general, the reflectance was measured more accurately when light was incident on the flat sides of the needles, for both Daughtry's and Harron's methods.

Influence of Needle Shape and Size on the Accuracy of Daughtry's and Harron's Methods

The errors of both methods varied with needle shape (Figure 11 and 12). NIR and shortwave infrared were the spectral regions where the largest errors of reflectance appeared. Without considering multiple scattering between needles, the absorption of needles could be measured accurately by Daughtry's method regardless of needle shape. In contrast, the absorption simulated with Harron's method was obviously overestimated, and its accuracy was more sensitive to needle shape.

Significant but wavelength-dependent differences were observed between the reflectance and transmittance of needles of different sizes regardless of measurement method (Figure 12). Increasing needle size exhibited a rising trend in needle transmittance, particularly evident in strongly absorbing spectral regions such as the visible spectral region (Figure 13). In

terms of accuracy, the relative and absolute errors of Daughtry's and Harron's reflectance and transmittance changed little with needle size (Figures 14 and 15), indicating marginal influence of needle size on the precision of Daughtry's method. The absolute errors of Harron's reflectance, transmittance, and absorption were stable across different needle sizes, but the relative error of absorption changed dramatically due to the critical variations in the reference absorption (Equation 2).

Influence of Leaf Biochemical Parameters on the Accuracy of Daughtry's and Harron's Methods

Both Daughtry's and Harron's transmittance in the visible domain shrank (Figure 16), with decreasing absolute error (Figure 17), as chlorophyll concentration increased. The largest error appeared at green wavelengths near 555 nm , where relatively less radiation was absorbed by the needles.

Daughtry's method showed excellent performance in the blue spectral domain ($400\text{--}500 \text{ nm}$ in Figure 6). When light struck the flat sides of the needles, the absolute errors of Daughtry's reflectance and transmittance in this domain were close to 0; by contrast, those of Harron's transmittance were much larger.

No bias was found for Daughtry's absorption, no matter what the chlorophyll concentration of the needle. Harron's absorption was significantly overestimated compared with the reference.

Influence of the Sample Holder's Aperture Width on the Accuracy of Harron's Method

Figure 19 displays the variations of Harron's reflectance and transmittance with the aperture width of the sample holder under the same needle shape and incident direction. The wider the aperture, the more accurate Harron's method was. When the aperture width is equal to the needle width or larger, Harron's method actually measures the defined benchmark reflectance and transmittance. The absorption of needles will always be underestimated by Harron's method as long as the aperture width is smaller than the needle width.

Influence of Mutual Shadowing Between Needles on the Accuracy of Daughtry's Method

Through comparing Daughtry's reflectance and transmittance of needle mats (three needles side by side) and individual needles, surprising needle-shape-independent consistencies arose between these two spectra sets across the whole spectral range (Figure 20), suggesting a marginal influence of mutual shadowing between needles on the accuracy of Daughtry's method.

PROSPECT-5 Inversions

When just chlorophyll and carotenoid contents were estimated with the PROSPECT-5 model, pronounced overestimation was observed for both pigments (Scheme 1 in Figure

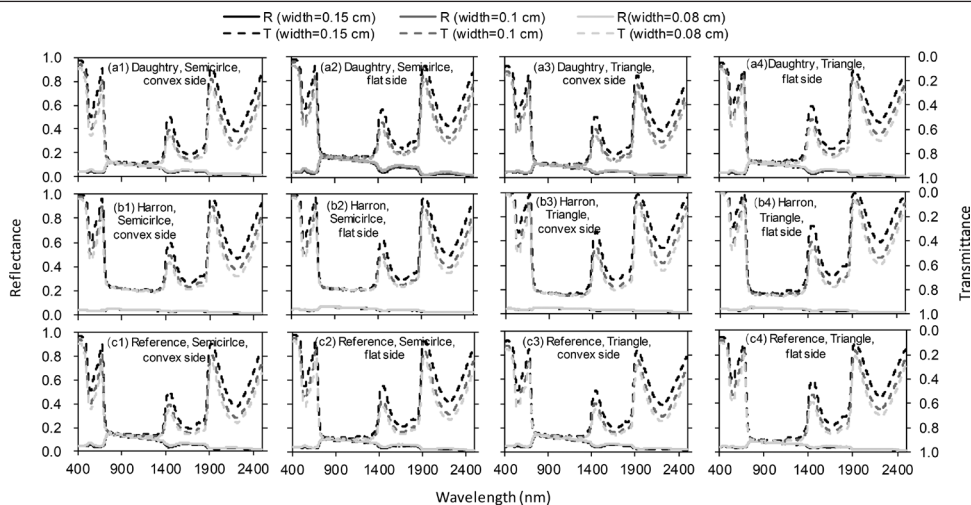


Figure 13. Daughtry's, Harron's, and defined reflectance and transmittance of different-size needles. The captions convey information about measurement protocol, needle shape, and incident direction of light. The concentrations of chlorophyll, total carotenoid, water, and dry matter are set to be, respectively, $720 \mu\text{g}/\text{cm}^3$, $160 \mu\text{g}/\text{cm}^3$, $0.34 \text{ g}/\text{cm}^3$, and $0.07 \text{ g}/\text{cm}^3$. The refractive indices are taken from PROSPECT-5. The slot width for Harron's method is set to half the needle width.

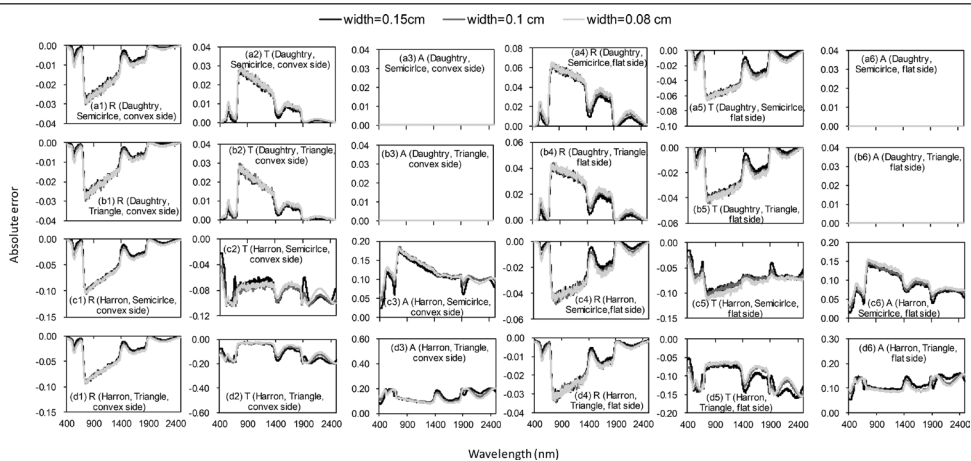


Figure 14. Absolute error of Daughtry's and Harron's methods for different-size needles. The captions convey information about spectral type, measurement technique, needle shape, and incident direction of light. The concentrations of chlorophyll, total carotenoid, water, and dry matter are set to be, respectively, $720 \mu\text{g}/\text{cm}^3$, $160 \mu\text{g}/\text{cm}^3$, $0.34 \text{ g}/\text{cm}^3$, and $0.07 \text{ g}/\text{cm}^3$. The refractive indices are taken from PROSPECT-5. The error is assessed with respect to the reference proposed in this study (Equations 1 and 2).

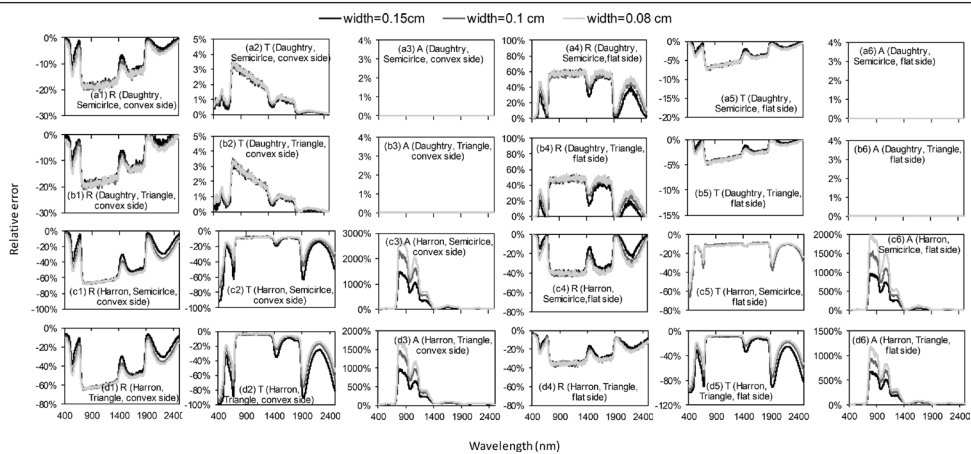


Figure 15. Relative error of Daughtry's and Harron's methods for different-size needles. The captions convey information about spectral type, measurement technique, needle shape, and incident direction of light. The concentrations of chlorophyll, total carotenoid, water, and dry matter are set to be, respectively, $720 \mu\text{g}/\text{cm}^3$, $160 \mu\text{g}/\text{cm}^3$, $0.34 \text{ g}/\text{cm}^3$, and $0.07 \text{ g}/\text{cm}^3$. The refractive indices are taken from PROSPECT-5. The error is assessed with respect to the reference proposed in this study (Equations 1 and 2).

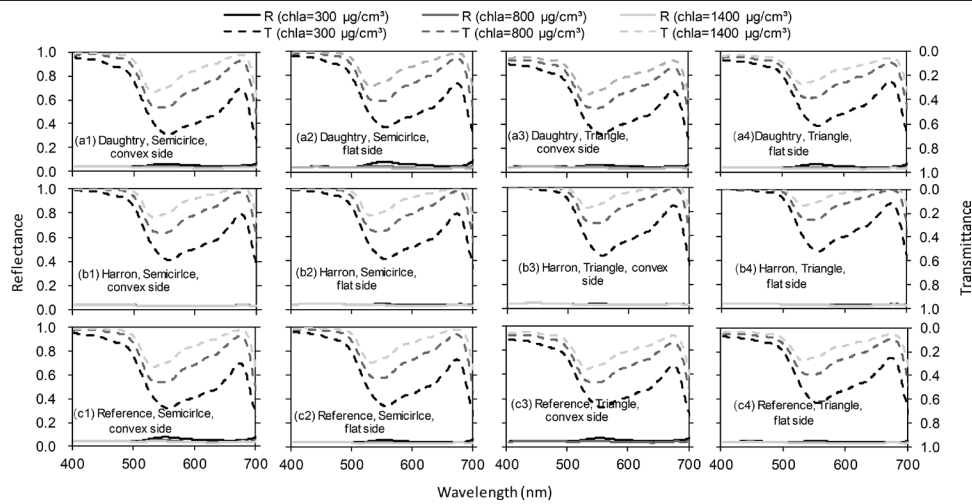


Figure 16. Daughtry's, Harron's, and defined reflectance and transmittance (visible spectral region: 400–700 nm) of needles with different chlorophyll concentrations. The captions convey information about measurement protocol, needle shape, and incident direction of light. The concentrations of total carotenoid, water, and dry matter are set to be, respectively, $160 \mu\text{g}/\text{cm}^3$, $0.34 \text{ g}/\text{cm}^3$, and $0.07 \text{ g}/\text{cm}^3$. The refractive indices are taken from PROSPECT-5. The needle width is 0.15 cm. The slot width for Harron's method is set to 0.075 cm.

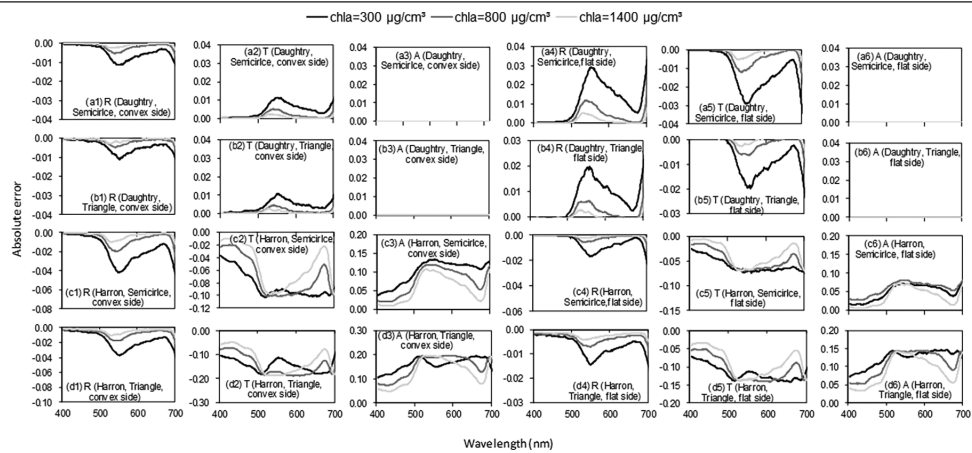


Figure 17. Absolute error of Daughtry's and Harron's methods for needles with different chlorophyll (chl_a) concentrations. The captions convey information about measurement technique, needle shape, and incident direction of light. The concentrations of total carotenoid, water, and dry matter are set to be, respectively, $160 \mu\text{g}/\text{cm}^3$, $0.34 \text{ g}/\text{cm}^3$, and $0.07 \text{ g}/\text{cm}^3$. The error is assessed with respect to the reference proposed in this study (Equations 1 and 2).

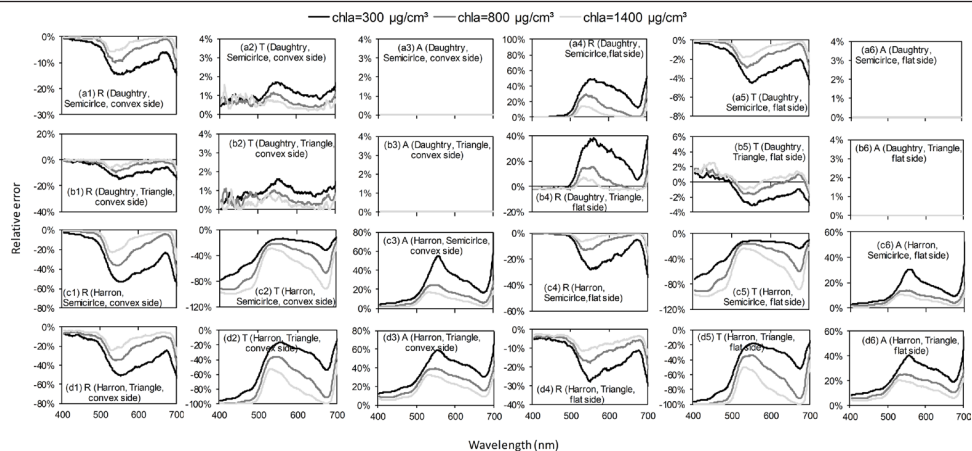


Figure 18. Relative error of Daughtry's and Harron's methods for needles with different chlorophyll (chl_a) concentrations. The captions convey information about spectral type, measurement technique, needle shape, and incident direction of light. The concentrations of total carotenoid, water, and dry matter are set to be, respectively, $160 \mu\text{g}/\text{cm}^3$, $0.34 \text{ g}/\text{cm}^3$, and $0.07 \text{ g}/\text{cm}^3$. The error is assessed with respect to the reference proposed in this study (Equations 1 and 2).

21a and 21b). The overestimation of chlorophyll was not alleviated when more kinds of biochemical constituents were added into the model inversion (Scheme 2 in Figure 21a), demonstrating that the overestimation is not caused by the inversion strategy. The model failed to estimate the carotenoid content of black-spruce needles ($R^2 = 0.087$) when other biochemical constituents, such as equivalent water thickness and leaf mass per area, were added. These observations are similar to the finding by Féret *et al.* (2019) that PROSPECT shows better performance in the estimation of leaf mass per area and equivalent water thickness when using spectral information from 1700 to 2400 nm than when using broader spectral ranges.

There are two causes that might be responsible for the failure of carotenoid estimation in Scheme 2. First, Harron's method is compromised and will cause overestimation of absorption, which cannot be quantified and may vary across samples. Second, the absorption of carotenoid is shaded by that of chlorophyll. The absorption of carotenoid is prominent in 400–560 nm. Above 560 nm, chlorophyll dominates the absorption. Dry matter also shows significant absorption in 400–560 nm. The mechanism of PROSPECT-5 inversion is to sum all the squared errors between measured and estimated reflectance and transmittance across the whole spectral range of interest and find the minimum of the least-square-based sum (Equation 4). So if the selected spectral range is wider than the absorption features of carotenoid and chlorophyll, and other constituents such as water and dry matter are added, the accuracy of carotenoid and chlorophyll estimations will degrade. The results prove that the measured biased reflectance and transmittance will cause an overestimation of the biochemical contents of needle-shaped leaves.

Discussion

Leaf DHR and DHT play an important role in both leaf-scale and canopy-scale remote-sensing studies. At the leaf scale, they are the fundamental data for leaf biochemical constituent inversions, using either spectral-index models or leaf optical-properties models. At the canopy scale, leaf DHR and DHT are often needed to evaluate or eliminate the influences of canopy structure and background on canopy reflectance (e.g., Zhang *et al.* 2008; Croft *et al.* 2015). If collected leaf spectra are compromised,

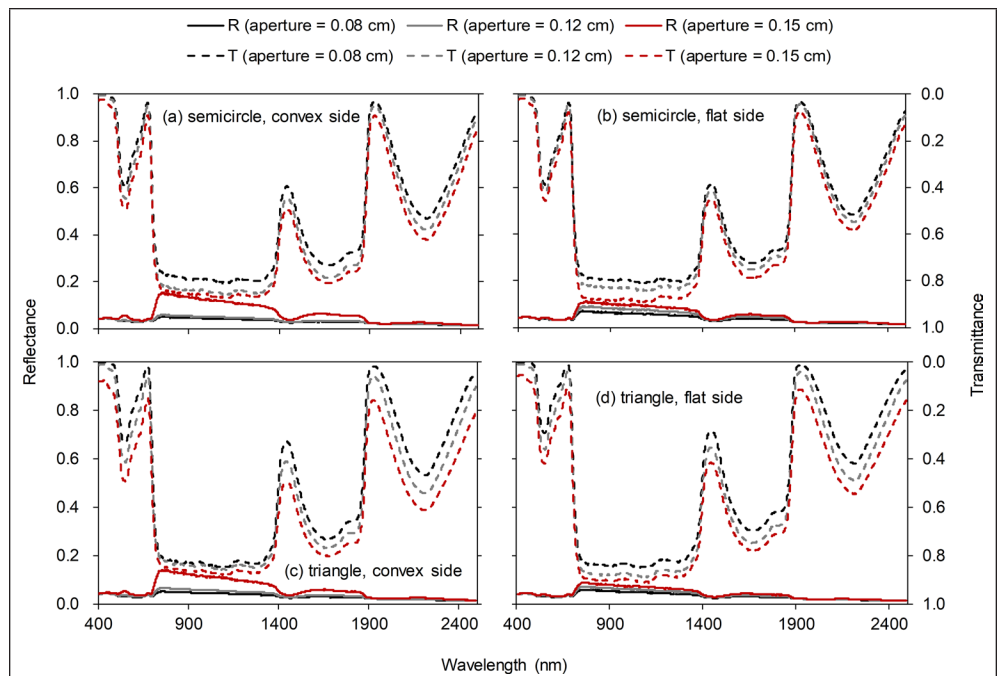


Figure 19. Harron's reflectance and transmittance when carriers with different slot widths are used. The captions convey information about needle shape and incident direction. The concentrations of total carotenoid, water, and dry matter are set to be, respectively, $160 \mu\text{g}/\text{cm}^3$, $0.34 \text{ g}/\text{cm}^3$, and $0.07 \text{ g}/\text{cm}^3$. The refractive indices are taken from PROSPECT-5. The needle width is 0.15 cm.

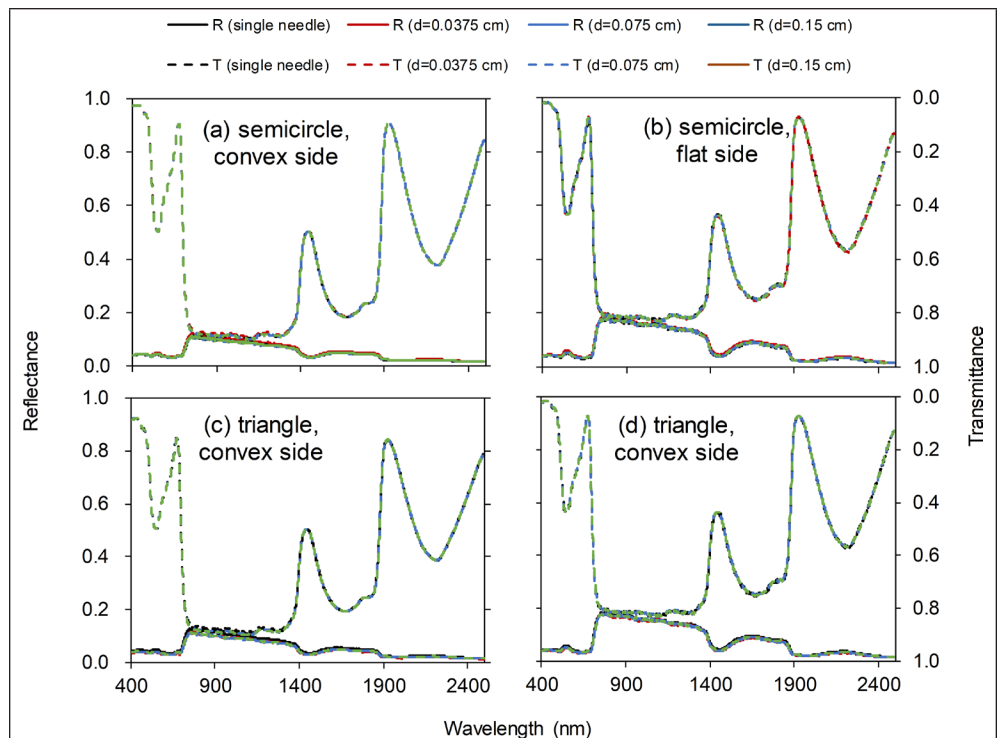


Figure 20. Daughtry's reflectance and transmittance of three needles arranged with different gap sizes. The concentrations of chlorophyll, total carotenoid, water, and dry matter are set to be, respectively, $720 \mu\text{g}/\text{cm}^3$, $160 \mu\text{g}/\text{cm}^3$, $0.34 \text{ g}/\text{cm}^3$, and $0.07 \text{ g}/\text{cm}^3$. The refractive indices are taken from PROSPECT-5.

remote-sensing models developed based on them will also be compromised, leading to problematic applications to biochemical parameter retrieval.

Due to needles' narrow and thick morphological characteristics, a clear understanding of how to distinguish between reflected and transmitted radiation is needed for the sake

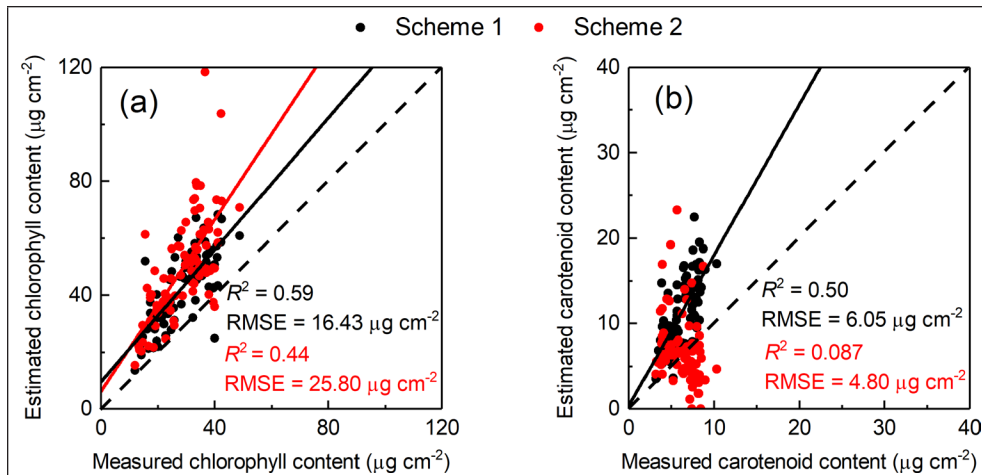


Figure 21. Results of PROSPECT-5 inversions of (a) chlorophyll and (b) total carotenoid over the black-spruce data set. The coefficients of determination (R^2) and relative mean squared error (RMSE) were calculated. Scheme 1 (black points) is to estimate only chlorophyll and carotenoid using wavelengths of 400–690 nm. Scheme 2 (red points) is to estimate chlorophyll, carotenoid, equivalent water thickness (EWT), and leaf mass per area (LMA) simultaneously using wavelengths of 400–900 nm.

of accurate reflectance and transmittance measurement; but unfortunately, this issue has not been addressed with existing techniques. This study investigated primary integrating-sphere-based spectral measurement methods for needle-shaped leaves from a theoretical point of view and gives a definition that may be helpful for the development of new measurement techniques.

Daughtry's method measures the reflectance and transmittance of needles with opposite biases, resulting in high accuracy in needle absorption measurement. The biases in reflectance and transmittance are more prominent in spectral regions characterized by weak absorption, such as NIR, than in other spectral regions. When an incident ray strikes on the surface of a needle, most (>90%) of the energy of this ray will penetrate through the surface and interact with the leaf interior according to Fresnel equations, but little radiation arrives at the shadow surface after perhaps one pass from the illuminated surface if the ray is strongly absorbed; therefore, the first one or two passes inside the needle may determine the final reflectance and transmittance of the ray, while the remaining passes of the ray play a marginal role. However, if the ray is weakly absorbed, it needs more time to decay to such a degree that the remaining passes can be neglected, resulting in potential biases of measured reflectance and transmittance relative to the defined reference due to an improper reference plane used by Daughtry's method. Mutual shadowing between needles was found to be insignificant in reducing the accuracy of Daughtry's method. This conclusion needs to be verified by experiments in further studies, as in this study the leaf interior is assumed to be homogeneous and radiative scattering is neglected. The transmittance and absorption measured by Daughtry's method are theoretically more accurate than the reflectance (overall—not absolutely—Daughtry's method may produce transmittance with large relative errors in some cases, such as in the region of 400–550 nm, when light is incident on the convex side of semicircular-shaped needles; see Figure 12). Therefore, Daughtry's transmittance and absorption can be used in spectroscopic studies of leaf biochemistry, but they are hard to apply to remote-sensing studies at the canopy scale, in which reflectance is the lead optical property.

The biased reflectance and transmittance may introduce great errors in some measured properties such as needle

surface refractive index. As mentioned before, the reflectance of a leaf includes two parts: surface reflection and internal scattering. Daughtry's method uses the surfaces of the sample holder rather than the surfaces of needles as the reference plane to distinguish reflected and transmitted radiation. As a result, some reflected radiation, from needle surfaces or interior or both, are incorrectly regarded as transmitted radiation. Current leaf optical-properties models, such as PROSPECT, use a set of fixed refractive indices to describe the reflection happening at leaf surfaces. The refractive indices were calibrated for broad leaves whose reflectance and transmittance can be measured accurately by integrating spheres without any sample holder, as the leaves are broad enough to cover the sample port of integrating spheres. In this case, the leaf surfaces are acting as the reference

plane to identify reflected and transmitted radiation, which is consistent with the definition. Therefore, the biased reflectance and transmittance measured by Daughtry's method are likely to result in unsatisfactory performance of leaf optical models. Some studies, such as by Malenovsky *et al.*, (2006), attribute the biased performance of PROSPECT with needles to the model structure developed for broad leaves, without paying sufficient attention to possible biases in measured needle reflectance and transmittance. These studies have thus recalibrated the biochemical and biophysical parameters simulated with their measured biased needle reflectance and transmittance. Actually, such recalibrations could be misleading if the measured needle reflectance and transmittance are biased. Compared with Daughtry's method, Harron's method measures both the reflectance and transmittance of needles with negative errors; therefore its measured absorption is always positively biased, which may lead to pronounced overestimation of leaf biochemical traits.

Both Daughtry's and Harron's methods take the faces of sample holders as the reference plane to distinguish between reflected and transmitted radiation; such sample holders will result in possible biases of measured reflectance and transmittance from convex objects. Therefore, the Gordian knot of accurate measurement of needle reflectance and transmittance may be the design of sample holders that can capture the reflected radiation from a convex needle surface in the forward scattering direction (away from the light source). There may be two viable solutions to cutting the knot. The first one is to design a sample holder for a single needle in an integrating sphere. The needle is placed on a flat supporting surface at the receiving side of the sphere with the following conditions: the area under the needle is black so that it does not reflect transmitted radiation through the needle, and the unshaded supporting surface is 100% white so that the radiation reflected by the needle in the forward direction can be reflected back into the integrating sphere. However, such a measuring system has a rather strict requirement for high sensitivity of the measuring sensor, since a needle is often too narrow to provide sufficient signals for measurement.

The second solution is to use multiple needles in a similar setting to the first solution's, in order to provide enough signals for measurement. With a blackened supporting surface

under each needle and white surfaces between needles, all radiation reflected by the needles in the forward direction can be reflected back to the integrating sphere. However, the radiation reflected by the white surface would interact with the needles and be partly absorbed by the needles. Hence a small reflective ridge may be placed between needles to prevent mutual scattering between them. A practical solution would be to place each needle in a concave trough with width selected to minimize the scattering back to the same needle. Although we have not found a practical solution to this complex issue, we would like to specify the requirements for measuring reflectance from a convex needle surface: the surface should be fully exposed to the incoming radiation, the interfusion of reflected and transmitted radiation on convex needle surfaces should be avoided, and for a holder with multiple needles, multiple scattering among needles should be avoided.

Conclusions

This study demonstrates that the directional-hemispherical reflectance and transmittance of needle-shaped leaves measured by two widely used techniques with integrating spheres can be significantly biased, which is obvious across the whole spectral range for Harron's method and remarkable at spectral regions with weak absorption characteristics for Daughtry's method. This finding is of fundamental importance for diverse research fields where accurate DHR and DHT of needle-shaped leaves are needed. To address this issue, we proposed a definition of needle leaf reflectance and transmittance based on a reference plane which separates the illuminated and shaded sides of needles. We also proposed basic requirements for making measurements of needle reflectance and transmittance using an integrating sphere, including a collimated light source, full exposure of the entire needles to the light source, and exposure of the largest side to the light source. The definition given in this study can serve as a theoretical foundation for the development of new measurement techniques.

Acknowledgments

This research was supported by the National Natural Science Foundation of China (41971304, 41671343, 41371070), the Strategic Priority Research Program of Chinese Academy of Sciences (XDA20060402) and the key research and development program for global change and adaptation (2016YFA0600202). We hereby express our sincere gratitude to Stéphane Jacquemoud of iPGP (Institut de physique du globe de Paris) and Jean-Baptiste Féret and others for providing the source code of PROSPECT-5. We also thank Yongqing Zhang and Holy Croft for providing the black-spruce data set used in this study.

References

Abdullah, H., R. Darvishzadeh, A. K. Skidmore, T. A. Groen and M. Heurich. 2018. European spruce bark beetle (*Ips typographus*, L.) green attack affects foliar reflectance and biochemical properties. *International Journal of Applied Earth Observation and Geoinformation* 64:199–209.

Astrup, R., P. Y. Bernier, H. Genet, D. A. Lutz and R. M. Bright. 2018. A sensible climate solution for the boreal forest. *Nature Climate Change* 8 (1):11–12.

Bousquet, L., S. Lachérade, S. Jacquemoud and I. Moya. 2005. Leaf BRDF measurements and model for specular and diffuse components differentiation. *Remote Sensing of Environment* 98 (2–3):201–211.

Brandt, J. P., M. D. Flannigan, D. G. Maynard, I. D. Thompson and W.J.A. Volney. 2013. An introduction to Canada's boreal zone: Ecosystem processes, health, sustainability, and environmental issues. *Environmental Reviews* 21 (4):207–226.

Chen, J. M. and T. A. Black. 1992. Defining leaf area index for non-flat leaves. *Plant, Cell & Environment* 15 (4):421–429.

Comar, A., F. Baret, F. Viénot, L. Yan and B. de Solan. 2012. Wheat leaf bidirectional reflectance measurements: Description and quantification of the volume, specular and hot-spot scattering features. *Remote Sensing of Environment* 121:26–35.

Croft, H., J. M. Chen, Y. Zhang, A. Simic, T. L. Noland, N. Nesbitt and J. Arabian. 2015. Evaluating leaf chlorophyll content prediction from multispectral remote sensing data within a physically-based modelling framework. *ISPRS Journal of Photogrammetry and Remote Sensing* 102:85–95.

Daughtry, C.S.T., L. L. Biehl and K. J. Ranson. 1989. A new technique to measure the spectral properties of conifer needles. *Remote Sensing of Environment* 27 (1):81–91.

Dawson, T. P., P. J. Curran and S. E. Plummer. 1998. LIBERTY—Modeling the effects of leaf biochemical concentration on reflectance spectra. *Remote Sensing of Environment* 65 (1):50–60.

Féret, J.-B., C. François, G. P. Asner, A. A. Gitelson, R. E. Martin, L.P.R. Bidet, S. L. Ustin, G. le Maire and S. Jacquemoud. 2008. PROSPECT-4 and 5: Advances in the leaf optical properties model separating photosynthetic pigments. *Remote Sensing of Environment* 112 (6):3030–3043.

Féret, J.-B., G. le Maire, S. Jay, D. Berveiller, R. Bendoula, G. Hmimina, A. Cheraïet, J. C. Oliveira, F. J. Ponzoni, T. Solanki, F. de Boissieu, J. Chave, Y. Nouvellon, A. Porcar-Castell, C. Proisy, K. Soudani, J.-P. Gastellu-Etchegorry and M.-J. Lefèvre-Fonollosa. 2019. Estimating leaf mass per area and equivalent water thickness based on leaf optical properties: Potential and limitations of physical modeling and machine learning. *Remote Sensing of Environment* 231:110959.

Ganapol, B. D., L. F. Johnson, P. D. Hammer, C. A. Hlavka and D. L. Peterson. 1998. LEAFMOD: A new within-leaf radiative transfer model. *Remote Sensing of Environment* 63 (2):182–193.

Grant, L., C.S.T. Daughtry and V. C. Vanderbilt. 1993. Polarized and specular reflectance variation with leaf surface features. *Physiologia Plantarum* 88 (1):1–9.

Harron, J. W. 2002. Optical properties of phytoelements in conifers. Master's thesis, York University.

Harron, J. and Miller, J., 2002. An alternate methodology for reflectance and transmittance measurements of conifer needles, *Proceedings of the 17th Canadian Symposium on Remote Sensing*, 1995, Saskatoon, Saskatchewan, Canada, pp. 654–661.

Hosgood, B., S. Jacquemoud, G. Andreoli, J. Verdebout, G. Pedrini and G. Schmuck. 1995. *Leaf Optical Properties Experiment 93 (LOPEX93)*. Catalogue No. CL-NA-16095-EN-C. Luxembourg: Office for Official Publications of the European Communities.

Hovi, A., P. Raitio and M. Rautiainen. 2017. A spectral analysis of 25 boreal tree species. *Silva Fennica* 51 (4):7753.

Jacquemoud, S. and F. Baret. 1990. PROSPECT: A model of leaf optical properties spectra. *Remote Sensing of Environment* 34 (2):75–91.

Jacquemoud, S. and L. Ustin. 2008. Modeling Leaf Optical Properties. <http://photobiology.info/Jacq_Ustin.html> Accessed 25 April 2018.

Jacquez, J. A. and H. F. Kuppenheim. 1955. Theory of the integrating sphere. *Journal of the Optical Society of America* 45 (6):460–470.

Lukeš, P., P. Stenberg, M. Rautiainen, M. Möttöus and K. M. Vanhatalo. 2013. Optical properties of leaves and needles for boreal tree species in Europe. *Remote Sensing Letters* 4 (7):667–676.

MacDicken, K. Ö. Jonsson, L. Piña, L. Marklund, S. Maulo, V. Contessa, Y. Adikari, M. Garzuglia, E. Lindquist, G. Reams and R. D'Annunzio. 2015. *Global Forest Resources Assessment 2015: How Are the World's Forests Changing?*, 2nd ed. Rome, Italy: Food and Agriculture Organization of the United Nations.

Maier, S. W., W. Lüdeker and K. P. Günther. 1999. SLOP: A revised version of the stochastic model for leaf optical properties. *Remote Sensing of Environment* 68 (3):273–280.

- Malenovský, Z., J. Albrechtová, Z. Lhotáková, R. Zurita-Milla, J.G.P.W. Clevers, M. E. Schaepman and P. Cudlín. 2006. Applicability of the PROSPECT model for Norway spruce needles. *International Journal of Remote Sensing* 27 (24):5315–5340.
- Marín, S.d.T., M. Novák, K. Klančnik and A. Gaberščik. 2016. Spectral signatures of conifer needles mainly depend on their physical traits. *Polish Journal of Ecology* 64 (1):1–13.
- McClendon, J. H. 1984. The micro-optics of leaves. I. Patterns of reflection from the epidermis. *American Journal of Botany* 71 (10):1391–1397.
- Mesarch, M. A., E. A. Walter-Shea, G. P. Asner, E. M. Middleton and S. S. Chan. 1999. A revised measurement methodology for conifer needles spectral optical properties: Evaluating the influence of gaps between elements. *Remote Sensing of Environment* 68 (2):177–192.
- Middleton, E. M., S. S. Chan, M. A. Mesarch and E. A. Walter-Shea. 1996. A revised measurement methodology for spectral optical properties of conifer needles. Pages 1005–1009 in *IGARSS '96: 1996 International Geoscience and Remote Sensing Symposium*, held in Lincoln, Neb., 27–31 May 1996. Los Alamitos, Calif.: IEEE.
- Miller, O. E. and A. J. Sant. 1958. Incomplete integrating sphere. *Journal of the Optical Society of America* 48 (11):828–831.
- Moorthy, I., J. R. Miller and T. L. Noland. 2008. Estimating chlorophyll concentration in conifer needles with hyperspectral data: An assessment at the needle and canopy level. *Remote Sensing of Environment* 112 (6):2824–2838.
- Mõttus, M., A. Hovi and M. Rautiainen. 2017. Theoretical algorithm and application of a double-integrating sphere system for measuring leaf transmittance and reflectance spectra. *Applied Optics* 56 (3):563–571.
- Noda, H. M., T. Motohka, K. Murakami, H. Muraoka and K. N. Nasahara. 2013. Accurate measurement of optical properties of narrow leaves and conifer needles with a typical integrating sphere and spectroradiometer. *Plant, Cell & Environment* 36 (10):1903–1909.
- Olascoaga, B., A. Mac Arthur, J. Atherton and A. Porcar-Castell. 2016. A comparison of methods to estimate photosynthetic light absorption in leaves with contrasting morphology. *Tree Physiology* 36 (3):368–379.
- Pickering, J. W., C.J.M. Moes, H.J.C.M. Sterenborg, S. A. Prah and M.J.C. van Gemert. 1992. Two integrating spheres with an intervening scattering sample. *Journal of the Optical Society of America A* 9 (4):621–631.
- Pickering, J. W., S. A. Prah, N. van Wieringen, J. F. Beek, H.J.C.M. Sterenborg and M.J.C. van Gemert. 1993. Double-integrating-sphere system for measuring the optical properties of tissue. *Applied Optics* 32 (4):399–410.
- Potůčková, M., L. Červená, L. Kupková, Z. Lhotáková, P. Lukeš, J. Hanuš, J. Novotný and J. Albrechtová. 2016. Comparison of reflectance measurements acquired with a contact probe and an integration sphere: Implications for the spectral properties of vegetation at a leaf level. *Sensors* 16 (11):1801.
- Qiu, F., J. M. Chen, W. Ju, J. Wang, Q. Zhang and M. Fang. 2018. Improving the PROSPECT model to consider anisotropic scattering of leaf internal materials and its use for retrieving leaf biomass in fresh leaves. *IEEE Transactions on Geoscience and Remote Sensing* 56 (6):3119–3136.
- Rajewicz, P. A., J. Atherton, L. Alonso and A. Porcar-Castell. 2019. Leaf-level spectral fluorescence measurements: Comparing methodologies for broadleaves and needles. *Remote Sensing* 11 (5):532.
- Schaepman-Strub, G., M. E. Schaepman, T. H. Painter, S. Dangel and J. V. Martonchik. 2006. Reflectance quantities in optical remote sensing—definitions and case studies. *Remote Sensing of Environment* 103 (1):27–42.
- Wang, B. J. and W. Ju. 2017. Limitations and improvements of the leaf optical properties model Leaf Incorporating Biochemistry Exhibiting Reflectance and Transmittance Yields (LIBERTY). *Remote Sensing* 9 (5):431.
- Yáñez-Rausell, L., M. E. Schaepman, J.G.P.W. Clevers and Z. Malenovský. 2014. Minimizing measurement uncertainties of coniferous needle-leaf optical properties, part I: Methodological review. *IEEE Journal of Selected Topics in Applied Earth Observations and Remote Sensing* 7 (2):399–405.
- Zarco-Tejada, P. J., J. R. Miller, J. Harron, B. Hu, T. L. Noland, N. Goel, G. H. Mohammed and P. Sampson. 2004. Needle chlorophyll content estimation through model inversion using hyperspectral data from boreal conifer forest canopies. *Remote Sensing of Environment* 89 (2):189–199.
- Zhang, Y., J. M. Chen, J. R. Miller and T. L. Noland. 2008a. Leaf chlorophyll content retrieval from airborne hyperspectral remote sensing imagery. *Remote Sensing of Environment* 112 (7):3234–3247.
- Zhang, Y., J. M. Chen, J. R. Miller and T. L. Noland. 2008b. Retrieving chlorophyll content in conifer needles from hyperspectral measurements. *Canadian Journal of Remote Sensing* 34 (3):296–310.

SUSTAINING MEMBERS

Aerial Services, Inc.

Cedar Falls, Iowa
www.AerialServicesInc.com
Member Since: 5/2001

Airbus Defense and Space

Chantilly, Virginia
www.intelligence-airbusds.com
Member Since: 11/2018

Ayres Associates

Madison, Wisconsin
www.AyresAssociates.com
Member Since: 1/1953

Cardinal Systems, LLC

Flagler Beach, Florida
www.cardinalsystems.net
Member Since: 1/2001

Dewberry

Fairfax, Virginia
www.dewberry.com
Member Since: 1/1985

Esri

Redlands, California
www.esri.com
Member Since: 1/1987

F.R. Aleman & Associates, Inc.

Miami, Florida
https://fr-aleman.com/
Member Since: 7/2020

GeoWing Mapping, Inc.

Richmond, California
www.geowingmapping.com
Member Since: 12/2016

GPI Geospatial Inc.

formerly **Aerial Cartographics of America, Inc. (ACA)**
Orlando, Florida
www.aca-net.com
Member Since: 10/1994

Green Grid Inc.

San Ramon, California
www.greengridinc.com
Member Since: 1/2020

Kucera International

Willoughby, Ohio
www.kucerainternational.com
Member Since: 1/1992

L3Harris Corporation

Broomfield, Colorado
www.harris.com
Member Since: 6/2008

Pickett and Associates, Inc.

Bartow, Florida
www.pickettusa.com
Member Since: 4/2007

Quantum Spatial, Inc.

Sheboygan Falls, Wisconsin
www.quantumspatial.com
Member Since: 1/1974

Sanborn Map Company

Colorado Springs, Colorado
www.sanborn.com
Member Since: 10/1984

Surveying And Mapping, LLC (SAM)

Austin, Texas
www.sam.biz
Member Since: 12/2005

T3 Global Strategies, Inc.

Bridgeville, Pennsylvania
https://t3gs.com/
Member Since: 6/2020

Towill, Inc.

San Francisco, California
www.towill.com
Member Since: 1/1952

Trimble

Munich, Germany
www.trimble.com/geospatial
Member Since: 4/1942

Wingtra

Zurich, Switzerland
https://wingtra.com/
Member Since: 6/2020

Woolpert LLP

Dayton, Ohio
www.woolpert.com
Member Since: 1/1985

SUSTAINING MEMBER BENEFITS

Membership

- ✓ Provides a means for dissemination of new information
- ✓ Encourages an exchange of ideas and communication
- ✓ Offers prime exposure for companies

Benefits of an ASPRS Membership

- Complimentary and discounted Employee Membership*
- E-mail blast to full ASPRS membership per year*
- Professional Certification Application fee discount for any employee
- Discounts on *PE&RS* Classified Ad
- Member price for ASPRS publications
- Discount on group registration to ASPRS virtual conferences
- Sustaining Member company listing in ASPRS directory/website
- Hot link to company website from Sustaining Member company listing page on ASPRS website
- Press Release Priority Listing in *PE&RS* Industry News
- Priority publishing of Highlight Articles in *PE&RS* plus, 20% discount off cover fee, one per year
- Discount on *PE&RS* full-page advertisement
- Exhibit discounts at ASPRS sponsored conferences (exception ASPRS/ILMF)
- Free training webinar registrations per year*
- Discount on additional training webinar registrations for employees
- Discount for each new SMC member brought on board (Discount for first year only)

*quantity depends on membership level

Pavement Macrotexture Determination Using Multi-View Smartphone Images

Xiangxi Tian, Yong Xu, Fulu Wei, Oguz Gungor, Zhixin Li, Ce Wang, Shuo Li, and Jie Shan

Abstract

Pavement macrotexture contributes greatly to road surface friction, which in turn plays a vital role in reducing road accidents. Conventional methods for macrotexture measurement are either expensive, time-consuming, or of poor repeatability. Based on multi-view smartphone images collected in situ, this paper develops and evaluates an affordable and convenient alternative approach for pavement macrotexture measurement. Photogrammetric computer vision techniques are first applied to create high resolution point clouds of the pavement. Analytics are then developed to determine the macrotexture metric: mean profile depth by using the image-based point clouds. Experiments are carried out with 790 images over 25 spots on three state routes and six spots at an Indiana Department of Transportation test site. We demonstrate multi-view smartphone images can yield results comparable to the ones from the conventional laser texture scanner. It is expected that the developed approach can be adopted for large scale operational uses.

Introduction

The quality properties of road pavements have direct and significant impacts on road safety. According to *Indiana Crash Facts 2017* (Sapp, Thelin, and Nunn 2017), about 200 000 vehicle crashes occurred in Indiana every year from 2013 to 2017, of which about 34 000 accidents resulted in injuries and 755 accidents caused fatalities. Twenty percent of these accidents were further attributed to insufficient surface friction on road curves.

It is therefore essential to provide adequate friction and drainage to reduce the possibility of accidents on roads. These two properties are mainly determined by pavement (surface) textures. Pavement texture, which can be defined as the deviation of a pavement surface from a true planar surface (Li, Wang, and Li 2016), directly affects various parameters resulting from tire-road interactions such as friction, tire noise, skid resistance, tire wear, rolling resistance, splash and spray, traffic vibration, etc. (Ejsmont *et al.* 2016; Das, Rosauer, and Bald 2015; Yaacob *et al.* 2014). It was suggested at the 1987 Permanent International Association of Road Congresses (PIARC), depending on the amplitude and wavelength of a feature, to divide the pavement surface characteristics (the

Xiangxi Tian, Zhixin Li, Ce Wang, and Jie Shan are with Lyles School of Civil Engineering, Purdue University, West Lafayette, IN 47907 (jshan@purdue.edu).

Yong Xu is with the School of Geographical Sciences, Guangzhou University, Guangzhou, Guangdong 510006, China.

Fulu Wei is with the Key Laboratory of Road and Traffic Engineering, Ministry of Education, Tongji University, Shanghai 201804, China.

Oguz Gungor is with the Department of Geomatics Engineering, Karadeniz Technical University, Trabzon 61080, Turkey.

Shuo Li is with the Division of Research and Development, Indiana Department of Transportation, West Lafayette, IN 47906.

geometric profile of a road in the vertical plane) in four categories: roughness (unevenness), megatexture, macrotexture, and microtexture (Dong, Prozzi, and Ni 2019; Bitelli *et al.* 2012; Dunford 2013).

Roughness refers to the unevenness, potholes, and large cracks on road surfaces that are larger than a tire footprint (Dong, Prozzi, and Ni 2019; Bitelli *et al.* 2012; Dunford 2013). Megatexture is associated with deviations in wavelengths from 50 mm to 500 mm and vertical amplitudes ranging from 0.1 mm to 50 mm (Dong, Prozzi, and Ni 2019; Dunford 2013). Texture of this size is mainly caused by poor construction practices or surface deterioration. This level of texture causes vibrations in tire walls, resulting in vehicle noise and some external noise. Macrotexture and microtexture refer to the relatively small pavement surface irregularities that primarily affect friction and skid resistance. Macrotexture refers to the changes in wavelengths ranging from 0.5 mm to 50 mm horizontally and variations ranging from 0.1 mm to 20 mm vertically (Dong, Prozzi, and Ni 2019). However, microtexture, which corresponds to wavelengths less than 0.5 mm horizontally and vertical amplitudes up to 0.2 mm, is related to the roughness of the individual stone elements used in the surface layer and to the natural mineral aggregate (Bitelli *et al.* 2012).

Although both microtexture and macrotexture contribute to pavement friction, there is currently no practical procedure for direct measurement of the microtexture profile in traffic (Dong, Prozzi, and Ni 2019; Henry 2000). The PIARC Model for the International Friction Index avoids the need for measuring microtexture if macrotexture measures are available. A measurement at any slip speed, together with the macrotexture parameter, determines the friction as a function of the slip speed (Henry 2000). The typical parameter to describe pavement macrotexture is the mean profile depth (MPD) or the mean texture depth (MTD). MPD is linearly related to MTD and is usually converted to MTD when comparing different macrotexture calculation methods (Fisco and Sezen 2014; Henry 2000).

The conventional methods for determining road macrotexture include the sand patch method, the outflow method, and laser profiling. The sand patch method is operator-dependent, and the test results have poor repeatability (Sengoz, Topal, and Tanyel 2012). Other problems with the sand patch method include that on surfaces with very deep textures, it is very easy to overestimate the texture depth (Fisco and Sezen 2014), and accurate sand patch testing cannot be done when the road surface is sticky or wet (Praticò and Vaiana 2015). As is the case with the sand patch method, the outflow method also is labor-intensive and time-consuming, and the reliability of the results depends largely on the operator. The circular laser-based device has been deployed for routine macrotexture measurement since 2002 (Abe *et al.* 2001), and the more portable handheld laser meter, such as the Ames

Photogrammetric Engineering & Remote Sensing
Vol. 86, No. 10, October 2020, pp. 643–651.
0099-1112/20/643–651

© 2020 American Society for Photogrammetry
and Remote Sensing
doi: 10.14358/PERS.86.10.643

laser texture scanner (LTS) and ELAtext meter (Patzak *et al.* 2016), were used and evaluated for macrotexture measurement. Laser-based linear profiling devices have been shown to be able to improve testing efficiency to a great degree (Fisco and Sezen 2014). White, Ward, and Jamieson (2019) showed that the macrotexture measurement results from an ELAtext meter were reliable compared to the sand patch method. The advantages of the laser-based device over the sand patch method is that it is more portable, repeatable, efficient, and less operator-dependent, while the major defect for the laser-based device is its high cost (White, Ward, and Jamieson 2019). Moreover, its high cost also restricts its use over large areas for multi-division transportation agencies.

As an alternative to the methods described above, there have also been studies using close-range photogrammetry techniques to characterize macrotexture properties. Close-range photogrammetry, although more popular in other areas, was implemented on pavement characteristic measurement by Georgopoulos, Loizos, and Flouda (1995). Chandler, Fryer, and Jack (2005) demonstrated the capability of the low-cost digital camera for pavement surface measurement. Since then, image-based methods using digital cameras or camera systems has been studied on pavement surface measurement. Gendy *et al.* (2011) introduced a photometric stereo system designed by themselves for pavement macrotexture measurement. This system, named PhotoTexture, was built inside a 0.6 m × 0.6 m × 0.6 m box comprising of one camera and an optic light source with adjustable illumination intensity and adjustable direction. The PhotoTexture system captured three images of pavement under three different incident illumination directions, whereas the camera remains still. The images were then processed to produce a 3D recovery of the pavement (Gendy *et al.* 2011). However, the system is large in size and requires an extra adjustable lighting, which restricts its portability and makes it inconvenient for measurement.

Sarker, Dias-da-Costa, and Hadighen (2019) used a Nikon D810 camera fitted on a tripod to analyze rough texture of aggregates. Edmondson *et al.* (2019) captured multiple images (5472 × 3648 pixels) using a single-lens reflex camera with 50 mm fixed focal length mounted on a camera tripod and dolly. Three-dimensional (3D) point clouds were reconstructed by the structure-from-motion (SfM) method with the collected images. The distance between the camera and pavement was adjusted and measured using the tripod. With the comparison between the results from 3D point clouds and a 3D smart laser profile sensor, they concluded that close-range photogrammetry is an effective alternative method for pavement evaluation (Edmondson *et al.* 2019). The major restriction of this method was the use of a special camera system and that the georeferencing was accomplished by the precalibrated location and angle of the camera against the pavement. The camera system was required to be fixed within a known-dimension box or a tripod to capture pictures, causing its poor portability.

The SfM method used by Edmondson *et al.* (2019) for macrotexture measurement was first proposed in by Ullman (1979). SfM uses images collected from different viewpoints but differs from traditional photogrammetry in that it automatically estimates the interior and exterior orientation parameters without necessarily using any ground control points (GCP) established on the ground and seen in photos (Micheletti, Chandler, and Lane 2014; Westoby *et al.* 2012). Developed in the machine vision arena, this is mostly achieved by precisely matching a large number of corresponding points in the images obtained at many different viewpoints. However, SfM requires a much larger overlap in sequentially captured images, just as in the case where one uses a moving sensor to create the 3D geometry of a structure, thus justifying the method's SfM name (Micheletti, Chandler, and Lane 2014). One of the significant steps in SfM implementation is to detect, describe, and match the corresponding key points between different images.

The most representative method is Scale Invariant Feature Transform (Lowe 1999; Lowe 2004) and its many variations. The rest of SfM is very similar to the bundle adjustment technique in traditional photogrammetry (Ullman 1979).

Different from the camera systems mentioned above, another way to provide georeferencing for 3D reconstruction from images is to using control points on the pavement. In this scenario, the camera can be simply handheld, and the convenience is highly improved. McQuaid *et al.* (2013) used a Canon™ EOS 400D digital camera fitted with a calibrated 60 mm macro lens to reconstruct the 3D surface and quantified the microtexture of the test specimen in a lab environment. In their experiment, the test specimen was fitted in a calibrated control framework rig with 12 control points and photographed (McQuaid *et al.* 2013). Similarly, using a handheld Canon 6D EOS digital full frame single lens reflex camera, Kogbara *et al.* (2018) captured 12 images for each study spot on a pavement constructed in 2010 and generated dense point clouds of pavement surfaces with 3DF Zephyr Pro v3.142 proprietary software (3DFlow, Verona, Italy), upon which the surface texture parameters were calculated. In their study *in situ*, a 300-mm nominal length scale ruler was placed on the pavement providing georeferencing (Kogbara *et al.* 2018). Both studies show that the calibrated network of control points or scale ruler, acting as a georeferencing frame during 3D reconstruction, are capable of reconstructing the pavement surface. It is more convenient for measurement compared to a complicated camera system.

Despite all of the above studies, the quality of the reconstructed point cloud was not discussed in detail in this research. Furthermore, no studies were found in the reviewed literature using multiple images collected by smartphone cameras, which is much more convenient, flexible, and affordable. The potential and capability using tens of smartphone images with recent, advanced computer vision techniques has not been fully explored. Furthermore, in terms of monetary expense, the market price for a Canon 6D EOS (camera body only) is more than twice of an iPhone 8Plus (~\$1699.00 versus \$599 in 2020). Considering the broad popularity of smartphones, using a smartphone camera to measure the pavement surface would be a much cheaper and more convenient approach to determine the pavement macrotexture, and is expected to be widely adopted by road construction and maintenance industry and agencies. However, a major problem with the smartphone camera is its coarser resolution with respect to a high-end professional camera. For instance, the resolution of the Canon 6D EOS is 20.2 MP while the resolution of the camera on iPhone 8Plus is 12 MP. As such, there is a need to extend current work with newly available and affordable smartphone images for pavement macrotexture measurement, which requires a submillimeter accuracy.

This paper combines the strengths of computer vision using a large number of multi-view images and traditional photogrammetry relying on ground control for precise pavement macrotexture measurement. With minimal ground control, the novel approach uses smartphone images collected onsite to generate accurate and dense 3D pavement point clouds by the SfM and multi-view stereo (MVS) techniques. Then, related analytics is developed to determine and analyze the road pavement macrotexture. To evaluate our image-based solution, an Ames LTS is used to provide reference measurement. Based on the comparison between the results from the image-based method and the Ames LTS, we demonstrate the promising capability of the smartphone camera on precise pavement macrotexture measurement. It is shown to be a convenient, cost-effective, and alternative method for pavement macrotexture measurement.

The remainder of this paper proceeds as follows. The section “Equipment and Data Collection” describes the equipment, data collection procedure, and the sites of data collection. The section “Methodology” presents the definition of

MPD and its calculation from a point cloud. Section “Results and Evaluation” first discusses the quality of the 3D point clouds reconstructed from smartphone images. The results of the image-based MPD are then presented and evaluated with reference to the ones from the LTS. In the conclusion section, major results and contributions of this paper are summarized along with possible future developments.

Equipment and Data Collection

Equipment

Both an LTS and a smartphone were used for data collection. Figure 1 presents the Ames LTS 9400 used in this research. It was last calibrated in 2018 and can calculate the pavement’s MPD, texture profile index, estimated texture depth, and root-mean-square (RMS). The specifications of LTS are listed in Table 1. The LTS immediately displays the measurement results on the liquid crystal display. As for measuring MPD, the LTS scans ten 100-mm profiles along the road direction. However, the ten profiles are unevenly spaced across the road direction. The average point spacing within a profile was 0.014286 mm. The MPD for each profile was calculated and the arithmetic mean of the ten MPDs was considered as the MPD over the area measured. In this study, the LTS is mainly used for measuring the MPD for pavement surface and is used as a reference method compared to the proposed image-based method.

The pavement images were collected with a commonly used smartphone, iPhone 8 Plus, as shown in Figure 1. Table 2 lists its specifications. The resolution of its images is 4032 pixels × 3024 pixels. The smartphone has two 12 MP rear cameras, a wide-angle camera with an f/1.8 aperture, and a telephoto camera with an f/2.8 aperture. When taking a photo, only the wide-angle camera is activated by default, while the telephoto camera is activated only when the zoom factor is 2× or higher. The default option is recommended to minimize the number of images to be taken *in situ* from a convenient distance to the road.

To provide control and reference for measurement, a control frame shown in Figure 1 is placed in the scene when the images are collected. It is used as a reference for bundle adjustment and 3D point clouds. The dimension of the central rectangular area of the control frame is 152 mm long and 90 mm wide and is made of plastic laminated hard paper. There are many markers on the surface of the frame that can be as references. Moreover, four targets denoted as A1, A2, A3, and A4 with different heights are glued on the frame, which are used as GCPs. The heights of these four GCPs are respectively 8.15 mm, 3.20 mm, 2.90 mm, and 3.36 mm relative to the bottom of the frame. They are measured by a vernier caliper to a precision of 0.01 mm. Similarly, the distances between targets are also measured by the same vernier caliper. The region enclosed by these four control points is 100 mm long and 90 mm wide (90 cm²) and considered to be useful for macrotexture measurement.

Data Collection Procedure

Since the Indiana Department of Transportation (INDOT) has been successfully using LTS to measure MPD for several years, the MPD measured by LTS is assumed to be accurate and reliable. Therefore, the MPD by LTS is used to validate the accuracy of the image-base method in this paper. The data collection procedure for MPD analysis consists of the following steps. After selecting several proper spots on the road, the control frame is placed on one spot along the road direction. Next, we place the LTS on top of the control frame to measure the MPD. In the subsequent step, we remove the LTS while leaving the control frame on road and take dozens of images using a smartphone. The smartphone is about 400 mm above the control frame and follows a circular trajectory with a diameter about 600 mm. Data collection is completed when this procedure is applied to all spots.



Table 1. Specifications of the LTS 9400.

| Specifications | Values |
|--|----------------|
| Scan area (mm) | 107.95 × 72.01 |
| Vertical Resolution (mm) | 0.015 |
| Maximum Length Resolution (mm) | 0.015 |
| Maximum Width Resolution (mm) | 0.0635 |
| Triangulation angle at the center of range (°) | 32 |
| Dot size at center of range (μm) | 50 |
| Dot size at max and min range (μm) | 220 |
| Max laser sampling speed (kHz) | 1 |

Table 2. Specifications of iPhone 8 Plus camera.

| Specifications | Values |
|--------------------------|-------------|
| Wide-angle camera | |
| Aperture | f/1.8 |
| Focal length (mm) | 28 |
| Telephoto camera | |
| Aperture | f/2.8 |
| Focal length (mm) | 56 |
| Image dimension (pixels) | 4032 × 3024 |
| Pixel size (μm) | 1.22 × 1.22 |

Sites of Data Collection

INDOT Test Site

The test site is located at the INDOT District Office, West Lafayette, Ind., as shown in Figure 2a. There are three different types of pavements tested. In Figure 2a, the right lane is three-year-old hot-mix asphalt (HMA) pavement, while the left lane is 10-year-old HMA pavement. A 1 m long × 1 m wide high friction surface treatment (HFST) area is constructed on top of the 10-year-old HMA pavement. The measurements were performed on the above-mentioned three different pavements on 3 December 2018. For each pavement, there are two testing spots for data collection. Table 3 summarizes the testing spots at the INDOT test site.

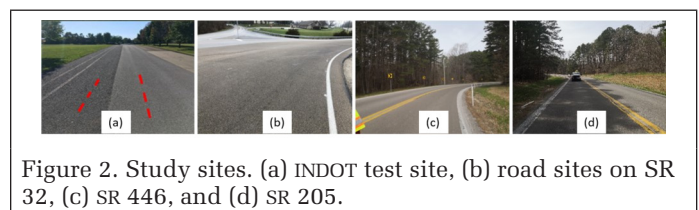


Table 3. Summary of data collected at the INDOT test site spots 3 December 2018.

| Type of pavement | LTS | Image method | |
|------------------|-----------------|-----------------|--------------------------------|
| | Number of spots | Number of spots | Number of images for each spot |
| 10-year-old HMA | 2 | 2 | 27 |
| 3-year-old HMA | 2 | 2 | 22, 29 |
| HFST | 2 | 2 | 24, 25 |

Road Sites

Shown in Figure 2b, the HFST on State Route (SR) 32 was completed on 13 August 2018. Before the HFST, the existing pavement surface was a 9.5 mm HMA mixture. On the day of treatment, the LTS was applied and 11 MPDs were collected for construction quality control. On 5 April 2019, about eight months after treatment, three MPDs by LTS and 64 images were collected at three spots. The detailed information of data collected on SR 32 is shown in Table 4. Traffic control was required during the measurement process. Due to an intensive time constraint, the LTS and smartphone testing was conducted side by side simultaneously instead of using the exact same locations consecutively.

As shown in Figure 2c, the HFST on SR 446 was finished on 17 October 2018. Before the HFST, the existing pavement surface was single-layer chip seal. On the day of treatment, the LTS collected 10 MPDs for construction quality control. On 11 April 2019, about six months after the treatment, a total of 290 images were collected at 10 spots. LTS measurements were conducted for seven of these spots. The detailed information of data collected on SR 446 is shown in Table 4. Traffic control was necessary during the measurement process. As such, the LTS and smartphone testing was conducted side by side simultaneously instead of using the exact same location consecutively.

The HFST construction at SR 205 was finished on 22 October 2018. Before the HFST, the existing pavement surface was single-layer chip seals. On the day of construction, the LTS was applied and 11 groups of MPDs were collected for construction quality control. On 16 April 2019, six months after the treatment, 12 MPDs by LTS and 306 images were collected at 12 spots. The detailed information of data collected on SR 205 is shown in Table 4, while Figure 2d shows a glance of the SR 205.

Methodology

This section first introduces several methods implemented in this paper for 3D point cloud generation and analysis, which includes SfM, bundle adjustment, and MVS. Then, the metric for macrotexture measurement or MPD and its calculation based on image-derived point clouds are presented in detail.

Structure-from-Motion and Multi-View Stereo Techniques

This section introduces the techniques for 3D point cloud generation and analysis used in this paper. This study uses Agisoft Metashape 1.5.0.701 to create 3D point clouds from road images. Although the implementation steps of the technique may vary depending on the software packages used, it consists of the following general steps.

Tie Points Generation

The SfM method aims to identify the common features in consecutive images collected from different angles to estimate the interior and exterior orientation parameters for each camera position. Therefore, the first step in SfM implementation is to detect, describe, and match the corresponding keypoints between different image-frames.

All the algorithms consist of two parts: (1) keypoint detection and (2) keypoint description. For example, the scale-invariant feature transform (SIFT) algorithm (Lowe 1999; Lowe 2004) includes the SIFT detector and SIFT descriptor. First, the detector is used to extract the keypoints, i.e., stable and well-defined points on the images. For each keypoint, its local neighborhood image is then used to calculate its properties, including gradient magnitudes and gradient directions to form a feature descriptor. Finally, correspondence of key points on different images are established by calculating the distances between feature descriptors (Rashid *et al.* 2019). Such corresponding points are shown in Figure 3a and will be used as tie points in the subsequent bundle adjustment.

Bundle Adjustment

SfM in principle does not necessarily rely on GCPs and prior camera calibration. It takes advantage of the redundancy provided by the large number of images and key points to estimate the interior orientation, exterior (or relative in the conventional photogrammetry term) orientation, and distortion parameters. The output of this process without GCP is an unscaled sparse point cloud under an arbitrary coordinate system. To achieve metric and reliable 3D point clouds, recent SfM developments can accommodate the inclusion of GCPs through bundle adjustment. As such, the four control points of the control frame are included in the SfM solution together with all tie points established through image correspondence. This way the images (Figure 3b) and the tie points clouds (Figure 3c) are oriented with reference to the control frame.

Table 4. Summary of data collected at selected spots on State Roads (SR).

| State Roads | Day of Construction | | After Construction | | | |
|-------------|---------------------|-------------|--------------------|-----------------|--------------------------------|-------------|
| | LTS | | LTS | Image method | | Date (2019) |
| | Number of spots | Date (2018) | Number of spots | Number of spots | Number of images for each spot | |
| SR 32 | 11 | 13 Aug | 3 | 3 | 20–22 | 5 Apr |
| SR 446 | 10 | 17 Oct | 7 | 10 | 20–32 | 11 Apr |
| SR 205 | 11 | 22 Oct | 12 | 12 | 22–29 | 16 Apr |

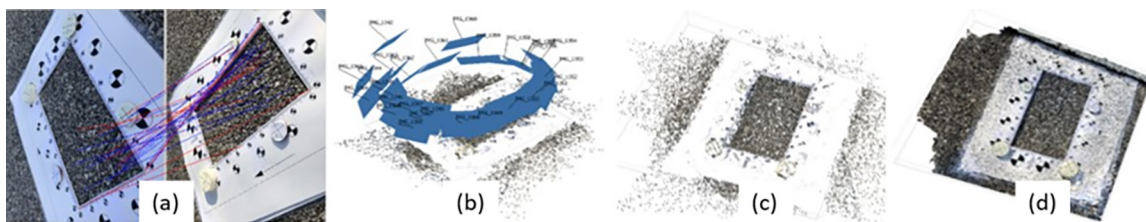


Figure 3. Results from SfM-MVS. (a) Keypoint matching between two images. (b) Output of bundle adjustment. The dark points are sparse point cloud generated for the scene, and the blue rectangles represent the position and orientation of the images. (c) Sparse point cloud and (d) dense point cloud. In this example, there are 29 132 points in the sparse point cloud, and 38 510 294 points after dense matching.

Dense Point Cloud Generation

In the last step, the point density is increased by multi-view stereo algorithms. Figure 3d illustrates the dense point cloud generated from the sparse point cloud. The purpose of the algorithms is to reconstruct the 3D point cloud of an object using overlapped images collected from different viewpoints and known camera positions (Seitz *et al.* 2006; Uh, Matsu-shita, and Byun 2014). In fact, the SfM method ended in the previous step where the sparse point cloud is generated. When a dense point cloud is also required in the application, it is obtained with an MVS algorithm. As such the name of the entire workflow is also called SfM-MVS.

Mean Profile Depth

This section first introduces the definition of mean segment depth (MSD) and MPD. We then describe the analytics for MPD calculation from image-based point clouds.

Definition of MPD

According to ASTM E1845-09, MPD is the average of all the MSDs for all the segments of a profile. Each profile segment should be 100±2mm long for analysis in the subsequent steps. The profile segment is applied to a filter to preserve textures with a wavelength ranging from 0.5 mm to 50 mm. One segment should be further divided into two equal lengths of 50mm and the maximum value is determined for each sub-segments. Then these two values are averaged arithmetically to obtain the MSD. The MSD is the average value of peak level (1st) and peak level (2nd) having a given baseline (segment), as shown in Figure 4 and Equation 1 (ASTM E1845-09 2009).

$$MSD = \frac{1}{2}(\text{Peak level}(1st) + \text{Peak level}(2nd)) \quad (1)$$

Finally, the MPD of a spot is calculated by averaging the MSDs of m profiles

$$MPD = \frac{1}{m} \sum_{i=1}^m MSD_i \quad (2)$$

Equations 1 and 2 are specified by ASTM E1845-09. According to ASTM E1845-09, both LTS and our image-based method use a baseline of 100 ± 2 mm long and choose $m=10$ profiles for MPD calculation.

MPD Calculation from Point Clouds

After the dense point cloud of a study spot is generated, we calculate its MPD by following the definition introduced in the section “Definition of MPD”. To be consistent with the calculation of LTS, we select ten 100-mm profiles along the road direction for each spot while maintaining the same spacings between adjacent profiles as LTS. To do so, we read the LTS output file to get the spacings between adjacent profiles. As listed in Table 5, the profile spacings are approximately 8.5 mm.

Ten profiles at the same spacing as in Table 5 are selected from the point cloud. For each profile, the Butterworth pass-band filter (Butterworth 1930) is first applied to retain the macrottextures. As suggested by (Dong, Prozzi, and Ni 2019), this filter can provide a maximal flat amplitude response in the passband. The sampling frequency used is 1 kHz, with a corresponding sampling interval of 1 mm. Therefore, the sampling interval of 0.5 mm corresponds to the sampling frequency of 2 kHz, while the sampling interval of 50 mm corresponds to the sampling frequency of 20 Hz. Since the wavelength of macrottexture ranges from 0.5 mm to 50 mm, the low-pass cut-off frequency for macrottexture is 2 kHz, and the high-pass cut-off frequency is 20 Hz. Every profile is processed with this bandpass filter, so that only macrottexture is retained for the subsequent MSD calculation.

Suppose Z is the direction perpendicular to road surface and X is along the road direction. $[X_a, X_b]$ is the range of the

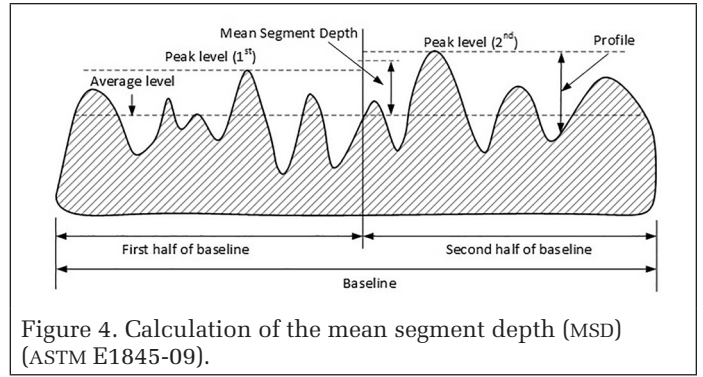


Figure 4. Calculation of the mean segment depth (MSD) (ASTM E1845-09).

Table 5. Spacing between adjacent LTS profiles.

| Spacing (mm) | Adjacent profiles | | | | | | | | |
|--------------|-------------------|--------|-------|--------|--------|--------|--------|-------|--------|
| | 1-2 | 2-3 | 3-4 | 4-5 | 5-6 | 6-7 | 7-8 | 8-9 | 9-10 |
| | 7.9174 | 8.3255 | 8.621 | 8.7999 | 8.8599 | 8.8001 | 8.6213 | 8.326 | 7.9181 |

profile in X direction. The average level for the profile with n points is denoted as a line expressed by Equation 3:

$$a_1X + b_1Z + c_1 = 0, \quad X \in [X_a, X_b] \quad (3)$$

Its coefficients a_1, b_1 , and c_1 are determined based on the least-squares criterion in Equation 4:

$$\operatorname{argmin}_{a_1, b_1, c_1} \sum_{i=1}^n \left(Z_i + \frac{a_1 X_i + c_1}{b_1} \right)^2 \quad (4)$$

Therefore, for point (X_i, Z_i) in the profile, the height deviation h_i or the distance from the point to the average level, is represented by Equation 5:

$$h_i = |a_1 X_i + b_1 Z_i + c_1| / \sqrt{a_1^2 + b_1^2} \quad (5)$$

By using height deviation, calculated above, MSD can be further calculated via Equation 6, in which X_j and X_k are respectively the locations of the peak levels in the two subsegments.

$$MSD = \frac{1}{2} \times (h_j + h_k) \quad (6)$$

Once the MSDs for the 10 selected profiles are calculated, its average (Equation 2) is taken as the MPD for this spot.

Results and Evaluation

This section discusses the MPD results from the image-based method in comparison with the ones from LTS.

Point Clouds from Images

The characteristics of the generated point clouds are listed in Table 6. For MPD calculation, 20 to 32 images were collected at each study spot, yielding a total of 790 images for 31 spots. The control frame was deployed and four GCPs were used during bundle adjustment. In average, each spot has 8202 tie points and 5 128 497 dense matching points. The root mean square errors at the GCPs are 0.113 mm, 0.125 mm, and 0.149 mm respectively in X , Y , and Z directions.

Once the ground coordinates of the tie points of the 3D point cloud are computed, these tie points are reprojected onto each image. Thus, the discrepancy between the reprojected pixel and the original pixel is the residuals. The average RMS error for residuals of the tie points is 1.550 pixels on the image or 0.585

Table 6. Overall characteristics of the image-based point clouds.

| Number of spots | Number of images | Avg. on tie points | | Avg. RMS at GCPs | | | Avg. on point clouds | |
|-----------------|------------------|--------------------|-----------------------|------------------|--------|--------|----------------------|---------------------|
| | | Number of points | RMS residual (pixels) | X (mm) | Y (mm) | Z (mm) | Number of points | ground spacing (mm) |
| 31 | 790 | 8202 | 1.550 | 0.113 | 0.125 | 0.149 | 5 128 497 | 0.070 |

mm on the ground. As an example, Figure 5 shows the distribution of the residuals on the tie points in one of the studied spots. The residuals in *x* and *y* directions are both in normal distribution with a mean of -0.0273 pixels in *x* and -0.0117 pixels in *y*. More than 95% of the residuals are within the mean±2σ.

Besides the numerical analysis, Figure 6 presents examples of 3D point clouds generated from images. The upper left picture shows the height (*Z*) of the three-year-old pavement at INDOT test site with smooth textures, while the other three pictures show the height of HFST pavements on road sites with the rough textures. The height deviation and change of texture roughness can be clearly depicted by the high-quality 3D model. As an overall conclusion of the above analysis, the dense point clouds generated from images are in high quality and fine resolution and can be used in subsequent MPD calculation.

MPD Results at the INDOT Test Site

The first data collection location was the test site located at INDOT, where six MPDs by LTS and 130 images were collected from six different spots at the test site. The MPD results from both methods are listed in Table 7.

The MPDs of spot 1 and spot 2 represent the macrotexture of the three-year-old HMA pavement, whose average MPD is 0.624 mm. The MPDs of spot 3 and spot 4 represent the macrotexture of the 10-year-old HMA pavement, whose average MPD is 1.299 mm, which was larger than the one of the three-year-old

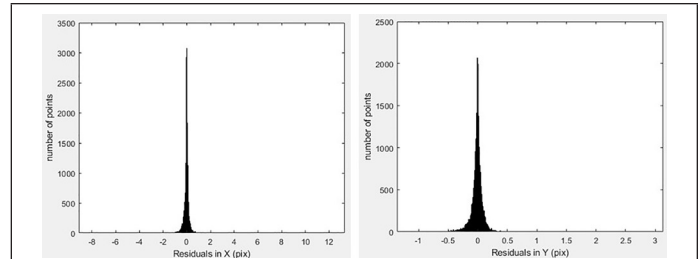


Figure 5. Examples of residual distribution of tie points in *x* (left) and *y* directions (right).

HMA pavement. After 10 years the asphalt had been stripped and the gravel layer was exposed, which accounted for its larger MPD than the three-year-old HMA pavement. Finally, the MPDs of spot 5 and spot 6 represent the macrotexture of the HFST pavement, which is larger than that the MPD of both HMA pavements. Accordingly, as the time goes on, the MPDs of pavement would decrease first then increase. The MPD of HFST is improved by 200% compared to the three-year-old pavement and by 50% with respect to the 10-year-old pavement. Therefore, applying HFST on the existing old road is effective to increase the pavement friction.

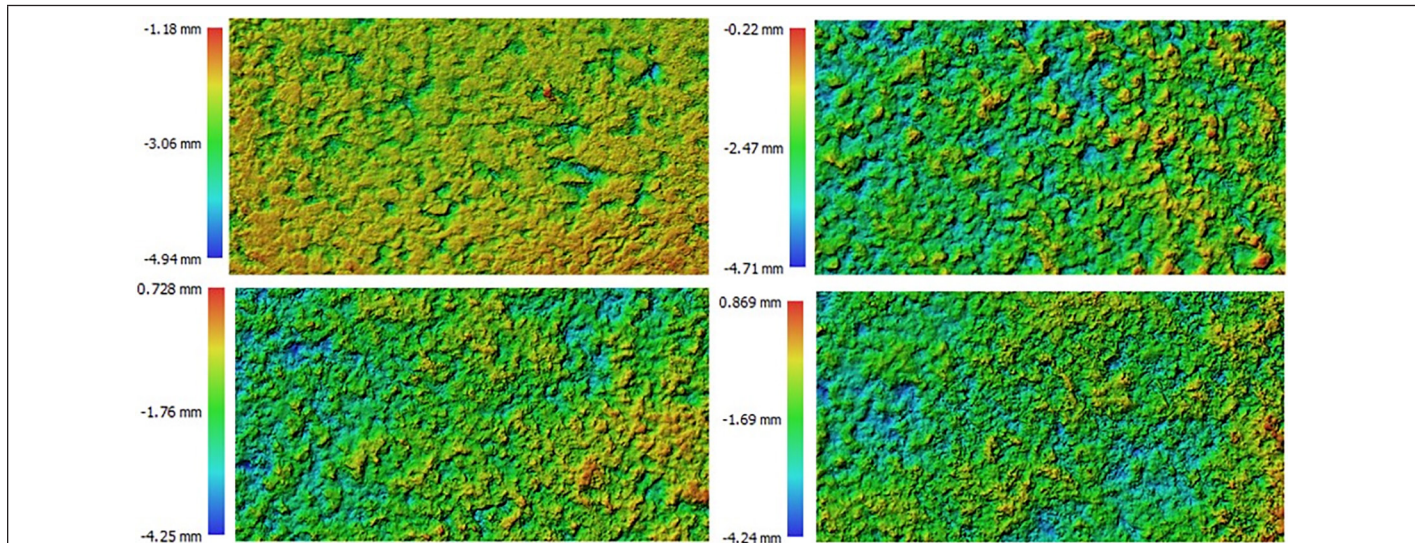


Figure 6. Four examples of 3D point clouds rendered over images respectively from the INDOT test site (upper left), SR 32 (upper right), SR 446 (lower left), and SR 205 (lower right).

Table 7. MPD from LTS and images for the INDOT test site.

| | Type of pavement and Spot ID | | | | | | | | |
|---|------------------------------|-------------|-------|--------------------------|-------------|-------|---------------|-------------|-------|
| | 3-year-old HMA pavement | | | 10-year-old HMA pavement | | | HFST pavement | | |
| | 1 | 2 | Avg. | 3 | 4 | Avg. | 5 | 6 | Avg. |
| Image method No. of images MPD (mm) | 27 0.576 | 27 0.679 | 0.628 | 22 1.197 | 29 1.443 | 1.320 | 25 1.775 | 24 1.714 | 1.745 |
| LTS method MPD (mm) | 0.515 | 0.733 | 0.624 | 1.275 | 1.323 | 1.299 | 1.749 | 2.073 | 1.911 |
| Difference of MPD (%) | 11.84 | -7.37 | 0.56 | -6.12 | 9.07 | 1.62 | 1.49 | -17.32 | -8.71 |

As shown in Table 7, the MPDs measured by LTS range from 0.515 mm to 2.073 mm, and the MPDs based on images range from 0.576 mm to 1.775 mm. The average MPDs for three-year-old HMA pavement, 10-year-old HMA pavement, and HFST pavement at the six INDOT spots measured by LTS are respectively 0.624 mm, 1.299 mm, and 1.911 mm. The corresponding average MPDs from the image-based method are 0.628 mm, 1.320 mm, and 1.745 mm, respectively.

It is noticed that the MPD for spot 6 has a large discrepancy between the LTS and image-based methods. Figure 7 compares the MPDs of the 10 profiles from the LTS and image-based methods. After the detailed investigation on the comparison of the 10 profiles of both two methods, two possible reasons for the large discrepancy between the results of the two methods are discovered. The first one is that the 10 profiles taken by image-based method cannot be assured to be the exact same profiles scanned by the LTS, although the authors try to make sure the identical adjacent profile spacing. The second reason, which is more severe, is the blunders existing in the results of both methods. Figure 7 indicates that a blunder in the LTS results causes this large discrepancy. Its MPD at this spot is too large to be reasonable. Although large discrepancies between the MPDs from two methods may exist, the average MPDs from both methods were consistent. The maximum difference between the average MPDs for the two methods over several spots is less than 9%. The tests suggest that the image-based method has the capability of acquiring comparable MPD results and is less vulnerable to blunders than LTS.

MPD Results on Road Sites

The MPDs at the three road sites were collected by LTS on the day of the HFST construction, whose results are summarized in Table 8, with MPDs being 2.075 mm, 1.590 mm, and 1.860 mm respectively for SR 32, SR 446, and SR 205. According to ASTM E1845-09, the average MPD measured on the day of construction reflects the macrotexture of the HFST pavement. Several (5.7–7.7) months later, these three State Road sites were revisited and the MPDs by both LTS and images were measured. Table 8 summarizes the average MPD from LTS and images for each revisited road site.

As shown in Table 8, 11 MPDs by LTS were measured on SR 32 on the day of construction and the average MPD is 2.075 mm. After 7.7 months, three MPDs by LTS were collected on the same road and their average MPD is 1.315 mm, a 36.63% reduction since construction. During this revisit, a total of 64 images were shot as well for these three locations, yielding three 3D point clouds. The average MPD calculated by the image-based method is 1.416 mm, which is only 7.71% or 0.101 mm larger than the average MPD from LTS.

As for SR 446, 10 MPDs by LTS were measured on the day of construction and the average MPD is 1.590 mm. After 5.8 months, seven MPDs by LTS were collected at seven locations on the same road, yielding an average MPD being 1.259 mm or a 20.82% reduction since construction. During this revisit, a total of 290 images were shot at 10 spots, yielding 10 3D point clouds. The average MPD calculated by the image-based method was 1.189 mm, which is only -5.57% or 0.070 mm, smaller than the average MPD from LTS.

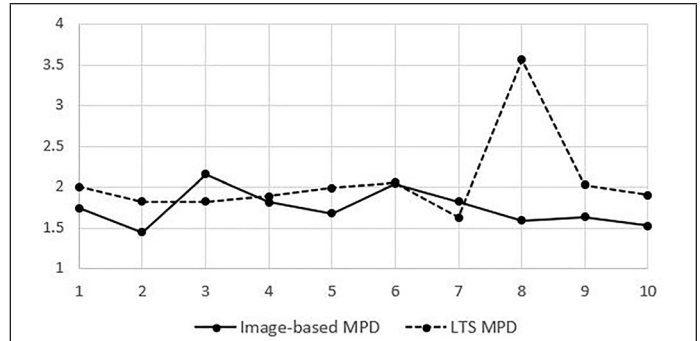


Figure 7. Comparison between MPDs of the 10 profiles between LTS and image-based method for spot 6 at the INDOT test site. A noticeable blunder exists in the LTS data.

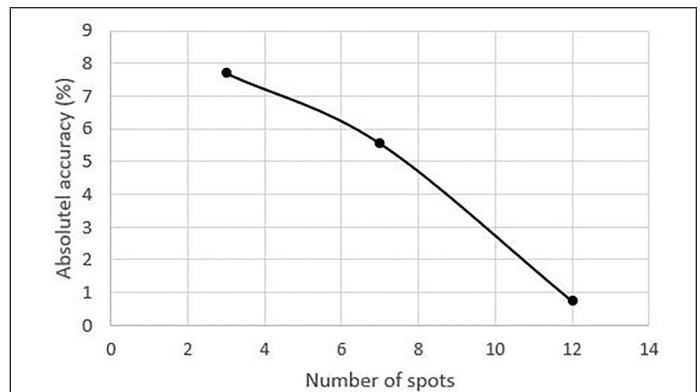


Figure 8. Average MPD difference between two methods versus the number of spots observed.

As for the last road site SR 205, 11 MPDs by LTS were measured on the day of construction, yielding an average MPD of 1.860 mm. After 5.8 months, 12 MPDs by LTS were collected at 12 spots on the same road, which leads to an average MPD of 1.243 mm or a 33.17% reduction. During the revisit, a total of 306 images were shot at 12 spots, which gives an average MPD of 1.234 mm, which is only -0.75% or 0.009 mm smaller than the average MPD from LTS.

Discussion

The above abundant tests reveal some important observations and understandings. Although blunders may exist in both methods, blunders in the image-derived point clouds tend to be outside the control frame due to mismatching on particles in the air, whereas blunders of LTS are relatively small and mostly caused by ranging noise. The former is easy to identify and remove, while the latter has small magnitude but can cause significant measurement errors if not removed. Moreover, the average MPDs from the image-based method are consistent with ones from LTS. For the test sites at INDOT, the maximum magnitude of the average MPD differences between two methods is less than 9% and the average magnitude of the differences is 3.6%. For three road sites, the maximum

Table 8. Summary of the MPD of three road sites by LTS and images.

| Roads | On Construction | | Months after | After Construction | | | | | |
|--------|-----------------|---------------|--------------|--------------------|---------------|---------------|--------------|---------------|-----------------------|
| | No. of spots | Avg. MPD (mm) | | LTS | | | Image | | Diff. of avg. MPD (%) |
| SR 32 | 11 | 2.075 | 7.7 | No. of spots | Avg. MPD (mm) | Reduction (%) | No. of spots | Avg. MPD (mm) | 7.71 |
| SR 446 | 10 | 1.590 | 5.8 | 3 | 1.315 | 36.63 | 3 | 1.416 | -5.57 |
| SR 205 | 11 | 1.860 | 5.8 | 7 | 1.259 | 20.82 | 10 | 1.189 | -0.75 |
| | | | | 12 | 1.243 | 33.17 | 12 | 1.234 | |

magnitude of the average MPD difference between LTS and image-based methods is less than 8% and the average magnitude of the difference is 4.7%. Furthermore, the numbers of observed spots on these three road sites are 3, 7, and 12. As shown in Figure 8, the corresponding variations of the MPD's among the spots in one road are 7.71%, 5.57%, and 0.75% respectively. As the number of observed spots increases, the average MPDs between the two methods tend to be more consistent. The discrepancies between the final average MPDs for a road can be reduced by increasing the number of testing spots. Considering the fact that traffic control is needed while taking the photos, no less than eight spots are recommended, which is demonstrated to cause within a 5% difference. As such, the image-based method can provide practically equivalent results as the LTS. Finally, according to the comparison between the MPD on the construction date and the one on revisit date, the MPD of the HFST would be reduced by about 30% after six to seven months of traffic. This amount of reduction is caused by the rapid polishing of the aggregates on roads, and the reduction rate would significantly slow down thereafter. Our study on macrotexture reduction with both images and LTS is consistent with previous research by (Vaiana *et al.* 2012).

In summary, the MPD calculated based on the image-based method by a smartphone is a dependable and economically feasible alternative to LTS. Moreover, no matter if LTS or the image-based method is used for MPD measurement, choosing several numbers of spots for measurement could reduce the impact of blunders and achieve reliable results.

Limitation and Future Work

Two limitations about the image-based method should be noted. One is that the entire data collection procedure for one spot takes about 2–3 minutes. This means traffic control is still necessary during measurement, though multiple sites in the vicinity can be collected simultaneously with different smartphones. A certain number of spots needs to be measured to assure the quality of measurement. The trade-off between accuracy and traffic control should be taken into consideration. Our recommendation of measuring eight spots is very conservative as a balance between these two aspects. Another limitation is its long computation time for the image-based method. Fine resolution 3D reconstruction from images may take a couple of hours on a laptop. In contrast, the LTS reports the measured MPD on its screen within a couple of minutes after applying it on a road. This feature can be demanding when real-time quality control is needed during construction. As such, the image based method at present may not be suitable for real-time quality control in pavement construction.

For time critical applications, it is necessary to make 3D reconstruction available on a smartphone. To make that happen, a light version of 3D reconstruction is more desirable. Dense 3D reconstruction may be created only for selected profiles in the field. This would shorten the computational time tremendously for 3D reconstruction. The efficiency of pavement texture measurement can be improved to a new degree by integrating image collection and image processing into one smartphone application.

Conclusion

This paper presents a novel approach for MPD measurement using multi-view images collected by a smartphone at a typical resolution of 12 MP. In comparison to reported professional camera systems for pavement macrotexture measurement, it is much simple, cost-effective, portable, and easy to deploy for large scale applications.

The image-based approach was evaluated with reference to the conventional laser texture scanner. 3D point clouds were generated from 790 images collected *in situ* at 31 different spots. It was shown that smartphone images with a home-made control frame are sufficient for the reconstruction of accurate and high-resolution 3D point clouds. Through comparative studies, we show that the MPDs measured by laser texture scanner and smartphone images have an average difference of 4% and a maximum difference of 9%. The quality of the image based method can be assured by taking about 30 images for one spot and selecting up to eight spots on a road. Under this very conservative recommendation, the results from a laser texture scanner and smartphone images are essentially comparable, whereas the latter is at least one magnitude times cheaper than the former and is popular among the general public. Furthermore, the use of smartphones would eliminate the routine calibration and upgrade of the laser texture scanner. Since there is virtually no training needed for using a smartphone to collect images on roads, it is reasonable to expect this approach be adopted widely for practical applications.

Future effort is worthwhile in the following aspects. Modern smartphones often offer several options for image collection. This study only used the wide-angle default camera. Though this can maximize the incoming light while keeping a convenient photograph distance, other options such as zooming-in, larger f-stop, high dynamic range, and even video may be evaluated. The objective is to find an optimal image collection strategy in the field. Next, road roughness or MPD reduces quickly within the first few months after construction and then exhibits slow decline afterwards. It is necessary to continuously monitor the change of road roughness over a longer period time. To do so, we need to further study the sensitivity of the image-based method for heavily polished road surface and compare it with the laser texture scanner. Then, we also need to further explore the possibility and optimal methods to reduce the necessary number of spots in the road for image collection while achieving reliable and accurate roughness measurements. Finally, rapid *in situ* MPD calculation and reporting is necessary for real-time quality control in construction management. Developing smartphone applications for 3D reconstruction for selected pavement profiles would be a feasible solution to meet such time critical need.

Acknowledgments

This work was sponsored by the Indiana Department of Transportation (INDOT) in cooperation with the Federal Highway Administration (FHWA) through the Joint Transportation Research Program (JTRP) of INDOT and Purdue University.

References

- Abe, H., A. Tamai, J. J. Henry and J. Wambold. 2001. Measurement of pavement macrotexture with circular texture meter. *Transportation Research Record* 1764:201–209. doi: 10.3141/1764-21.
- ASTM E1845-09. 2009. *Standard Practice for Calculating Pavement Macrotexture Mean Profile Depth*. West Conshohocken, Pa.: ASTM International.
- Bitelli, G., A. Simone, F. Girardi and C. Lantieri. 2012. Laser scanning on road pavements: A new approach for characterizing surface texture. *Sensors* 12 (7):9110–9128. doi: 10.3390/s120709110.
- Butterworth, S. 1930. On the theory of filter amplifiers. *Experimental Wireless and the Wireless Engineer* 7:536–541.
- Chandler, H., J. G. Fryer and A. Jack. 2005. Metric capabilities of low cost digital cameras for close range surface measurement. *The Photogrammetric Record* 20 (109):12–26.

- Das, A., V. Rosauer and J. S. Bald. 2015. Study of road surface characteristics in frequency domain using micro-optical 3-D camera. *KSCE Journal of Civil Engineering* 19 (5):1282–1291. doi: 10.1007/s12205-013-0529-3.
- Dong, N., J. Prozzi and F. Ni. 2019. Reconstruction of 3D pavement texture on handling dropouts and spikes using multiple data processing methods. *Sensors* 19 (2):278. doi: 10.3390/s19020278.
- Dunford, A. 2013. *Friction and the Texture of Aggregate Particles Used in the Road Surface Course*, Ph.D. thesis, University of Nottingham.
- Edmondson, V., J. Woodward, M. Lim, M. Kane, J. Martin and I. Shyha. 2019. Improved non-contact 3D field and processing techniques to achieve macrotexture characterisation of pavements. *Construction and Building Materials* 227:116693. doi: 10.1016/j.conbuildmat.2019.116693.
- Ejsmont, J. A., G. Ronowski, B. Świczko-Zurek and S. Sommer. 2016. Road texture influence on tyre rolling resistance. *Road Materials and Pavement Design* 18 (1):181–198. doi: 10.1080/14680629.2016.1160835.
- Flintsch, G., E. D. Izeppi, M. Saleh and K. K. Mcghee. 2008. Area-based macrotexture measurements using stereo vision. In *Proceedings of the 6th Symposium on Pavement Surface Characteristics*, held in Portoroz, Slovenia.
- Fisco, N. and H. Sezen. 2014. Comparison of surface macrotexture measurement methods. *Journal of Civil Engineering and Management* 19 (Supplement 1):153–160. doi: 10.3846/13923730.2013.802732.
- Gendy, A. E., A. Shalaby, M. Saleh and G. W. Flintsch. 2011. Stereo-vision applications to reconstruct the 3D texture of pavement surface. *International Journal of Pavement Engineering* 12 (3):263–273. doi: 10.1080/10298436.2010.546858.
- Georgopoulos, A., A. Loizos and A. Flouda. 1995. Digital image processing as a tool for pavement distress evaluation. *ISPRS Journal of Photogrammetry and Remote Sensing* 50 (1):23–33.
- White, G., C. Ward and S. Jamieson. 2019. Field evaluation of a handheld laser meter for pavement surface macrotexture measurement. *International Journal of Pavement Engineering*. doi: 10.1080/10298436.2019.1654103.
- Henry, J. J. 2000. *Evaluation of Pavement Friction Characteristics*, series 291. Transportation Research Board, 0547–5570. Washington, D.C.: National Academy Press. <<http://worldcat.org/isbn/0309068746>>.
- Kogbara, R. B., E. A. Masad, D. Woodward and P. Millar. 2018. Relating surface texture parameters from close range photogrammetry to Grip-Tester pavement friction measurements. *Construction and Building Materials* 166:227–240. doi: 10.1016/j.conbuildmat.2018.01.102.
- Li, L., K. C. Wang and Q. J. Li. 2016. Geometric texture indicators for safety on AC pavements with 1mm 3D laser texture data. *International Journal of Pavement Research and Technology* 9 (1):49–62. doi: 10.1016/j.ijprt.2016.01.004.
- Lowe, D. 1999. Object recognition from local scale-invariant features. In *Proceedings of the Seventh IEEE International Conference on Computer Vision*. doi: 10.1109/iccv.1999.790410.
- Lowe, D. G. 2004. Distinctive image features from scale-invariant keypoints. *International Journal of Computer Vision* 60 (2):91–110. doi: 10.1023/b:visi.0000029664.99615.94.
- McQuaid, G., D. Woodward, P. Millar and S. Friel. 2013. Use of close range photogrammetry to assess the microtexture of asphalt surfacing aggregates. *International Journal of Pavements Conference* 219-2.
- Micheletti, N., J. H. Chandler and S. N. Lane. 2014. Investigating the geomorphological potential of freely available and accessible structure-from-motion photogrammetry using a smartphone. *Earth Surface Processes and Landforms* 40 (4):473–486. doi: 10.1002/esp.3648.
- Patzak, T., M. Hase, R. Roos and T. Worner. 2016. Friction of different surface courses. In *Proceedings of the 6th Eurasphalt & Eurobitume Congress*. doi: dx.doi.org/10.14311/EE.2016.256.
- Praticò, F. and R. Vaiana. 2015. A study on the relationship between mean texture depth and mean profile depth of asphalt pavements. *Construction and Building Materials* 101:72–79. doi: 10.1016/j.conbuildmat.2015.10.021.
- Rashid, M., M. A. Khan, M. Sharif, M. Raza, M. Sarfraz and F. Afza. 2019. Object detection and classification: A joint selection and fusion strategy of deep convolutional neural network and SIFT point features. *Multimedia Tools and Applications* 78:15751–15777. doi: <https://doi.org/10.1007/s11042-018-7031-0>.
- Sapp, D., R. Thelin, and S. Nunn. 2017. Indiana Crash Facts 2017. <https://trafficsafety.iupui.edu/crash-fact-books/Crash%20Fact%20Book_2017_Final%20Lo%20Res.pdf> Accessed day Month year.
- Sarker, M., D. Dias-da-Costa and S. Hadighen. 2019. Multi-scale 3D roughness quantification of concrete interfaces and pavement surfaces with a single-camera set-up. *Construction and Building Materials* 222:511–521. doi: 10.1016/j.conbuildmat.2019.06.157.
- Seitz, S., B. Curless, J. Diebel, D. Scharstein and R. Szeliski. 2006. A comparison and evaluation of multi-view stereo reconstruction algorithms. In *Proceedings of the 2006 IEEE Computer Society Conference on Computer Vision and Pattern Recognition (CVPR06)*, vol. 1. doi: 10.1109/cvpr.2006.19.
- Sengoz, B., A. Topal and S. Tanyel. 2012. Comparison of pavement surface texture determination by sand patch test and 3D laser scanning. *Periodica Polytechnica Civil Engineering* 56 (1):73. doi: 10.3311/pp.ci.2012-1.08.
- Uh, Y., Y. Matsushita and H. Byun. 2014. Efficient multiview stereo by random-search and propagation. Pages 393–400 in *Proceedings of the 2014 2nd International Conference on 3D Vision (3DV)*, vol. 1.
- Ullman, S. 1979. The interpretation of structure from motion. *Proceedings of the Royal Society of London* 203 (1153):405–426. doi: 10.1098/rspb.1979.0006.
- Vaiana, R., G. F. Capiluppi, V. Gallelli, T. Iuele and V. Minani. 2012. Pavement surface performances evolution: An experimental application. *Procedia: Social & Behavioral Sciences* 53:1150–1161. doi: 10.1016/j.sbspro.2012.09.964.
- Westoby, M., J. Brasington, N. Glasser, M. Hambrey and J. Reynolds. 2012. “Structure-from-Motion” photogrammetry: A low-cost, effective tool for geoscience applications. *Geomorphology* 179:300–314. doi: 10.1016/j.geomorph.2012.08.021.
- Yaacob, H., N. A. Hassan, M. R. Hainin and M. F. Rosli. 2014. Comparison of sand patch test and multi laser profiler in pavement surface measurement. *Jurnal Teknologi* 70 (4). doi: 10.11113/jt.v70.3497.

Advertise in the #1 publication in the imaging and geospatial information industry!



Impact Factor (2018): 3.15

PE&RS (*Photogrammetric Engineering & Remote Sensing*) is the official journal of the American Society for Photogrammetry and Remote Sensing—the Imaging and Geospatial Information Society (ASPRS). This highly respected publication is the #1 publication in the industry by a wide margin. Advertisers with a desire to reach this market can do no better than PE&RS. It delivers the right audience of professionals who are loyal and engaged readers, and who have the purchasing power to do business with you.

PE&RS Readership Highlights

Circulation: 3,000
Total audience: 6,400*

Founded in 1934, the American Society for Photogrammetry and Remote Sensing (ASPRS) is a scientific association serving professional members throughout the world. Our mission is to advance knowledge and improve understanding of mapping sciences to promote the responsible applications of photogrammetry, remote sensing, geographic information systems (GIS), and supporting technologies.

Our members are analysts/specialists, educators, engineers, managers/administrators, manufacturers/ product developers, operators, technicians, trainees, marketers, and scientists/researchers. Employed in the disciplines of the mapping sciences, they work in the fields of Agriculture/Soils, Archeology, Biology, Cartography, Ecology, Environment, Forestry/Range, Geodesy, Geography, Geology, Hydrology/Water Resources, Land Appraisal/Real Estate, Medicine, Transportation, and Urban Planning/Development.

RESERVE YOUR SPACE TODAY!

Bill Spilman, ASPRS Advertising, Exhibit Sales & Sponsorships
(877) 878-3260 toll-free
(309) 483-6467 direct
(309) 483-2371 fax
bill@innovativemediasolutions.com

| | Corporate Member Exhibiting at a 2019 ASPRS Conference | Corporate Member | Exhibitor | Non Member |
|--|---|--------------------------|-----------|------------|
| <i>All rates below are for four-color advertisements</i> | | | | |
| Cover 1 | \$1,850 | \$2,000 | \$2,350 | \$2,500 |
| <i>In addition to the cover image, the cover sponsor receives a half-page area to include a description of the cover (maximum 500 words). The cover sponsor also has the opportunity to write a highlight article for the journal. Highlight articles are scientific articles designed to appeal to a broad audience and are subject to editorial review before publishing. The cover sponsor fee includes 50 copies of the journal for distribution to their clients. More copies can be ordered at cost.</i> | | | | |
| Cover 2 | \$1,500 | \$1,850 | \$2,000 | \$2,350 |
| Cover 3 | \$1,500 | \$1,850 | \$2,000 | \$2,350 |
| Cover 4 | \$1,850 | \$2,000 | \$2,350 | \$2,500 |
| Advertorial | 1 Complimentary Per Year | 1 Complimentary Per Year | \$2,150 | \$2,500 |
| Full Page | \$1,000 | \$1,175 | \$2,000 | \$2,350 |
| 2 page spread | \$1,500 | \$1,800 | \$3,200 | \$3,600 |
| 2/3 Page | \$1,100 | \$1,160 | \$1,450 | \$1,450 |
| 1/2 Page | \$900 | \$960 | \$1,200 | \$1,200 |
| 1/3 Page | \$800 | \$800 | \$1,000 | \$1,000 |
| 1/4 Page | \$600 | \$600 | \$750 | \$750 |
| 1/6 Page | \$400 | \$400 | \$500 | \$500 |
| 1/8 Page | \$200 | \$200 | \$250 | \$250 |
| Other Advertising Opportunities | | | | |
| Wednesday Member Newsletter Email Blast | 1 Complimentary Per Year | 1 Complimentary Per Year | \$600 | \$600 |

A 15% commission is allowed to recognized advertising agencies

THE MORE YOU ADVERTISE THE MORE YOU SAVE! PE&RS offers frequency discounts. Invest in a three-times per year advertising package and receive a 5% discount, six-times per year and receive a 10% discount, 12-times per year and receive a 15% discount off the cost of the package.

*Based on 2 readers per copy as well as online views | Source: PE&RS Readership Survey, Fall 2012

Digital Elevation Model Technologies and Applications: The DEM Users Manual, 3rd Edition

Edited by David F. Maune, PhD, CP
and Amar Nayegandhi, CP, CMS

To order, visit
<https://www.asprs.org/dem>

The 3rd edition of the DEM Users Manual includes 15 chapters and three appendices. References in the eBook version are hyperlinked. Chapter and appendix titles include:

1. Introduction to DEMs
David F. Maune, Hans Karl Heidemann, Stephen M. Kopp, and Clayton A. Crawford
 2. Vertical Datums
Dru Smith
 3. Standards, Guidelines & Specifications
David F. Maune
 4. The National Elevation Dataset (NED)
Dean B. Gesch, Gayla A. Evans, Michael J. Oimoen, and Samantha T. Arundel
 5. The 3D Elevation Program (3DEP)
Jason M. Stoker, Vicki Lukas, Allyson L. Jason, Diane F. Eldridge, and Larry J. Sugarbaker
 6. Photogrammetry
J. Chris McGlone and Scott Arko
 7. IfSAR
Scott Hensley and Lorraine Tighe
 8. Airborne Topographic Lidar
Amar Nayegandhi and Joshua Nimetz
 9. Lidar Data Processing
Joshua M. Novac
 10. Airborne Lidar Bathymetry
Jennifer Wozencraft and Amar Nayegandhi
 11. Sonar
Guy T. Noll and Douglas Lockhart
 12. Enabling Technologies
Bruno M. Scherzinger, Joseph J. Hutton, and Mohamed M.R. Mostafa
 13. DEM User Applications
David F. Maune
 14. DEM User Requirements & Benefits
David F. Maune
 15. Quality Assessment of Elevation Data
Jennifer Novac
- Appendix A. Acronyms
Appendix B. Definitions
Appendix C. Sample Datasets

This book is your guide to 3D elevation technologies, products and applications. It will guide you through the inception and implementation of the U.S. Geological Survey's (USGS) 3D Elevation Program (3DEP) to provide not just bare earth DEMs, but a full suite of 3D elevation products using Quality Levels (QLs) that are standardized and consistent across the U.S. and territories. The 3DEP is based on the National Enhanced Elevation Assessment (NEEA) which evaluated 602 different mission-critical requirements for and benefits from enhanced elevation data of various QLs for 34 Federal agencies, all 50 states (with local and Tribal input), and 13 non-governmental organizations.

The NEEA documented the highest Return on Investment from QL2 lidar for the conterminous states, Hawaii and U.S. territories, and QL5 IfSAR for Alaska.

Chapters 3, 5, 8, 9, 13, 14, and 15 are "must-read" chapters for users and providers of topographic lidar data. Chapter 8 addresses linear mode, single photon and Geiger mode lidar technologies, and Chapter 10 addresses the latest in topobathymetric lidar. The remaining chapters are either relevant to all DEM technologies or address alternative technologies including photogrammetry, IfSAR, and sonar.

As demonstrated by the figures selected for the front cover of this manual, readers will recognize the editors' vision for the future – a 3D Nation that seamlessly merges topographic and bathymetric data from the tops of the mountains, beneath rivers and lakes, to the depths of the sea.

Co-Editors

David F. Maune, PhD, CP and
Amar Nayegandhi, CP, CMS

PRICING

| | |
|--|------------|
| Student (must submit copy of Student ID) | \$50 +S&H |
| ASPRS Member | \$80 +S&H |
| Non-member | \$100 +S&H |
| E-Book (only available in the Amazon Kindle store) | \$85 |

LEARN
DO
GIVE
BELONG

ASPRS Offers

- » Cutting-edge conference programs
- » Professional development workshops
- » Accredited professional certifications
- » Scholarships and awards
- » Career advancing mentoring programs
- » *PE&RS*, the scientific journal of ASPRS

asprs.org

ASPRS